Electroactive Speciation Studies for Metal Ion Sensing

Mark A. Knell

Department of Chemistry

University of Durham

A thesis submitted in part-fulfillment for the degree of

Doctor of Philosophy

March 2006

Abstract

Electroactive Speciation Studies for Metal Ion Sensing

Mark A. Knell

Chemical speciation is an important factor in understanding the role of metals in the environment. Bioavailability of trace metals is influenced by the degree of the labile fraction of the metal that is readily available for interaction with a cell surface of an organism.

Voltammetric methods are capable of measuring this labile fraction, and are able to achieve limits of detection in the biologically relevant range. In this study, voltammetric methods were used to examine a set of trifluoromethyl and tolyl pyridylsulfonamide metal-ligand systems during the formation of ML_n complexes at a fixed [M]:[T] ratio and varied pH, to investigate speciation and the potential use of these ligands in surface modified sensors.

Formation constants with cobalt(II), nickel(II), copper(II), zinc(II), and the varied pyridylsulfonamide moieties, were fully evaluated by potentiometry. A method for simultaneous voltammetric-spectral pH titrations was developed and used to correlate formation constant findings.

Voltammetric investigations at a bare glassy carbon electrode had varying electroactive response from the metal-ligand systems. The labile and electroactive systems, e.g. $[CuL^1_2]$ and $[CuL^4_2]$, were used in formation constant mass-balance refinements derived from voltammetric pH titration data. It is believed that under optimised conditions, formation constant measurement by voltammetry at a glassy carbon electrode is feasible, and this method would be applicable for voltammetric speciation of metal ions in the environment.

Declaration

The work described herein was carried out in the Department of Chemistry, University of Durham between October 2000 and September 2004. All the work is my own unless otherwise stated and no part of it has been submitted for a degree at this or any other university.

Statement of Copyright

Acknowledgements

I have the following people to thank:
My supervisors, Dr. Ritu Kataky, and Prof. David Parker, for their help and advice throughout, and for giving me the opportunity to study chemistry at the University of Durham.

Aileen Congreve for collaboration with her sulfonamide ligand studies.

Prof. Marek Trojanowicz and Dr. Ewa Pobozy at the University of Warsaw for teaching me the capillary electrophoresis technique. Prof. Ignacy Cukrowski of the University of Pretoria for his valuable help and advice with the analysis of my voltammetric titration data. Prof. Peter Gans for his help with Hyperquad and titration software, and Lyndsay Molyneux for the maintenance of Molspin titration equipment.

My friends in Canada, Chris, Heather, Ben, Michelle, Tim, Dave, Jamie, Eyan and Andrea. Aiden, Tom, Georgy, Rupam, and Lisa, for their camaraderie in the lab. Katerina, Mark, Liz, Tom, Michael, and Stephani whose friendship in Durham helped take my mind off of chemistry. And Despina Kaloriti for her friendship and support that kept me going through difficult times.

And last, but not least my mother, father, stepmother, brother, grandmother, and the rest of my family, for their love and encouragement.

EPSRC for funding and support.

Table of Contents

Abbreviations

ACN	acetonitrile
ASV	anodic stripping voltammetry
$\beta_{1,2...n}$	additive protonation constant
β_{ML_n}	additive formation constant
BAS	Bioanalytical Systems Inc.
BIA	batch injection analysis
BGE	background electrolyte
CDP	cathodic differential pulse
CpE	capillary electrophoresis
CE	counter electrode
CF_3	trifluoromethyl
CF_3SQ	8-(trifluoromethylsulfoamido)quinoline
CFSE	crystal field stabilization energy
CLE	competitive ligand exchange
CSV	cathodic stripping voltammetry
CV	cyclic voltammetry
DP	differential pulse
DPASV	differential pulse anodic stripping voltammetry
DPCSV	differential pulse cathodic stripping voltammetry
DT	deposition time
DTPA	diethylenetriaminepentaacetic acid
E	potential
$E_{1/2}$	half-cell potential
$E_{p,a}$	anodic peak potential
$E_{p,c}$	cathodic peak potential
ΔE_p	peak potential separation
EMF	electromotive force
FAAS	flame atomic absorption spectroscopy
FIA	flow injection analysis

GFAAS	graphite furnace atomic absorption spectroscopy
GCE	glassy carbon electrode
GIME	gel integrated microelectrode
HOMO	highest occupied molecular orbital
I	ionic strength
$i_{p,a}$	anodic peak current
$i_{p,c}$	cathodic peak current
$i_{p,f}$	forward peak current
$i_{p,r}$	reverse peak current
ICP-MS	inductively coupled plasma-mass spectroscopy
K	equilibrium constant
$K_{1,2...}$	protonation constant
K_{ML}	complex formation constant
KHPh	potassium hydrogen phthalate
LC	liquid chromatography
LFSE	ligand field stabilization energy
LFT	ligand field theory
LMCT	ligand to metal charge transfer
LOD	limit of detection
LUMO	lowest unoccupied molecular orbital
2-Me-CF_3SQ	2-methyl-8-(trifluoromethylsulfamido)quinoline
MES	2-[N-morpholino]ethanesulfonic acid
MFE	mercury film electrode
MPA	mercaptopropanoic acid
MS	mass spectroscopy
mVs^{-1}	millivolts per second
PLM-GIME	permeable liquid membrane GIME
PA	pulse amplitude
23PDCA	2,3-pyridinedicarboxylic acid
PDCA	(2,6)-pyridinedicarboxylic acid
PSI	pounds per square inch
Q	equilibrium quotient (non-ideal)

RE	reference electrode
SAM	self assembled monolayer
SI	scan increment
SPE	solid phase extraction
SR	scan rate
STM	scanning tunneling microscopy
SV	stripping voltammetry
SW-ASV	square wave anodic stripping voltammetry
tosyl	*p*-toluenesulfonyl
TSQ	8-(4-toluenesulfonamido)quinoline
TTAOH	tetradecyltrimethylammonium hydroxide
UME	ultra-microelectrode
UMEA	ultra-microelectrode array
UV-Vis	ultraviolet and visible spectrum
V	volt
V_e	endpoint volume
VIP	voltammetric in-situ profiling system
WE	working electrode

Table of Figures

Table of Tables

Chapter 1

Monitoring of Trace Metals in the Environment

1 Monitoring of Trace Metals in the Environment

This study is concerned with the development of electrochemical sensing technology and its application to the analysis of various dissolved metal ions in water. Metal ions play a diverse role in biology, the environment and in modern society. Although many trace metals are essential to human health, the release of harmful amounts of metal complexes from natural and anthropogenic sources gives rise to a need for ongoing monitoring and an assessment of their impact.

1.1 Biological Role & Toxicity of Chromium(III), Cobalt(II), Nickel(II), Copper(II), Zinc(II) and Antimony(III)

1.1.1 Chromium

Trivalent chromium is an essential metal in man and in animals, and plays an important role in insulin metabolism as the glucose tolerance factor (GTF) and also with proper lipid and protein metabolism.[1,2] Both acute and chronic adverse effects of chromium are mainly caused by hexavalent compounds, which are very toxic to man. The ability of hexavalent compounds to induce bronchiogenic cancer in humans is well estabilished.[24] The strong oxidizing nature of hexavalent compounds appears to be the cause. Once reduced, the trivalent ion can create havoc by strong coordination with metallo-enzyme systems.[3] There is also firm evidence of mutagenic capacity of chromium(VI) species.[4,5]

Chromium is more easily absorbed, both via lungs and the gastrointestinal tract, in the hexavalent state than in the trivalent state. Chromium is found in all organs, the highest concentration usually being in the lung where accumulation occurs with age. An important consumer of chromium(III) for many years has been the tanning industry. Other uses are in pigment production, graphics industry and industries using chromium alloys and

plated materials. Industrial exposures involving chromium(VI) species are from the chemical industry, stainless steel industry, the use of alloys and in the chromium plating industry.[6,7]

1.1.2 Copper

Copper is one of the earliest known metals, *ca.* 8000 years ago it was used in bronze and brass. The element is essential to all animals,[8,9] copper containing enzymes include tyrosinase, ascorbic acid oxidase, cytochrome oxidase, monoamine oxidase, uricase, δ-aminolevelinic acid dehydratase. Normal serum levels of copper in most animals, including humans, is in the range 8.0-12.0 $\mu g\ L^{-1}$.[10]

Disease states with high copper levels include Wilson's disease, heptolenticular degeneration as well as thalassemia, hemachromatosis, cirrhosis, yellow atrophy of liver, tuberculosis and carcinomas.[11] Wilson's disease, which results in the build up of copper, is a hereditary progressive disease involving neurological disturbances and liver cirrhosis. Toxic exposures result in weakness, malaise, and loss of appetite.[12]

1.1.3 Cobalt

Essentiality was discovered in 1948 as a constituent of the vitamin B_{12} system.[13,14] Cobalt is used in the manufacture of alloys and in nuclear technology; cobalt-60 is used in medicine as a source of radiation.[12] Salts of cobalt are used for pigments, grinding wheels and previously as foam stabilizers in beer.[12]

Fatal cardiomyopathy results from chronic exposure to cobalt, acute poisoning brings nausea, vomiting and gastric mucosa.[15]A well-known poisoning incident occurred in Quebec City that killed 50 people from what was known as 'beer drinkers' cardiomyopathy, a result of cobalt poisoning.[12]

1.1.4 Nickel

Nickel is found in many ores in combination with sulfur, arsenic and antimony. Soils typically contain ~40ppm nickel compared with 2ppm molybedum, 10ppm lead and 6ppm arsenic.[16] Except for industrial exposures nickel is considered a relatively non-toxic element because of poor bodily absorption.[17] Nickel is essential although the precise role is not fully understood. Typical western diets contain 300-500μg daily[12] resulting in a 1.1-4.6μg L^{-1} blood nickel level.[18]

1.1.5 Zinc

Zinc is the second most abundant transition metal within the human body.[19] In 1934[20] zinc was shown to be essential for the normal growth of mammals. Zinc(II) has numerous cellular functions and is important in the various processes associated with cell activation and growth; these include gene expression, apoptosis, neurotransmission, signal transduction, enzyme regulation and catalysis.[21,22,23]

Major uses of zinc are in the production of non-corrosive alloys, brass and in galvanizing steel and iron products. Zinc oxide is also used in rubber production and in white pigment.[24] Release of zinc by industry frequently induces the release of other toxic metals such as cadmium and lead.[24]

1.1.6 Antimony

Antimony has two valencies, +3 and +5. Most antimony absorbed by the body is excreted rapidly.[24] A small portion however has a long half-life and is accumulated in the heart, lungs, thyroid, kidney and liver.[25,26] Antimony(III) is known to form thioantimonates with sulfide groups in cellular constituents.[12] Symptoms of acute and chronic antimony poisoning are similar to arsenic.

Antimony is a common constituent of metal alloys e.g. with lead and copper. It is also widely used for flame-retardants, in lead storage batteries, producing textiles and glass.[27]

Studies have shown daily food intake to be ~10-250μg. Ambient river water has been reported at 0.1μg L^{-1} in parts of Europe.[28] Cigarettes are another source of antimony estimated to be present at 0.1mg kg^{-1}.[29] Industrial exposures to airborne antimony, is frequently found in conjunction with exposure to other metals such as arsenic or lead.

1.2 Occurrence of Trace Metals in the Environment

Table 1-1 lists some selected trace metal water quality criteria presently in place including those that are a subject of this study, i.e. chromium, cobalt, nickel, copper, zinc, and antimony. The United States Environmental Protection Agency (USEPA) has developed Maximum Contaminant Levels for selected organic and inorganic compounds. This is the maximum permissible level of a contaminant to be delivered to a public water system and are defined by the best available technology and treatment techniques as well as toxicology.[30] The MCL's targets are legally binding whereas USEPA 'Criteria Maximum Concentration' targets are the recommended water quality levels for freshwater in general.

Table 1-1 Occurrence and permissible contaminant levels of selected trace metals for the United States and the European Union (μg L^{-1})[30]

Metal μg L^{-1}	Elemental Abundance On Earth[a]	USEPA Recommended Water Quality[b]	USEPA MCL[c]	Contaminant Occurrence Average (range)[d]	EU Guidelines[e]	WHO Guidelines[f]
Chromium	100	570 Cr(III), 16Cr(VI)	100	**242** (0.05-2000)	50	50
Nickel	75	470	52		20	
Copper	55	13	1300	**269** (0.5-2580)	2	2000
Zinc	70	120	5000			
Cadmium	0.2	2.0	5.0	**32** (0.01-50)	5	3
Mercury	0.08	1.4	2	**21** (0.1-3900)	1	1
Lead	12.5	65	15	**7.5** (0.1-1900)	10	10
Arsenic	1.8	340	50	**165** (0.28-1000)	10	10
Antimony	0.2	5.6	6.0	**3.0** (0.03-50)	5	20

[a]Average elemental abundance in the Earth's crust (mg kg^{-1})
[b]USEPA Criteria Maximum Concentration; recommended water quality criteria for freshwater (2002)
[c]USEPA Maximum Contaminant Level deliverable to the public water system (2003)
[d]USEPA Drinking Water Contaminant Occurrence (surface water) (2001)
[e]EU drinking water guidelines (2003)
[f]World Health Organisation drinking water guidelines (2003)

The United States has been monitoring levels of contaminants with the Toxics Release Inventory (TRI) program since 1987, some of the contaminant occurrence levels are listed in Table 1-1.[30] The European Union also implemented a similar program in 2001; the European Pollutant Emission Register. The EU target-levels for the above named trace metals are listed in Table 1-1 as well as drinking water guidelines set out by the World Health Organisation.

The table indicates that, in general, levels of arsenic, cadmium, chromium and mercury are above the desired MCL target. The occurrences ranges indicate that frequently there is a high variabililty in contaminant levels across the country.

1.3 Common Methods of Analysis

Common methods of analysis of trace metals include inductively coupled plasma mass spectrometry (ICPMS), X-ray fluorescence (XRF) analysis, flame atomic absorption spectrometry (FLAAS) and graphite furnace atomic absorption spectrometry (GFAAS), inductively coupled plasma atomic emission spectrometry (ICP-AES), electrochemical (EC) methods, capillary electrophoresis (CE) and neutron activation analysis.[31]

A survey of the United States National Environmental Methods Index (NEMI) indicates that standard methods approved by the USEPA, for the trace metals mentioned previously, use ICP-MS and ICP-AES for common multi-element analysis with detections limits of ~0.4μg L^{-1} and ~2μg L^{-1} respectively.[32] Other frequently used standard methods include; GF-AAS (0.4μg L^{-1}), FL-AAS (10μg L^{-1}) and XRF (1μg L^{-1}) (limits of detection).[32]

1.4 Speciation Studies of Trace Metals

Speciation of trace metals did not become widely studied by environmental scientists until the early 1970s.[41] It refers to the many physico-chemical forms of trace metals in the environment. These forms are very important for our understanding of the toxicological effects of a metal to biological systems.

The chemical speciation of copper, iron, cobalt, zinc, nickel and several other metals in natural waters is controlled by organic metal binding ligands.[36] Relatively little is known about the composition of the ligands involved.[36] Often, speciation studies can be complicated by the presence of several ligands.[36]

For example, the organic ligands that participate in complexation with copper(II) are put into groups L1 and L2; those ligands which bind strongly with copper(II) are in group L1, and those that bind weakly are in L2.[36,33,34] A recent study indicated that thiols are likely ligands for copper complexation in estuarine waters, but humic and fulvic acids are also thought to act as strong copper binding ligands in natural waters.[35] Speciation is often further complicated by redox reactions between oxidation states and the pH causing the formation of unstable, transient species.[36,37,38]

Identifying the reactive, labile fraction of the metal, which can be absorbed by an organism, is an important factor in speciation studies. This labile fraction is likely to correlate better with toxicological responses than total metal values, which are regularly reported.[39,40] Interest in speciation has coincided with advances in technology. Anodic stripping voltammetry (ASV) is a very specific technique used extensively in the development of speciation studies because it responds only to those metal species that are reducible at an electrode under the appropriate conditions, and hence is a measure of lability.[41]

The currently accepted model for bioavailability processes is illustrated in Figure 1.1.[41] There are two main approaches for this model. One is where the rate of biouptake across a cell surface is relatively slow compared to the rate of diffusion to the cell surface. The metal thus comes into pseudo-equilibrium with the metal in bulk solution, and therefore is under thermodynamic control.[41]

The other approach considers that the rate of internalization is rapid compared with the rate of diffusion. In this situation there is a concentration gradient surrounding the cell that may cause metal complexes to dissociate. Here, the metal biouptake is controlled by kinetic factors. There has been a polarizing of research opinions concerning the relative importance of these two descriptors.[41]

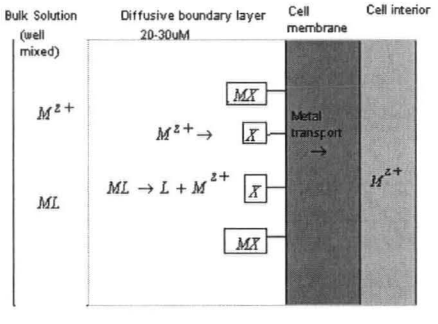

Figure 1.1 Model of metal ion uptake by a biological cell[41]

Most of the current information on metal complexation equilibria by dissolved organic matter comes from methods that rely on the titration of water samples by addition of known increments of metal, and following a suitable equilibration period, measurement of the equilibrium concentration of free metal by cathodic stripping voltammetry (CSV) with competitive ligand exchange (CLE),[42] by graphite furnace atomic absorption spectroscopy (GFAAS) of the extracted complex,[43,44] or by anodic stripping voltammetry (ASV).[45]

According to Buffle and co-workers, the importance of a quantitative understanding of dynamic speciation, must be recognised, by taking into account the kinetic features of the inter-conversion of different species.[46] In the end, the equilibrium approach is a simplified limiting case of the general dynamic situation in which chemical reactivity and transport of the various pollutant species also play crucial roles.[47,48,49]

Diffusion is a key transport process for both environmental systems and sensor functioning. Figure 1.2 describes the relationship between diffusion time scale and the key parameters of environmental and sensor systems.

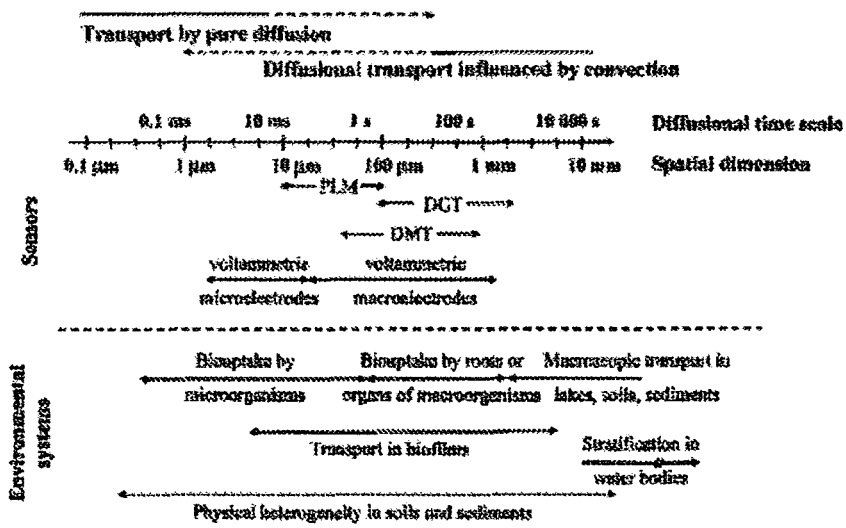

Figure 1.2 Schematic representation of diffusional time scales and spatial dimensions for a range of environmental processes and analytical sensors; Permeation liquid membrane (PLM), diffusive gradients in thin film (DGT), Donan membrane technique (DMT)[46]

For example, the diffusive gradients in thin film method (DGT)[50] gives the flux, *J*, of labile species from dividing the accumulated metal by the deployment time. A DGT sensor consists of a layer of hydrogel (0.4-2mm thick) overlying a layer of Chelex resin beads.[41] As the species diffuse through the gel, a concentration gradient is established in the gel layer. The lability and diffusion coefficients of penetrating complexes are determined

by the amount of metal collected in the resin.[41] This method has been used in studies to measure kinetically labile species of trace metals in natural waters.

Permeation liquid membranes (PLM) attempt to mimic the process of transport across a cell membrane.[51] The PLM is sandwiched between a sample solution and stripping solution. The membrane, consisting of a hydrophobic solvent and selective carrier molecule, measures the flux across the membrane.

1.5 Sensing Technology

Chemical sensing technology is concerned with the interplay between the chemistry of a target analyte and the creation of a physically measurable signal that is distinctive to the particular species using various methods. The signal may be electrical, optical, piezoelectric or thermometric. The largest of such fields is that of electrochemical sensing,[52] where chemical information is related to small electrical currents or potentials at an electrode transducer interface.

Electrochemical sensors are a focus of this research, as well as their potential application to environmental speciation. The importance of sensor technology is that it meets important monitoring criteria of real-time and in-situ detection of contaminants at the required low limits of detection.

1.5.1 Electrochemical Sensors

Electrochemical sensors represent an important class of sensors that use an electrode transduction element to transform chemical information from target analyte into electrical information. These sensors are relatively small, low cost and have a small power requirement, making them a potentially exciting alternative in the future of environmental monitoring.

Two main approaches for electroanalysis exist, potentiometry and voltammetry. Although both of these methods stem from electrochemistry, they use different routes to obtaining a signal. Potentiometry is known as a steady state measurement whereas in voltammetry applied potentials create a non-equilibrium condition at the electrode surface.

Traditionally, electrochemical sensors are known as a variety of potentiometric ion-selective electrodes, and using polarography for measuring heavy metals. Handheld glucose meters for diabetes patients are an example of commercially successful miniaturized electrochemical sensors. Such success has led to great interest in development of voltammetric monitoring for a range of trace metals, carcinogens and other organic pollutants.[53,54]

Modern instrumentation is capable of high sensitivity and low limits of detection in the parts per billion ($\mu g\ L^{-1}$) or even parts per trillion ($ng\ L^{-1}$) range using small handheld devices. Electroanalytical methods can also boast inherent capacity for metal speciation and applicability to a range of possible analyte, as well as promise of real-time on-line measurement and portability with minimal sample preparation needs.

Chapter 2

Sensing of Cobalt(II), Nickel(II), Copper(II), and Zinc(II) ions

2 Sensing of Cobalt(II), Nickel(II), Copper(II), and Zinc(II) ions

Sensing transition metal ions by optical or electrochemical methods can be achieved via a selective binding interaction between a ligand and the target metal ion. As described in Section 2.2, in a previous study by Congreve,[59] various sulfonamide ligands were designed for selective coordination of zinc(II), for possible use in luminescence and MRI applications. These ligands L^1-L^4 in Figure 2.8 are characterised in this study via potentiometric titrimetric analysis, defining the relevant protonation and metal complexation binding equilibria. In addition their use as ligands for incorporation into immobilized electrochemical sensor surfaces has also been screened.

2.1 Binding trends of Cobalt(II), Nickel(II), Copper(II), and Zinc(II) ions

In theory, a ligand is required that exhibits a selectivity profile for the target, for instance with the zinc(II) ion, that favours its binding in competition with, say, nickel(II) and copper(II). This is challenging, as the Irving-Williams series predicts a complex stability order of $Cu^{2+} >> Ni^{2+} > Zn^{2+}$, for typical N and O donor ligands.

2.1.1 Lewis Acid and Base Character

Trends in binding stability may be related to variations in ionic radii. Stability generally increases across a period and decreases down a group because of stronger metal to ligand bonds. An important general trend is defined by the Irving-Williams series,[55,56,57] this is partly caused by ionic radii changes but ligand field stabilization energy (LFSE) and Jahn-Teller distortion contributions can also play a key role.

$$Mn^{2+} < Fe^{2+} < Co^{2+} < Ni^{2+} < Cu^{2+} > Zn^{2+}.$$

Stability orders are also categorized by 'soft and hard' Lewis acid and base theory. Generally, soft acid metal ions bind with soft base ligands more strongly. Equally, hard acids bind well with hard bases. Hardness is a characteristic of polarizing electron donors / acceptors. This gives a more ionic character where electrostatic attraction is the source of stability. Softness is characterised by polarisable electron donor / acceptors giving the coordination bond more covalent character, in which the donor electrons fill metal ion *d*-orbitals for greater stability.[58]

Cobalt(II), nickel(II), copper(II) and zinc(II) ions are classed as 'borderline' acids. Therefore, stability is greatest with intermediate bases, and particularly with nitrogen donors. As the charge on the ion increases so does hardness. Therefore, chromium(III) is classed as a 'hard' acid, binding best with oxygen and nitrogen donors.

2.1.2 Coordination Geometries

Metals in solution are coordinated to donors or solvent at all times. Coordination number and the geometry preference of the metal ion is another potential means of creating selectivity for a particular ion.

2.2 Responsive Lanthanide Complexes for Luminescent Zinc(II) Sensing

The doctoral work of Aileen Congreve[59] involved the synthesis and evaluation of ligands forming metal complexes that might penetrate through cell membranes, and without harming the cell, would allow for the local role of metal ions, such as zinc(II), to be evaluated. Simple pyridyl sulfonamide

ligands were developed to selectively bind zinc(II) at physiological pH 7. The following Section 2.2.1 reviews related potential zinc probes.

2.2.1 Luminescent Zinc(II) Probes

A group of macrocyclic polyamines with appended fluorophores were developed as potential zinc probes. In the absence of zinc(II) the lone pair on nitrogen acts as an electron donor, quenching the fluorescence of the aryl fluorophore by intramolecular electron transfer. Fluorescence is enhanced when the amine nitrogens are coordinated by zinc(II) and this change may be related to the metal ion concentration. However, the nitrogen was protonated at physiological pH which also lead to fluorescence and competed with the binding of zinc(II).[59,60,61] Examples include azamacrocycles [12]aneN$_3$ and [12]aneN$_4$ with tosylamide L^5 and dansylamide flurophores L^7. Dansylamide-appended cyclen L^6 bound strongly with zinc(II) but again at neutral pH the ligand was protonated. The strong binding of sulfonamides to zinc(II) formed the basis for these structures seen in Figure 2.1, synthesized by Kimura and co-workers.[62,63,64,65]

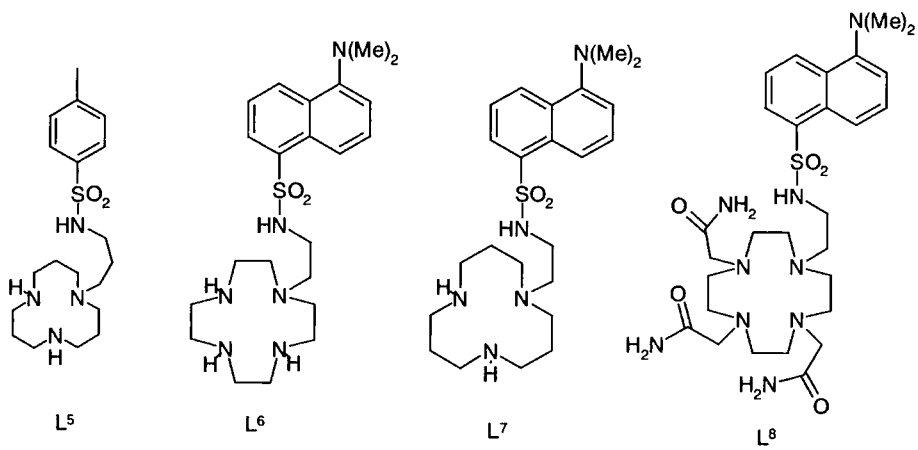

Figure 2.1 Azamacrocycles appended with fluorophores developed as potential zinc(II) probes

A 2-(9-anthrylmethylamino)ethyl-appended cyclen was synthesized and characterized for a new Zn^{2+} chelation-enhanced fluorophore and compared with a previously reported 2-anthrylmethylcyclen.[66,67,68] Despite strong

zinc(II) uptake with the previous L^9 ligand, its biggest drawback was a similarly occurring PET-retarded fluorescence attributed to uptake of two protons.[69]

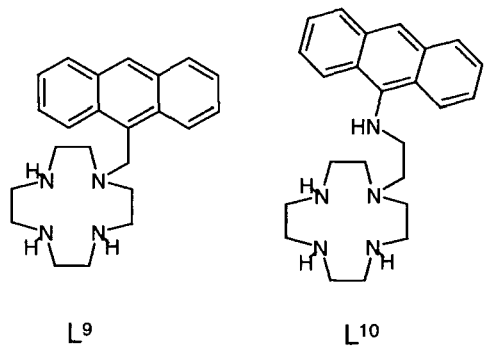

L^9 L^{10}

Figure 2.2 Anthryl fluorophore appended cyclens[69]

The new L^{10} ligand had an added site for binding with pK_a of 7.15 from the ethylamine pendant.[69] Complexation of Zn^{2+} with ligand L^{10} is strongly favoured over complexation with L^9, with $\beta_{ML} = 17.6$ compared to $\beta_{ML} = 11.6$.[69] And although the possibility of deprotonation of the dansylamide cyclen (L^6) resulted in increased stability with zinc(II) ($\beta_{ML}= 20.8$),[70] the greater acidity of ligand L^{10} enabled binding at neutral pH. The corresponding speciation diagrams of the complexation of zinc(II) according to protonation and formation constant data are seen in Figure 2.3.[69]

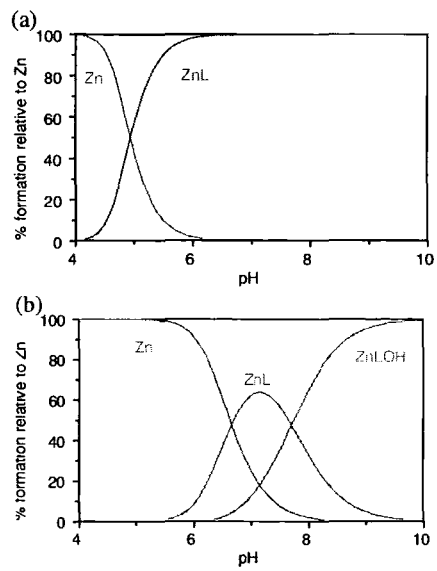

Figure 2.3 Speciation diagrams for (a) 5μmol L^{-1} zinc(II) 5μmol L^{-1} L^{10} and (b) 5μmol L^{-1} zinc(II) 5μmol L^{-1} L^9.[69]

A fluorescein-appended cyclen was also developed to selectively bind with zinc(II).[71] Fluorescence was enhanced 14-fold in the presence of micromolar concentrations of zinc(II). However, complex formation was too slow for use in biological diagnostics[59]. Naphthyl dendrimers attached to a cyclam core[72] formed luminescent complexes with zinc(II). The complexes formed were very stable, and therefore not ideally responsive to variable zinc(II) concentration,[59] Figure 2.4.

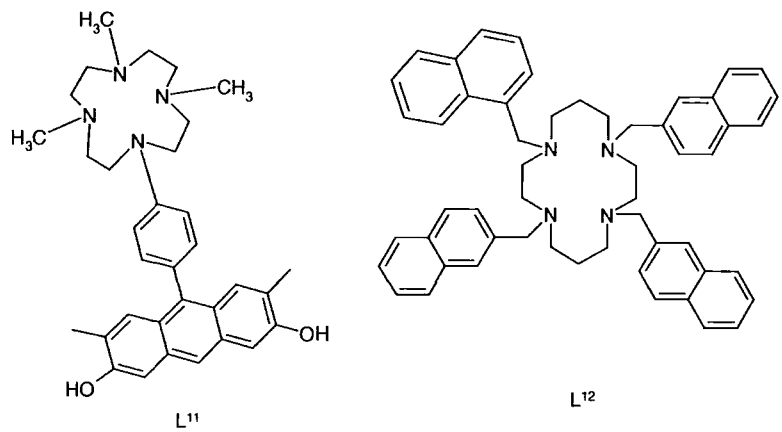

Figure 2.4 Fluorescein and naphthyl fluorophores attached to azamacrocyles

Fluoroscein appended acyclic amines that use the same principle as the cyclic amine zinc(II) probes have also been investigated.[59] Development of the *Zinpyr* family of zinc(II) probes such as Zinpyr-1 again had protonated amine binding sites at ambient pH that suppressed zinc(II) binding, Figure 2.5. Zinpyr-4 and Zinpyr-8 were reported to have more acidic pK_a. And Zinpyr-8 was reported to have an 11-fold increase in emission when bound to zinc(II). However the molecules were found to be impermeable to cell membranes. Figure 2.5.[59,73,74,75,76,77]

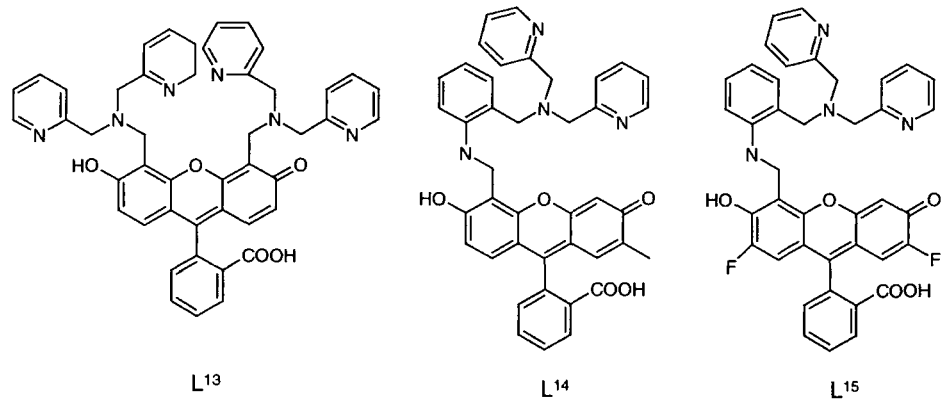

Figure 2.5 Acyclic fluorescent probes Zinpyr-1, Zinpyr-4, Zinpyr-8

The most widely used fluorescent probes for zinc(II) are at present based on 8-*p*-toluenesulfonamidoquinoline systems.[59,78,79,80,81,82,83,84] Examples are given by TSQ, Zinquin and 2-Me-TSQ[85, 86] (Figure 2.6). These ligands are cell permeable and were used to detect zinc(II) in the range 100 *p*mol L^{-1} to 10 nmol L^{-1}.[59,81,87,88]

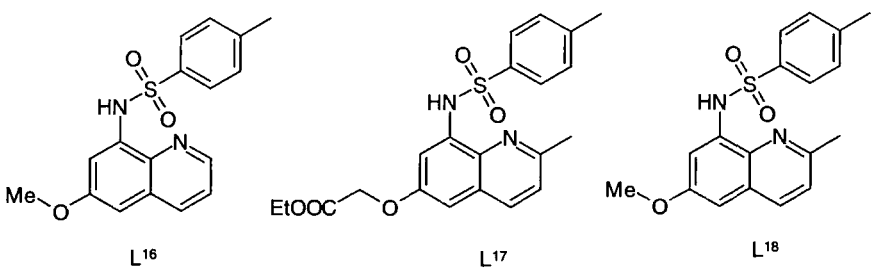

Figure 2.6 8-*p*-toluenesulfonamidoquinoline ligands; TSQ, Zinquin and 2-Me-TSQ

A study by O'Halloran[89] on a series of TSQ analogues, including 2-Me-TSQ has shown that while 2-Me-TSQ formed a neutral bidentate distorted [Zn(2-Me-TSQ)] tetrahedral complex, the methyl group on the quinoline inhibited square planar and octahedral complex formation, thereby creating a 'steric selectivity' leading to reduced copper and nickel complex stability.

Nakamura *et al*[90] studied protonation and binding equilibria of TSQ and trifluoromethylsulfonamidoquinoline analogues (Figure 2.7) with cobalt(II), nickel(II), copper(II) and zinc(II) (Table 2.1).

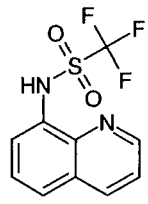

L^{19}

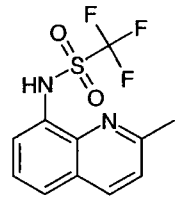

L^{20}

Figure 2.7 Trifluormethylsulfonamidoquinolines; CF_3SQ and 2-Me-CF_3SQ

Table 2.1 Protonation and binding equilibria of TSQ, CF_3SQ and 2-Me-CF_3SQ

*TSQ = 8-(4-Toluensulfonamide)quinoline, CF_3SQ = 8-(Trifluoromethylsulfonamido)quinoline, 2-Me-CF_3SQ = 2-methyl-8-(Trifluoromethylsulfonamido)quinoline **not available *** Conditions 30°C 75% dioxan with glass electrode

Ligand	Ion	β_{ML}***	K_{ML_2}	β_{ML_2}
TSQ*	H^+	11.9	2	13.9
	Co^{2+}	9.9	8.7	18.6
	Ni^{2+}	10.7	9.80	20.5
	Cu^{2+}	13.6	11.70	25.3
	Zn^{2+}	10.2	9.60	19.8
CF_3SQ*	H^+	7.6	<2	<9.6
	Co^{2+}	7.7	6.40	14.1
	Ni^{2+}	8.8	7.20	16.0
	Cu^{2+} **	-	-	-
	Zn^{2+}	7.7	6.30	14.0
2-Me-CF_3SQ*	H^+	8.2	2	10.2
	Co^{2+}	6.3	6.80	13.1
	Ni^{2+}	6.3	5.50	11.8
	Cu^{2+}	9.3	8.40	17.7
	Zn^{2+}	8.5	7.2	15.7

The acidity of the sulfonamide log K_1 increases from 11.9 to 7.6 with the CF_3 ligand, and binding stability for all metal ions also decreases. The

methyl appendage decreases stability of nickel(II) from β_{ML_2} =16.0 to 11.8, while zinc(II) stability is enhanced with 2-Me-CF_3SQ from 14.0 to 15.7.

A downside compared with macrocyclic probes is that mixed complexes can form with the bidentate ligand causing some uncertainty in luminescence measurement.[59] Other limitations include problems with solubility and the requirement of potentially damaging UV excitation for the tosylsulfonamide probes (TSQ λ_{abs}=334nm)[91,92].

2.2.2 Zinc(II) Ligand Design

Preliminary work by Aileen Congreve began with synthesis and characterization of a group of simple pyridyl sulphonamide ligands, L^1 - L^4 (Figure 2.8), designed to bind selectively with zinc(II) under ambient pH conditions.[59] A model ligand was sought from this series capable of forming a neutral complex with zinc(II) ions in the concentration range 100-0.1nM.

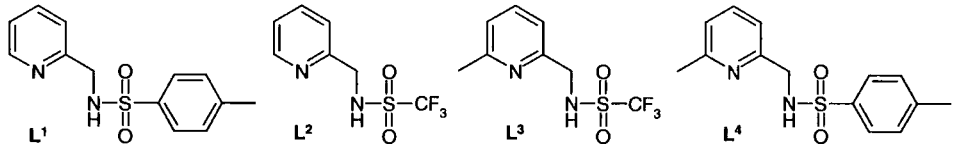

Figure 2.8 Pyridine sulfonamide ligands L^1 – L^4

The electronic donating ability of the sulfonamide nitrogen was varied, by altering the sulfonamide group from *p*-tolyl to trifluoromethyl. A neutral secondary sulfonamide is a weak acid that may be deprotonated in basic media to generate an anionic conjugate base. The protonation constant characterizing this equilibrium is around 12 while the trifluoromethylsulfonamide has pK_a of ~ 7.5.[90] Thus, the donor ability of the sulfonamide nitrogen may be controlled by variation of the nitrogen character. The α-methyl appendage in L^3 and L^4 sterically inhibits the formation of square planar or octahedral ML_2 species, e.g. with 2-Me-TSQ

Figure 2.8. This feature is expected to reduce the difference in stability between copper(II) and nickel(II) complexes relative to zinc(II).

2.2.3 X-ray Analysis

Following a series of x-ray structural analyses each complex was found to form a 1:2 M/L system with bidentate ligand coordination. With three exceptions, each complex adopted a four-coordinate distorted tetrahedral geometry. The degree of distortion of these complexes is primarily related to the 5-ring chelate bite angle that averaged 82°.[59]

The coordination geometry of zinc(II) and cobalt(II) was invariably distorted tetrahedral. This is the lowest energy arrangement around the metal and offers a slightly favourable ligand field stabilization effect in the case of cobalt(II). A similarly distorted tetrahedral arrangement is found with copper(II), except for the less sterically demanding ligand L^1, which forms a square planar complex. Nickel(II) is able to form a square planar $[NiL^1_2]$ complex and an octahedral $[NiL^2_2.EtOH]$ complex.[59] However with the α-methyl substituted ligands L^3 and L^4, nickel(II) also adopts a distorted tetrahedral arrangement.

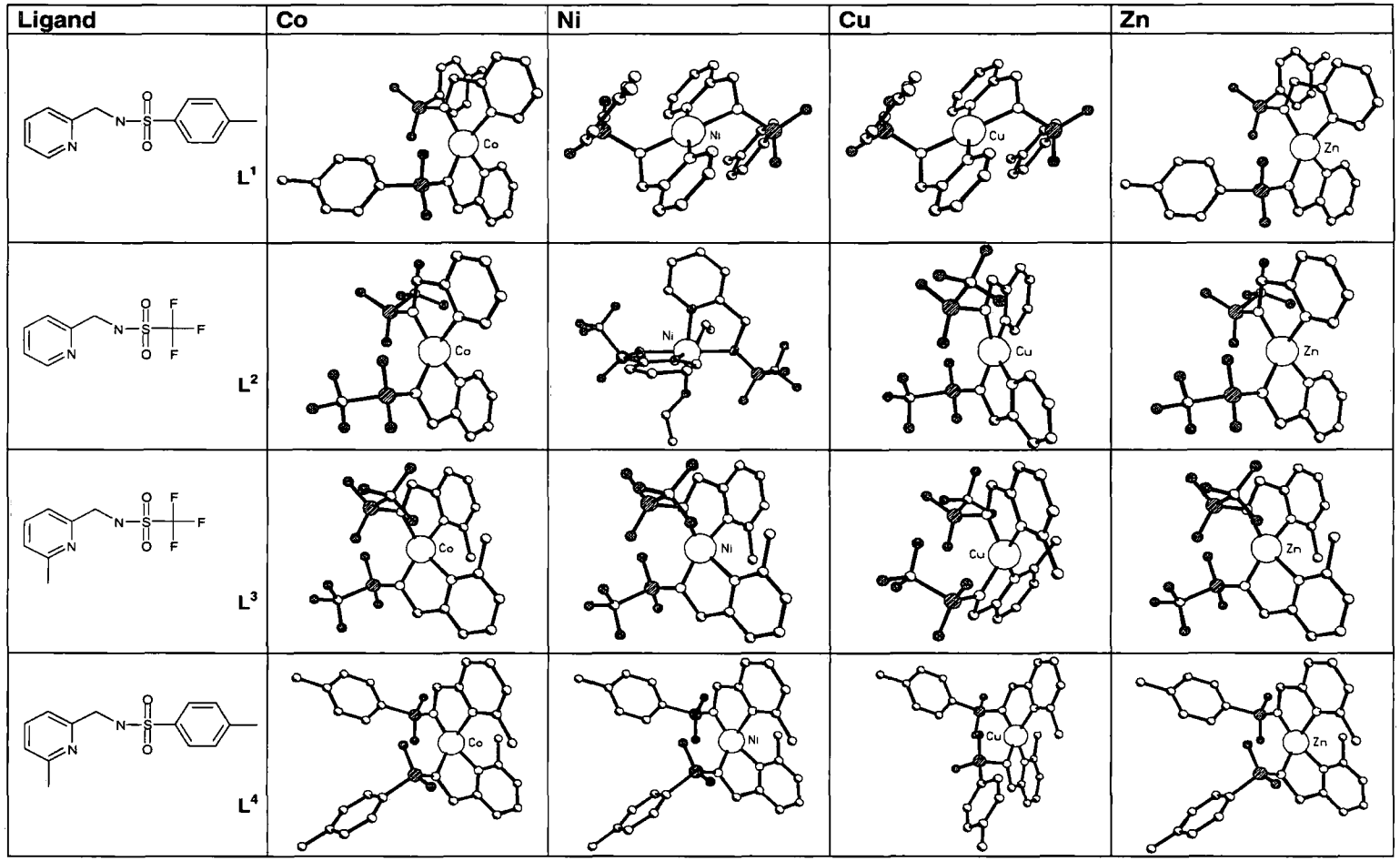

Figure 2.9 Crystal structures of the Co(II), Ni(II), Cu(II) and Zn(II) complexes of L^1 – L^4. [59]

2.3 Lability of Chromium(III), Copper (II), Zinc(II) Metal Ions

The kinetic lability of metal ion complexes is an important issue in sensing applications. Complexes that undergo rapid equilibration are termed 'labile', an aspect which may be independent of complex thermodynamic stability. Inert complexes can be slow to equilibrate (slow homogeneous kinetics), making measurements sensitive to changing concentration difficult. Slow heterogeneous kinetics may also create issues with producing an electroactive response at a particular electrode surface.

The chromium(III) ion is a very stable d^3 configuration. A high LFSE contributes to slow kinetics, and chromium(II) and chromium(IV) are usually unstable. A higher activation energy is therefore needed for ligand exchange. The rate of water exchange for chromium(III) aqua ion is $3x10^{-6}$ sec^{-1} compared with copper $8x10^9$ sec^{-1}.[93] The first divalent d-series metals are moderately labile with copper(II) most labile. Aqua ions in lower oxidation numbers tend to be very labile, consistent with a lower activation barrier to associative interchange.[93]

Table 2.2 Rate constants for exchange of water molecules with metal ions at 25°C[93]

Ion	k_1, sec^{-1}
Cr^{2+}	$7x10^9$
Mn^{2+}	$3x10^7$
Fe^{2+}	$3x10^6$
Co^{2+}	$1x10^6$
Ni^{2+}	$3x10^4$
Cu^{2+}	$8x10^9$
Hg^{2+}	$>10^4$
Al^{3+}	~ 1
Cr^{3+}	$3x10^{-6}$
Gd^{3+}	$2x10^9$

The labile copper(II) aqua ion has a moderate redox potential +0.33V (Table 2.3). It is convenient to analyse on a gold surface and carbon, although the use of bare solid substrates can be problematic due to adsorptive interferences and electrode regeneration. Copper(II) species are ideal metal species for testing new modified surfaces on gold or carbon substrates.

Analysis of zinc(II) is hampered by its high reduction potential, usually, at the edge of the negative potential windows. Traditional mercury electrodes are stable at this potential, because of high hydrogen overvoltage. Measurements at this potential are unable to be carried out with gold and platinum.[95]

Table 2.3 Selected standard electrode potentials[94]

Half reaction	E°, volts
$Cr^{3+} + e^- \rightleftharpoons Cr^{2+}$	-0.408
$Cr^{3+} + 3e^- \rightleftharpoons Cr$ (s)	-0.744
$Cr_2O_7^{2-} + 14H^+ + 6e^- \rightleftharpoons 2Cr^{3+} + 7H_2O$	+1.33
$Co^{2+} + 2e^- \rightleftharpoons Co$ (s)	-0.277
$Co^{3+} + e^- \rightleftharpoons Co^{2+}$	+1.808
$Ni^{2+} + 2e^- \rightleftharpoons Ni$ (s)	-0.250
$Cu^{2+} + 2e^- \rightleftharpoons Cu$ (s)	+0.337
$Cu^{2+} + e^- \rightleftharpoons Cu^+$	+0.153
$Zn^{2+} + 2e^- \rightleftharpoons Zn$ (s)	-0.763
$Sb_2O_5(s) + 6H^+ + 2e^- \rightleftharpoons 2SbO^+ + 3H_2O$	+0.581
$H_3AsO_4 + 2H^+ + 2e^- \rightleftharpoons H_3AsO_3 + H_2O$	+0.559

Chapter 3

Electrochemical Trace Metal Speciation

3 Electrochemical Trace Metal Speciation

3.1 Introduction

Traditionally, mercury electrodes have been used for voltammetric analysis. However, there is increasing desire to move away from use of mercury in voltammetry by replacement with chemically modified surfaces.[96] Chemically modified electrodes have been developed to adsorb analyte species on electrode surfaces with selectively coordinating ligands such as self-assembled monolayers on gold, covalent attachment on carbon, and polymer and membrane coatings.

Electrode poisoning limits widespread use of electrochemical monitoring from continual need for regeneration of the surface through cleaning and polishing that is time-consuming and difficult to reproduce.[95] There are three main ways of reducing electrode surface fouling problems.[96]

1. Reduce the time that poisoning substances are in contact with the electrode by flow techniques
2. Reduce the compatibility of the electrode surface with adsorption of poisoning substances by surface modification or membrane protection
3. Avoid the need for electrode regeneration by manufacturing disposable screen-printed electrodes.

The following chapter outlines many possible routes considered for in-situ electrochemical sensor methodology and their use in determining metal speciation in the environment. Section 3.2 introduces ion-selective electrodes as a means of directly measuring metal ions in solution, and the use of pH electrodes for measuring metal binding equilibria, and for selectivity evaluation of potential ligands for voltammetric sensing. A

number of voltammetric techniques were utilised throughout, such as cyclic voltammetry, differential pulse and square-wave waveforms as well as analysis strategies; anodic stripping and cathodic adsorptive stripping, which are described.

Various routes for ligand immobilisation on the electrode surface were investigated. L-cysteine on gold for analysis of copper(II), electro-polymerisation of pyrogallol on glassy carbon for analysis of antimony(III), and diazonium linkage for immobilisation of ligands for analysis of chromium(III), copper(II) and zinc(II). The above methodologies are outlined with recent developments in Section 3.5.

Electrochemical analysis of chromium(III) was difficult because of high d^3 stability. Chapter 7 describes the determination of chromium(III) in leather tanning waste solution via capillary electrophoresis and chelation with diethylenetriaminepentaacetic acid (DTPA).[97]

3.2 Ion Selective Electrodes

Thermodynamic arguments tell us that the gradient of activity across a membrane (of the analyte ions in the outer and inner solutions) produces a gradient of free energy:

Equation 3-1 $$\Delta G = -RT \ln\left(\frac{a_{i,sample}}{a_{i,\text{int}.solution}}\right)$$

where R is the universal gas constant (8.134J K^{-1} mol^{-1}), and T is the absolute temperature. The potential produced across the membrane corresponds to this free energy difference:

Equation 3-2

$$E = -\frac{\Delta G}{nF} = \frac{RT}{nF}\ln\left(\frac{a_{i,sample}}{a_{i,\text{int}.solution}}\right)$$

Since the potential of the electrode is fixed, and the activity of the ion in the inner solution is constant, the measured cell potential reflects the potential of the ISE, and hence can be related to the activity of the target ion in solution. Ideally, the response of the ISE should obey the equation:

Equation 3-3

$$E = E° + (2.303RT / z_i F)\log a_i$$

One of the most common classes of sensor is the ion selective electrode (ISE).[98] Detection limits are typically 10^{-6} – 10^{-8} mol L^{-1}, and are suitable in species modeling studies where metal concentrations are relatively high. In most ecotoxicological investigations ISEs do not have low enough limit of detection.[41] A compilation some of the commercially available ISEs, including linear ranges and limits of detection, is seen in Table 3-1.

Table 3-1 Types of commercially available ion selective electrodes with concentration ranges and limits of detection[99]

Analyte	Type	Typical concentration range (M)	Lower limit (ppm)
NH_3	Gas permeable membrane	$1–10^{-6}$	0.02
NH_4^+	Liquid membrane	$10^{-1}–10^{-6}$	0.02
Ba^{2+}	Liquid membrane	$10^{-1}–10^{-5}$	10
Br^-	Solid state	$10^{-5}–10^{-6}$	0.4
Cd^{2+}	Solid state	$10^{-1}–10^{-6}$	0.2
Ca^{2+}	Liquid membrane	$10^{-5}–10^{-7}$	0.02
F^-	Solid state	$10^{-5}–10^{-7}$	0.01

I^-	Solid state	$1–10^{-7}$	0.02
Pb^{2+}	Solid state	$10^{-1}–5 \times 10^{-6}$	1.0
NO_3^-	Liquid membrane	$1–5 \times 10^{-6}$	0.08
K^+	Liquid membrane	$1–10^{-6}$	0.04
Ag^+	Solid state	$1–10^{-7}$	0.01
Na^+	Glass sensing membrane	Saturated–10^{-6}	1 ppb
S^{2-}	Solid state	$1–10^{-7}$	0.003

Until recently it was accepted that lower limits of detection would remain around 10^{-6} mol L^{-1}, primarily because under normal conditions inner filling solutions were in the region of 10-100 mmol L^{-1} causing 'backward' flux of primary ion into the membrane and out into the interfacial region of the outer membrane.[100] It was found that sub-nmol L^{-1} was possible when the ion flux was reduced by reduction of inner filling solution concentration of primary ion, and by applying a biasing current that counteracts the flux.[101]

3.2.1 Equilibrium Determination with Potentiometric Titrations

Binding equilibria between ion and ionophore is determined by solving mass balance equations for total hydrogen [H_T], ligand [L_T] and metal [M_T]. Refinement of formation constants is possible if either free metal ion [M], free ligand [L] or free proton [H] concentration can be monitored with high accuracy over a wide concentration range.

The study of metal-ligand equilibria using a glass pH electrode has been common practice for many years.[102,103,104,105,106] Widespread application of glass electrodes has lead to dedicated software, such as *ESTA*[107,108] and *Hyperquad*.[185] In this study, potentiometric titrations were carried out to evaluate the suitability of various ligands for voltammetric sensing.

Modern software such as *Hyperquad* is equipped with species simulation programs such as *HySS* (Hyperquad Speciation & Simulation).[211] It allows one to easily calculate species formation curves from protonation and binding equilibria, and plot vs. pH, pM or pL. Modeling can be used extensively to probe into the likely species distributions at low concentrations common to speciation of trace metals in environmental samples.

3.3 Voltammetric Analysis Techniques

Voltammetry uses controlled-potential waveforms to induce a current response in relation to an applied potential. The use of certain waveforms can dramatically increase the sensitivity of a determination.

3.3.1 Chronoamperometry

Chronoamperometry involves increasing the potential in steps at the working electrode from which no faradaic reaction occurs to a potential at which the surface concentration of the electroactive species is effectively zero (Figure 3.1). The current response is given by the *Cottrell* equation, where F is the Faraday constant, A is electrode area, C is concentration, t is time, and D is the diffusion coefficient.

Equation 3-4 $$i_t = \frac{nFACD^{1/2}}{\pi^{1/2} t^{1/2}} = kt^{-1/2}$$

For sensing purposes using chronoamperometry, it is advantageous in that no stirring is necessary. It is useful for in-vivo bioanalysis where the potential at the electrode is pulsed repetitively.[109] Low current measurements are limited by background contributions from the charging current.

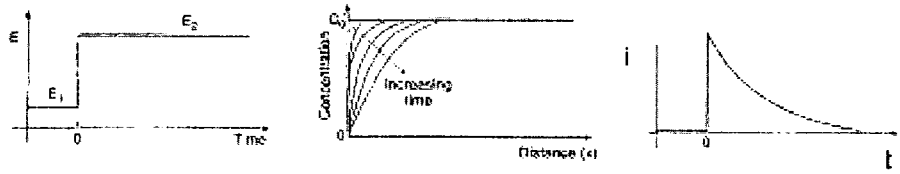

Figure 3.1 Chronoamperometric experiment; potential- time waveform, change of concentration profiles with time, and the resulting current – time response

3.3.2 DC Polarography

Polarography is a subclass of voltammetry that uses exclusively a dropping mercury electrode (DME). Because of the renewable, well-defined surface and wide cathodic range, polarography has been a widely used technique for measurements of many important metal species. The excitation signal used in DC polarography is a linearly increasing potential ramp.

DC polarography results in a sigmoidal-shaped current response curve. Current response is defined by the diffusion limited current plateau. The *Ilkovic* equation (Equation 3-5) describes this relationship, where i_d is diffusion limited current, and m is the mass flow rate of mercury.

Equation 3-5 $$i_d = 708nD^{1/2}m^{2/3}t^{1/6}C$$

For the reduction of labile (fast homogeneous kinetics) metal complexes, ML_p (Equation 3-6), the half-wave potential of the labile species is shifted to a more negative potential (vs. the free metal ion $E_{½}$). This reflects the additional energy required for the decomposition of the complex.

Equation 3-6 $$ML_n + ne^- \rightleftharpoons M(Hg) + nL$$

In DC polarography, the difference between the half-wave potential for the complexed and uncomplexed metal ion is given by Equation 3-7, as it relates to changing concentration of [L].[110]

Equation 3-7

$$(E_{1/2})_c - (E_{1/2})_{free} = \frac{RT}{nF}\ln K_f - \frac{RT}{nF}p\ln[L] + \frac{RT}{nF}\ln\left(\frac{D_{free}}{D_c}\right)^{1/2}$$

Here K_f is the formation constant. For reversible systems (with fast heterogeneous electron transfer kinetics), the experimental current response, *i*, and the potential of a polarographic wave can be described by the *Heyrovsky-Ilkovic* equation.

Equation 3-8

$$E = E_{1/2} + \frac{RT}{nF}\ln\left(\frac{i_d - i}{i}\right)$$

Equation 3-8 describes the potential shift as a function of *i*, in the form of the Nernst equation. Thus it follows that a plot of E vs. $\log[(i_d\text{-}i)/i]$ should yield a straight line with a slope of $0.05916/n$. The equations, above, have been recently expressed as a generalized theory by Cukrowski,[157] which exploits the Nernstian response in order to calculate $[M]_{free}$ and thus enable the solving of mass balance equations for complex formation equilibria using voltammetric data, as discussed in Section 3.4.

3.3.3 Pulse Techniques

Differential pulse voltammetry measures the differences in two currents, just before the end of the pulse and just before the pulse application. The difference is plotted against an increasing potential. The pulse is a factor of ten or more shorter than the period of the staircase. By subtraction of the capacitative current, limits of detection are improved to 10^{-8} mol L^{-1}. The differential pulse and square-wave waveforms with experimental reading and detection limits, are described below in Table 3-2.

Table 3-2 Voltammetric techniques used for trace-metal analysis and typical concentration ranges; v = Potential scan rate dE = Pulse amplitude; f = Frequency; td = Preconcentration time; ip = Peak current; Ep = Peak potential[125]

Technique	Potential function	Recorded function	Concentration range (mo L^{1})
Differential pulse voltammetry DPV	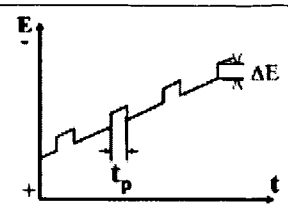	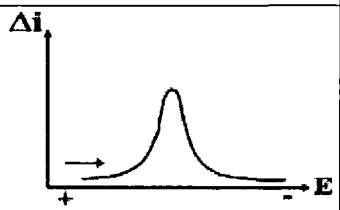	10^{-4}-10^{-7}
Square wave voltammetry SWV	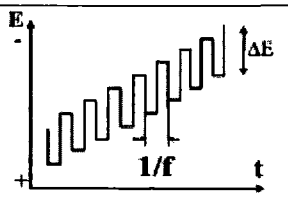	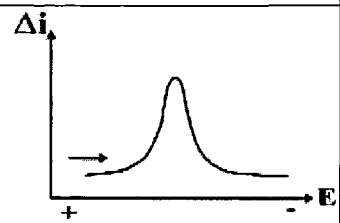	10^{-4}-10^{-8}

Square-wave voltammetry consists of a square wave superimposed on a staircase (Table 3-2). The currents at the end of the forward and reverse pulses are both registered as a function of potential. The capacitative currents are very effectively reduced. Analysis is faster and achieves lower limits of detection than differential pulse. Square-wave voltammetry is also advantageous in that oxygen does not have to be eliminated from solution because the forward and reverse current for oxygen reduction is equal giving a net zero current.

3.3.4 Anodic Stripping Voltammetry

Anodic stripping voltammetry (ASV) is the most widely used form of stripping analysis.[109] For this method metals are preconcentrated by electrodeposition onto the electrode, commonly a hanging mercury drop (HMDE) or mercury film electrode (MFE).

This method offers a great improvement in sensitivity of 10^{-11} mol L^{-1}. Traditionally, anodic stripping voltammetry (ASV) has been applicable to

mercury amalgam forming metals such as lead(II), copper(II), zinc(II), cadmium(II) (Table 3-3).[111,112,113]

Table 3-3 Stripping techniques used for voltammetric analysis of metal ions

Technique	Potential function	Recorded function	Concentration range ($molL^{-1}$)
Anodic stripping voltammetry ASV	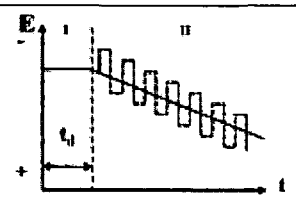	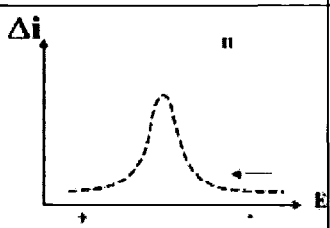	10^{-6}-10^{-11}
Adsorptive stripping voltammetry AdSV	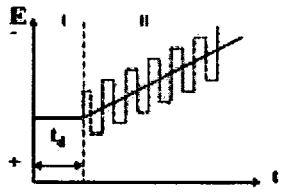	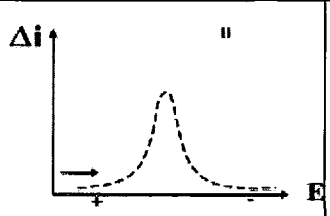	10^{-6}-10^{-12}
Potentiometric stripping analysis PSA	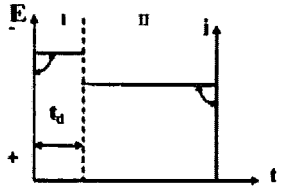	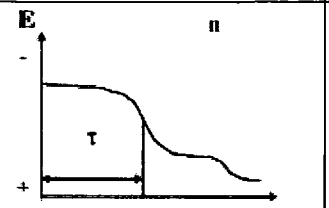	10^{-5}-10^{-9}

Several studies have shown that labile copper (determined by ASV) correlates with bioavailability.[114,115] Wider acceptability of ASV has, however, been hindered by several factors. Among concerns have been the problem of adsorptive interferences in contaminated samples, the possible artifacts of dissolved oxygen removal, and the unsuitability that this imposes on the in situ applications.[41]

3.3.5 Adsorptive Stripping Voltammetry

The adsorptive stripping (AdSV) technique, involves the addition of a ligand to a sample that forms an adsorbable complex with the metal of interest. The

complex accumulates by adsorption on the surface of an electrode, usually mercury, for a fixed time. The metal is reduced by applying a cathodic potential scan.

This technique is desirable in that a broader range of metals can be studied than just the amalgam forming ones. AdSV is highly sensitive and has found application in investigating the complexation of several metals by natural organic matter e.g. copper,[116,117,118] zinc,[119,120] lead,[121] iron,[122] and nickel.[123]

Much of the adsorptive stripping voltammetry for metal speciation studies has been developed by van den Berg and coworkers, with the use of competitive ligand exchange (CLE) prior to analysis.[124] This broadly involves the addition of a ligand and titration of the sample with added ionic metal, allowing appropriate equilibration before SV measurements.

AdSV has commonly employed mercury electrode surfaces as a way of retaining the pre-concentrated species,[95] but chemical modification of an electrode surface by a coordinating ligand is an alternate strategy increasingly employed.

3.3.6 Potentiometric Stripping Analysis

Potentiometric stripping analysis (PSA) is another voltammetric methodology worth considering for in-situ electrochemical sensing. It employs an alternate stripping strategy summarised in Table 3-3. The PSA method is advantageous in that de-aeration and stirring can be avoided. Additionally, it has been recently shown that PSA is significantly less sensitive to redox reversibility, and hence much less prone to artifacts due to adsorption.[125,126]

Wang and coworkers exemplified PSA's utility with a comparative analysis between PSA and ASV using bare gold-fibre microelectrodes to determine

the labile fractions of copper(II) and mercury(II) in an environmental sample.[127] Figure 3.2 shows determination of the labile fraction of both metals can be achieved with LOD of 0.22 μg L^{-1} and 0.04 μg L^{-1} for copper(II) and mercury(II) (lability represented 10% of total concentration[127]). In contrast SW-ASV was hampered by background current noise and irreversible adsorption on gold.[127]

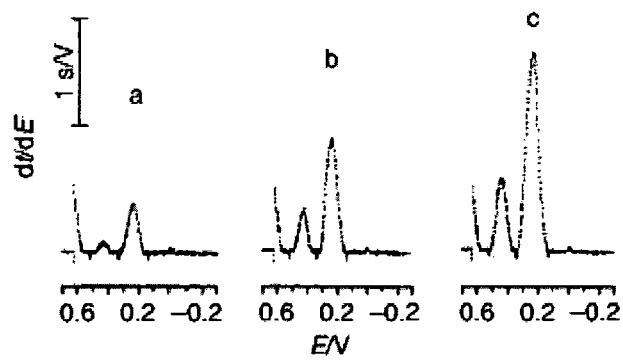

Figure 3.2 Stripping potentiograms following addition of (a) 0; (b) 1μgL Hg^{2+} and 2μgL Cu^{2+}; (c) 2μgL Hg^{2+} and 4μgL Cu^{2}. Deposition time 5 min at -0.30 V; constant stripping current, 0.1 mA; 'cleaning' for 30 s at +0.70V[127]

Palchetti's group used mercury-film screen printed electrodes (MFE-SPE) to determine copper(II), cadmium(II) and lead(II).[128] SWASV and PSA were investigated and it was found that the PSA technique was more sensitive and faster than SWASV (Figure 3.3).[128]

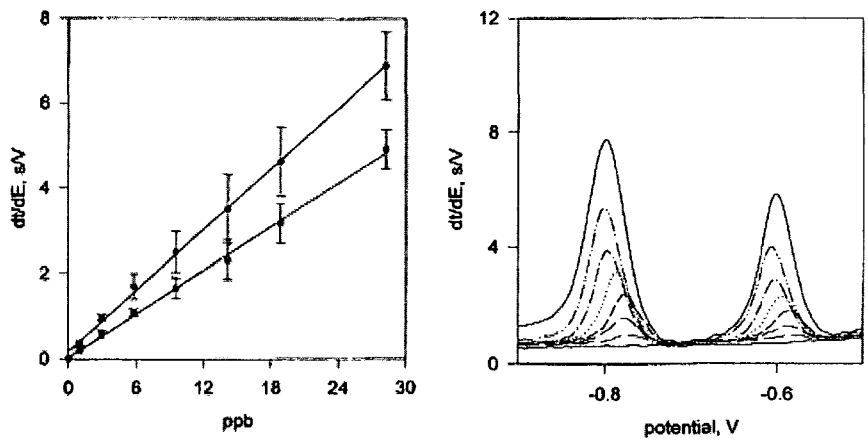

Figure 3.3 Lead and cadmium calibration curves. Acetate buffer 30mM, pH 4.7, 60s dep. time, rest 15s.[128]

3.3.7 Speciation Analysis with Ultramicroelectrodes

Generally, the advent of microelectrodes has been one of the major voltammetric advances in recent times.[41] Microelectrodes allow the issue of ionic strength in environmental analysis to be largely overcome.[129,130] Mercury coated microelectrodes have enabled fast, sensitive ASV in-situ sensors to be developed

In regards to speciation analysis, microelectrodes are very important. The decreasing radius of the electrode enhances the diffusional contribution of the measured current relative to the kinetic contribution, which is unchanged. The diffusion regime at a microelectrode is likely to be closer to that for unicellular organisms.[41]

3.4 Voltammetric Speciation using Acid-Base Titrations

Most of the current information on metal complexation by dissolved organic matter comes from methods that rely on titration of water samples by addition of known increments of metal, following a suitable equilibration period.[131,132,133,134]

All voltammetric theories and applications of speciation studies reported to date[135,136,137,138,139,140,141,142,143,144,145,146] involve the evaluation of the shift in position of the signal, but there has never been an attempt to predict a theoretically recorded signal (e.g. $E_{1/2}$ for DC polarography or E_p for differential pulse).[157] Whereas, in potentiometry, the theoretically predicted signal is a foundation of refinement operations employed in dedicated software, such as *Hyperquad*.[157]

The main approaches of analysis of voltammetric data, from which evaluation of formation constants has been performed, uses the shift or intensity of a voltammetric signal.[157] In a fully dynamic (fast homogeneous kinetics) M-L system and reversible electrochemical process (fast heterogeneous kinetics), analysis of the shift in voltammetric signal as a function of the excess of added ligand at fixed pH, was first used to evaluate formation constants of a single metal complex, ML_n. This began over 60 years ago with the Lingane equation,[146] and the method was expanded upon by DeFord and Hume to include several complexes formed in consecutive fashion.[147,148]

Among many theories[166], there is not a single contribution that involves mass balance equations and an analytical procedure similar to glass electrode potentiometry, e.g., acid-base titrations.[157] Analytical procedures employed, as well as exclusion of mass-balance equations, has lead to significantly restricted applications related mainly to the formation of metal complexes investigated with ligand titration at a fixed pH value.[157,149,150,151,152,153,154,155,156]

The refinement of stability constants involving the simultaneous solution of mass-balance equations is possible when either the free metal ion, ligand, or proton concentration [M], [L], or [H], respectively, can be monitored accurately during an experiment. Voltammetry is a dynamic, non-equilibrium analytical technique and therefore it does not allow a direct

measurement of free ion concentration. But voltammetric measurements do result in a signal in which the position and intensity depends on a solution composition.[157]

New methodology and theory of speciation by DC polarography and differential pulse has been described by Cukrowski,[157,158-163] and was recently tested on numerous metal-ligand systems that show varied polarographic behaviour. Fully labile (dynamic),[158,159,160] non-labile (inert)[161,162] and mixed[163] metal-ligand systems were investigated under typical glass electrode potentiometric conditions, i.e., at fixed $[L_T]$:$[M_T]$ ratio and varied pH.

The aim of the work by Cukrowski was to propose a simple mathematical treatment (Equation 3-9), on DC polarographic or differential pulse data, that resulted in a type of data that was suitable for refinement by dedicated potentiometric software, such as *Hyperquad*.[157,164,165,167]

In this current study, there was an attempt to implement this concept by simultaneously studying metal-ligand systems with both voltammetry (using an unmodified glassy carbon electrode) and glass electrode potentiometry.

Equation 3-9
$$(E(M)-E(comp))_{pH_i}-\frac{RT}{nF}\ln\left(\frac{I(comp)}{I(M)}\right)_{pH_i}=\frac{RT}{nF}\ln\left(\frac{[M_T]}{[M]}\right)_{pH_i}$$

In the above equation, E(M) and I(M) represent peak potential E_p and peak current i_p of free metal ion current response. E(comp) and I(comp) represent E_p and i_p at pH_i in the presence of metal complexes.[157] These parameters are related to [total metal] / [free metal ion] at pH_i.

This approach is a more generalized theory based on Equation 3-7, developed many years ago by Lingane,[110] that described a shift in potential taking place, with the labile metal current response.

The left-hand side of Equation 3-9 can be calculated directly from experimental voltammetric data. It accounts for the thermodynamic shift in potential, as well as contribution from the altered current intensity of the complex peak, by converting it to 'virtual' potential shift.

A plot of the left-hand side of Equation 3-9 versus pH generates the experimental complex formation curve This is used as the experimental objective function that has to be reproduced by the theoretical function, e.g., the right-hand side of Equation 3-9 illustrated below in Figure 3.4.[157]

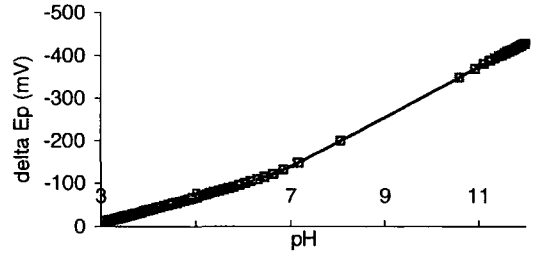

Figure 3.4 Theoretical complex formation curve calculated from the right-hand side of Equation 3-9 for Copper(II) / ligand L^1 equilibria

The change in the recorded current i_p can be attributed to a change in the diffusion coefficients of different labile metal complexes formed in succession.[166] This was an assumption made by Lingane, DeFord, and Hume.[167] Under this assumption, the thermodynamically expected position of the E_p signal along the potential scale can be calculated at any pH from the available experimental data with Equation 3-10.[157] This makes the approach theoretically capable of acting as a 'virtual' potentiometric sensor that is selective to any labile metal ion under investigation.[157]

Equation 3-10

$$\left(E(comp) + \frac{RT}{nF} \ln\left(\frac{I(comp)}{I(M)} \right) \right)_{pH_i} = E(virt)_{pH_i}$$

There are many components that can cause a change in the recorded voltammetric signal, which may complicate the interpretation of voltammetric data. The voltammetric signal can change due to the formation of an electrochemically inactive metal complex. The intensity of the recorded signal will also decrease with a decrease in the electrochemical reversibility.[164]

But for the purposes of the method proposed by Cukrowski, regardless of the cause of the variation in the intensity of the recorded signal, the term (RT/nF)ln(I(comp)/I(M)) can be interpreted as a fraction of a potential by which the recorded signal should have shifted more towards negative potentials, provided that there was no change in the value of the intensity of the recorded peak.[157]

3.5 Electrode Surface Modification Techniques

Chemical modification of an electrode surface can be an effective, mercury-free way to improving electrode sensitivity and selectivity for trace metal speciation. Numerous methods of modification include solid polymer electrolytes, membrane-modified electrodes, conducting polymers, sol-gel films, self-assembled monolayers, covalent ligand attachment, ceramic materials and enzyme modified electrodes.[168,169]

3.5.1 Covalent Attachment on Carbon

Monolayer modification on glassy carbon (GC) involves attachment via a covalent bond between the modifying reagent and a carbon substrate. Electrochemical modification includes oxidation of amines, reduction of aryl diazonium cations, oxidation of arylacetates and oxidation of the surface in the presence of alcohols (Figure 3.5).[170] Electrochemically assisted covalent modification of GC is a relatively recent development. Pinson *et al*[171] first

described the electrochemical generation of a solution radical that bound to a carbon surface in 1990.

Oxidation mechanisms for covalent attachment of reagent include, firstly, the oxidation of amines, whereby an amide radical is produced at the electrode surface and reacts with the carbon surface as seen below in Figure 3.5.[170]

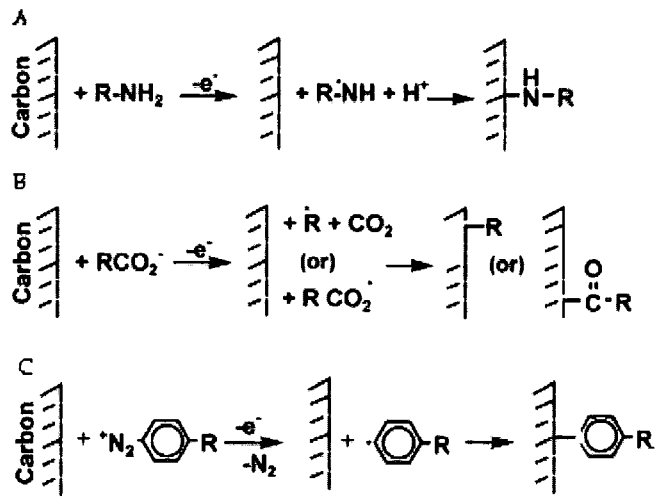

Figure 3.5 Routes for covalent attachment (a) amino (b) arylacetate (c) diazonium linkage on carbon[172]

Oxidation of arylacetates also creates stable monolayers.[173] Oxidation of the carboxylate results in elimination of CO_2. This yields an aryl methyl radical, which is then oxidized to create a C-C bond with the carbon surface (Figure 3.5), higher potentials can remove the monolayer.[173]

Another oxidative method involves modification in the presence of alcohols. At a positive potential (2V) the electrode is slowly pacified by the reaction. A mechanism proposed by Ohmori *et al* suggested aromatic radicals are produced from the carbon surface undergoing nucleophilic attack.[174,175]

Reduction of diazonium cations is a route that was investigated in this current study (Chapter 7). [170,176] Pinson's group explored immobilisation of

glucose oxidase for a potential sensor strategy. Firstly, phenyl acetate diazonium salt was grafted to the surface, then the enzyme was coupled via amine bond formation.[177] This reductive diazonium method of carboxylate formation created less background current via surface roughening incurred during oxidative modification.[170]

Another recent example involved benzo-15-crown-5 (B15C5) grafting to glassy carbon using diazonium linkage.[178] The modified surface was characterized with cyclic voltammetry (CV) and scanning tunneling microscopy (STM).[178] Formation constants of metal ions with the B15C5-GC surface were determined by impedence spectroscopy. The changes in capacitance at –0.16V at the electrode surface gave an order of $K^+ > Na^+ > Rb^+ > Li^+ > Cs^+$ with a distinct selectivity for K^+ ions.[178]

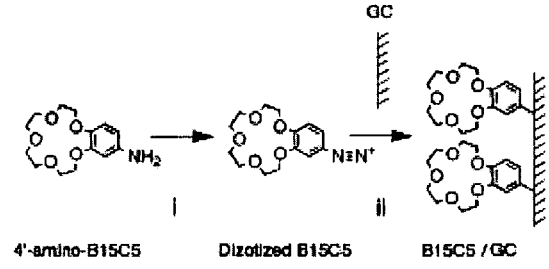

Figure 3.6 Scheme showing immobilization of B15C5 on a GC electrode by electrochemical reduction of in-situ generated B15C5 diazonium salt. (i) 1mM 4`-aminobenzo-15-crown-5, 2mM $NaNO_3$, 0.1M HCl, 4°C; (ii) potential cycling between 0 and –0.8V vs. Ag/AgCl, 25 cycles, 4°C[178]

This technique is desirable since electrochemically assisted methods are rapid, simple and inexpensive.[170] Covalently attached monolayers are stable to harsh conditions such as organic solvents, ultrasonication, elevated temperatures and moderate potential excursions, thus are more robust than thiol SAMs.[179] Loose packing as well as close packing is controllable with a potentiostat.[170]

Importantly, electrochemical means of modification have an important drawback compared to SAM modification; it is difficult to control multi-

layer formation. Radicals that are formed, may "stack up" by reacting with another reagent molecule already bound to the electrode. Careful control of electrode potential is therefore needed to alleviate this issue.

Another disadvantage of using glassy carbon compared with gold is the heterogeneous nature of the glassy carbon surface, in terms of basal-to-edge plane structure. Another important issue is that many analytes exhibit slower electron transfer kinetics at the carbon surface and thus the insertion of monolayer increases the distance over which electron transfer would occur.[170]

Chapter 4

Materials and Methods

4 Materials and Methods

4.1 Potentiometric Titrations

Thermodynamic binding stabilities with metal ions for prospective ligands have been evaluated by potentiometric methods. Preliminary measurement with varied solvents and background electrolyte was required to establish optimum conditions for ligand solvation and minimal interaction with supporting electrolyte. The effects of ionic strength and solvent interactions were examined and used to calibrate the pH electrode and enable accurate results.

4.1.1 pH Electrode

The activity of hydronium ion, H_3O^+, of the test solution was determined by measurement of the boundary potential difference at a glass pH electrode surface; illustrated in Figure 4.1. An Ag/AgCl(s) reference electrode completes the cell.

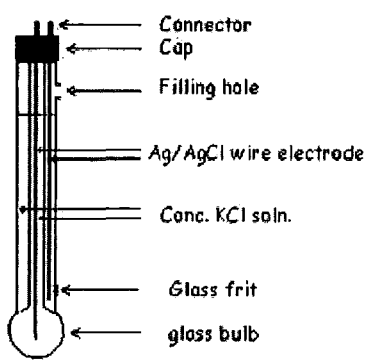

Figure 4.1 Diagram of a glass pH combination electrode with Ag/AgCl reference

There are five phase boundaries in the glass pH combination electrode; the cell diagram in Figure 4.2 describes these potential boundaries. The internal

reference potential, E_{ref1}, the external reference, E_{ref2}, and the internal potential, E_2, which develops at the inner glass membrane surface are constant.[183] The two other potentials are variable; the external potential of the glass membrane surface affected by pH and the liquid junction potential, which is present in all pH electrodes and is solution dependent.

The liquid junction potential comes from two electrolyte solutions in contact with each other at a junction. If the rate of ion transfer of the cation differs from that of the anion, a charge separation occurs at the junction.[180] The magnitude of the liquid junction potential can be calculated by the Henderson equation.[180] However, it is usual to keep the liquid junction small by addition of appropriate electrolyte in the two solutions.[180] The performance of an Ag/AgCl aqueous reference electrode in mixed solvents is good, and was thus used throughout the study.[180]

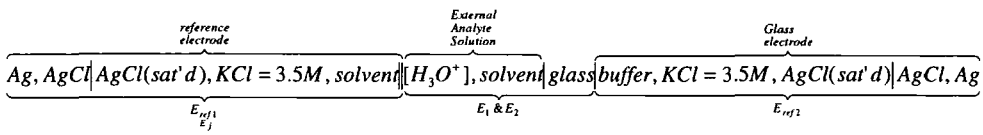

Figure 4.2 Cell diagram for measurement of pH[198]

The pH value was calculated using the Nernst equation (Equation 4-1). E^o represents constant potentials, E_{ref1}, E_{ref2}, and E_2. R is the gas constant, T is the temperature, n is the number of electrons, and F is the faraday constant. The Nernst equation when rearranged indicated how the experimental potential is subtracted from the reference potential. The liquid junction potential could be ignored so long as that it is acceptably small or at a constant value.

Equation 4-1 $$E = E^o - \frac{RT}{nF} \ln c_H \gamma_H - E_j$$

Equation 4-2

$$pH = -\log a_H = \frac{E - E^o}{0.0592} - \frac{E_j}{0.0592}$$

4.1.2 Determination K_w in Mixed Solvents

The use of water-alcohol media was necessary in pH titrations to improve solubility of ligands and complexes. The auto-protolysis equilibria in mixed solvents are more complex than in pure water. A binary solvent mixture contains up to four different proton transfer processes (Figure 4.3).[181]

$$H_2O + H_2O \rightleftharpoons H_3O^+ + OH^-$$

$$H_2O + ROH \rightleftharpoons H_3O^+ + RO^-$$

$$ROH + ROH \rightleftharpoons ROH_2^+ + RO^-$$

$$ROH + H_2O \rightleftharpoons ROH_2^+ + OH^-$$

Figure 4.3 Autoprotolysis equilibria of mixed solvents

However, the autoprotolysis of a mixed solvent media is written in the same way as with pure water according to IUPAC recommendations (Equation 4-3).[181,182] Therefore, K_w could be calibrated similarly to that of pure water.

Equation 4-3

$$K_{w_{ap}} = \frac{[RH_2^+][R^-]\gamma_{RH_2^+}\gamma_{R^-}}{x_{RH}^2}$$

4.1.3 Ionic Strength

It is important to evaluate the deviation from ideal behaviour of thermodynamic equilibrium caused by supporting electrolyte. Since the pH electrode measures activity of H^+, a_H, the resultant equilibrium quotient, Q, is related to the absolute (infinite dilution) equilibrium constant, K, by the correction term, γ the activity coefficient (Equation 4-4).[183] Figure 4.4 shows

increasing deviation of activity from concentration [H^+] as ionic strength increases, measured by a pH electrode.

Equation 4-4 $K = Q \cdot \gamma$

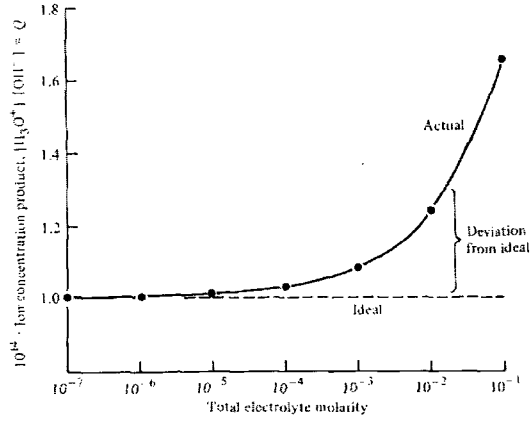

Figure 4.4 Ion product of water as ionic strength increases upon addition NaCl compared with ideal behaviour[183]

Ionic strength is calculated by:

Equation 4-5 $I = \frac{1}{2}\sum c_i z_i^2$

Ionic strength, I, changes throughout a titration as ionic species proportions change. In the course of titrations undertaken in this work, two sets of ionic strength scenarios were presented; one at 10 mmol L^{-1} [L], the other at 1 mmol L^{-1} [L]. Ionic strength ranges were calculated.

At 10 mmol L^{-1}, protonation equilibria titration solutions varied from I = 0.1 - 0.105 mol L^{-1} and complex formation equilibrium solutions varied from I = 0.1 - 0.115 mol L^{-1}. At 1 mmol L^{-1} calculated values are I = 0.1 - 0.1005 mol L^{-1} and I = 0.1 - 0.1015 mol L^{-1} for ligand and metal-ligand solutions respectively. The most significant departure from I = 0.1 is the 10 mmol L^{-1} solution containing metal ions at I = 0.115 mol L^{-1}.

4.1.4 p[H⁺] Buffer Conversion

Determination of pH is given by,

Equation 4-6 $$pa_{H^+} = -\log(c_H \cdot \gamma_H)$$

The pH scale may be converted to the p[H] scale with calculated activity coefficient γ of the reference solution to allow direct interpretation between $[H^+]$ electrode readings and [L] and [M] values in mass balance equations.

The activity coefficient was calculated by the Debye-Huckel equation at very dilute ionic strength, the extended Debye-Huckel equation (Equation 4-7) is reliable up to ionic strength of 0.01 mol L^{-1}, where z = charge, I = ionic strength and α = ionic size.[183] The Davies equation gives estimation of the activity coefficient at higher concentration.[183]

Equation 4-7 $$\log \gamma = \frac{-0.51 z^2 \sqrt{I}}{1 + (3.28 \alpha \sqrt{I})}$$

Potassium hydrogen phthalate was used as the reference solution. The buffering effect of potassium hydrogen phthalate (KHPh) decreases in solutions of decreasing water content. One reason is that the solubility is not sufficient in solutions of < 10 v / v%. Secondly the aprotic property of the solvent mixtures reduces the buffer capacity of KHPh.[180]

4.1.5 Equilibrium Determination

Acidified ligand solutions undergo deprotonation as pH increases, for example, with L^1-L^4 ligands deprotonation occurs from respective pyridine and sulfonylamide nitrogen atoms as the titration progresses. These reactions are conventionally described in terms of stepwise protonation constant, K, values and β values that represent additive stepwise constants; β_n = log $K_1K_2 \ldots K_n$ (Table 4.1).

Table 4.1 Definition of stepwise K and β protonation constants for diprotic acids[189]

K_1	K_2	$\beta_{2_{HL2}}$
$H^+ + L^- \rightleftharpoons HL$	$H^+ + HL \rightleftharpoons H_2L^+$	$2H^+ + L^- \rightleftharpoons H_2L^+$
$K_1 = \frac{[HL]}{[H^+][L^-]}$	$K_2 = \frac{[H_2L^+]}{[H^+][HL]}$	$\beta_{2_{HL2}} = \log\left(\frac{[H_2L^+]}{[H^+]^2[L^-]}\right)$

The key idea in acid strength is the ability of the conjugate base, through use of its molecular structure, to spread out the negative charge from the proton loss. The more this charge is dispersed, the easier it is for the proton to dissociate.[183]

Formation constants represent more basic constants first, followed by increasingly acid protonations. The opposite is true for acid dissociation constants, which present acidic constants first, and then increase in basicity value.

The general term used to represent the formation constant is:

Equation 4-8 $$\beta_{mlh} = \log\left(\frac{[M_mL_lH_h]}{[M]^m[L]^l a_H}\right)$$

Where m and l are positive integers or zero and h is positive for protonated species, negative for hydroxo complexes or zero. $[M_mL_lH_h]$ is the concentration of the complex species. [M] and [L] are concentrations of the uncomplexed reactant species and a_H is the measured proton activity.[184] The metal β and stepwise formation constants for ML_2 complexes are described in the same way as protonation constants (Table 4.2).

Table 4.2 Definition of stepwise K and additive β formation constants for ML_2 complexes[189]

K_{ML}	K_{ML2}	β_{ML2}
$M^{2+} + L^- \rightleftharpoons ML^+$	$M^{2+} + ML^+ \rightleftharpoons ML_2$	$M^{2+} + 2L^- \rightleftharpoons ML_2$
$K_{1_{ML}} = \frac{[ML^+]}{[M^{2+}][L^-]}$	$K_{2_{ML2}} = \frac{[ML_2]}{[M^{2+}][ML^+]}$	$\beta_{2_{ML2}} = \log\left(\frac{[ML_2]}{[M^{2+}][L^-]^2}\right)$

4.1.6 Equilibrium Constant Refinement with Hyperquad Analysis

Formation constants are calculated by fitting potentiometric data according to relevant mass and charge balance equations using the *Hyperquad* software program (versions 2000 & 2003).[185,186,187] In this program constants are varied in order to minimize the difference between calculated and observed values of –log [H^+]. Error estimates reported, are a measure of pH fit for applicable pH range.

For each experimental titration point, the following mass balance equations are valid:

Equation 4-9 $$T_M = [M] + \sum_{m=1}^{j} m\beta_{mlh}[M]^m[L]^l[H]^h$$

Equation 4-10 $$T_L = [L] + \sum_{l=1}^{j} l\beta_{mlh}[M]^m[L]^l[H]^h$$

Equation 4-11 $$T_H = [H] + \sum_{h=1}^{j} h\beta_{mlh}[M]^m[L]^l[H]^h + \frac{A_H}{\gamma - K_w / a_H}$$

Where T_M, T_L, and T_H are the analytical concentrations of metal, ligand and proton respectively, and are known from the quantities used to make up the test solutions.[184] γ is the activity coefficient for H^+, K_w is the dissociation constant of water, j represents the number of titration points and a_H is obtained from potentiometric titration.[184]

The unknown parameters are [M] and [L] for each titration point and the formation constants, β_{mlh}. The [M] and [L] variables are calculated in Hyperquad and β_{mlh} values are estimated.[184]

Hyperquad inputs required:

- Thermostat temperature
- Initial volume
- Titre error
- Slope factor – from titration program calibration
- Electrode error
- Total amount of ligand (in millimoles)
- Total amount of hydrogen – known amount of acid from acidification plus associated acid
- Concentration of OH^-, standardized from Gran's plot analysis of standard strong acid.

Equation 4-12 may be used as a method for approximating equilibrium constants from titration data for weak acid-strong base titrations.

Equation 4-12 $$pH = pK_{a_1} + \log(LH / LH_2)$$

At the first equivalence point, $[LH_2] = 0$, halfway to the first equivalence point [L] = [LH] and halfway to the second equivalence point [LH] = $[LH_2]$. Data in Figure 4.5 indicates that log $K_1 \approx 3$ and log $K_2 \approx 7.5$, which is in agreement with refined values of ligand L^2 protonation equilibria.

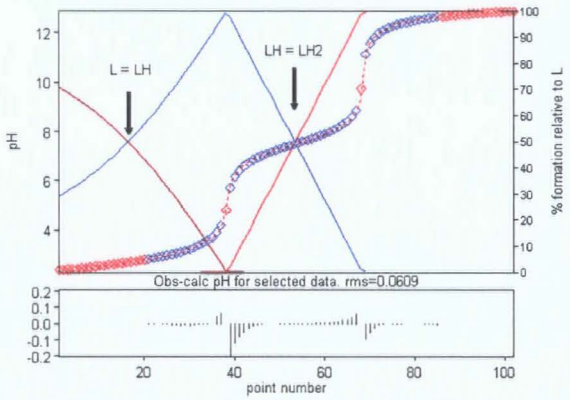

Figure 4.5 Hyperquad refinement showing [L] (brown), [LH] (blue), and $[LH_2]$ (red) species distribution used to predict protonation constants K_1 and K_2 for ligand L^2

In Hyperquad2003 multiple data sets can be analysed simultaneously to give an increased assurance in the calculated values.

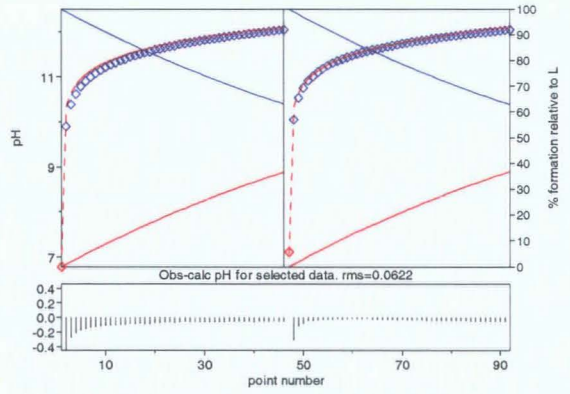

Figure 4.6 *Hyperquad2003* analysis of protonation curves for L^1 using simultaneous fitting for two data sets, blue= [LH], red= $[LH_2]$

Hyperquad calculates the best fit obtained by minimizing a weighted sum of squared residuals. The weighting scheme takes into account that near an end-point a small error in titre volume has a large effect on the pH measured, weights are reduced in this region.[192] Each residual is the difference between

calculated e.m.f, μ, and an observed e.m.f, X, expressed as sigma; defined in Equation 4-13.

Equation 4-13 $$\sigma = \sqrt{\frac{\sum (X-\mu)^2}{N}}$$

The calculated e.m.f., μ, is expressed in Equation 4-14; where EQ is the equivalence point for volume/e.m.f., n_1 is the number of protons of the ligand that can be titrated, E_x is the volume/e.m.f. that represents strong acid.

Equation 4-14 $$\mu = EQ - \frac{EQ}{n_1[L]}\left(\sum_{h=1}^{j} \beta_{mlh}[M]^m[L]^l[H]^h + \frac{A_H}{\gamma - K_w / A_H}\right) + E_x$$

In Hyperquad, a further statistical test of randomness Chi-Square is applied, where possible. This is based on the hypothesis that the residuals should follow a normal Gaussian distribution.[192] It is assumed that the residuals when divided by magnitude into 8 groups, each group should hold 1/8 of the residuals. If the distribution is approximately normal, the value will be around 12 or less.[188]

4.1.7 Metal Ion Hydrolysis

When a system forms an insoluble phase, the mass balance relationships employed with homogeneous solutions for total quantities of L, M and H are not valid. Usually precipitates "age" by rearranging themselves to form larger crystals over time. These aged precipitates have a different solubility than fresh ones, so there is no unique equilibrium constant that can be applied to the system.[189] Therefore, titration data is not used past the point where precipitation is discerned from a steady drift in pH or visually, and in the region where hydrolysis is expected by approximation from K_{sp} values (Table 4.3).[189]

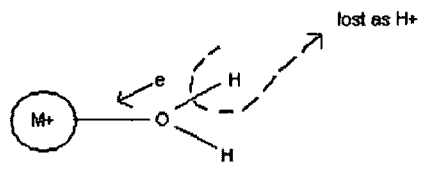

$$^{*}K_1 = \frac{[M(OH)^{(n-1)+}][H_3O^+]}{[M^{n+}][H_2O]}$$

$$K_1 = \frac{[M(OH)^{(n-1)+}]}{[M^{n+}][OH^-]}$$

$$M^{n+} + OH^{-n} \Leftrightarrow M(OH)_n \text{ (aq)}$$

$$^{*}K_{so} \qquad\qquad ^{*}K_{s1}$$

$$M(OH)_n \text{ (s)}$$

Trends in p^*K_1, the homogeneous binding equilibrium between M^{n+} and H_2O show a dependence on ionic charge and radius. M^+ species have values close to the protonation of water (Li^+= 13.9, Na^+= 14.7). While multiply charged species M^{3+} and M^{4+} show a much greater tendency to polarize the water molecule and protonate.[190] Transition metal species, M^{3+}, tend to be more acidic with lower p^*K_1 values than *sp*-block species and lanthanides; Cr^{3+}= 3.9, Fe^{3+}= 2.0 compared with Al^{3+}= 5.0, Sc^{3+}= 5.0 and Ce^{3+}= 9.3, Gd^{3+}= 8.6.[190] The increased acidity of the metal ion is also indicative of precipitation since this often follows the formation of hydroxide complexes.

The first row d-block M^{2+} species lie between M^+ and M^{3+} behaviour. This is indicated by K_{sp} values in Table 4.3. Solubility product K_{sp} gives an indication of the pH to expect hydroxide precipitation calculated by Equation 4-15.

Equation 4-15 $$K_{sp} = [M^{n+}][OH^-]\gamma_M \gamma_{OH}$$

Indicated below are the expected points of precipitation in free metal ions with I= 0.1 mol L^{-1}. However relying simply on the K_{sp} does not indicate the

actual point of hydroxide precipitation under the titration conditions. Principally the solvent mixture containing 80% methanol and the presence of ligands are expected to shift equilibrium to a more basic region.

Table 4.3 Solubility products of $M(OH)_2$ (s) and pH of formation in pure water

Precipitate	K_{sp}	$[OH^-]$	pH
$Co(OH)_2$	$10^{-14.8}$ [a]	$4.7 \cdot 10^{-7}$ [b]	7.67
$Ni(OH)_2$	$10^{-15.2}$	$3.0 \cdot 10^{-7}$	7.47
$Cu(OH)_2$	$10^{-20.4}$	$9.7 \cdot 10^{-10}$	5.98
$Zn(OH)_2$	$10^{-15.5}$	$2.7 \cdot 10^{-7}$	7.43
$Cd(OH)_2$	$10^{-14.0}$		

[a] Reference 183 [b] $[M^{n+}]= 0.01$ mol L^{-1}; $\gamma_M= 0.425$ and $\gamma_{OH}= 0.77$ at I = 0.1 mol L^{-1}, 25°C

4.1.8 Titration Apparatus

The glass pH semi-micro combination electrode (BDH 309-1025-02) was connected to a Molspin high impedance voltmeter.[191] Molspin pH meter and automated titrator was controlled by Molspin titration software (DOS V1.0),[191] and a more recent version of the software developed by Peter Gans (2004)[192]. The step motor of the Molspin dispenser was calibrated to 4752 steps/ml. Hydroxide was dispensed through a Hamilton 1ml Gas-tight syringe (#1001).

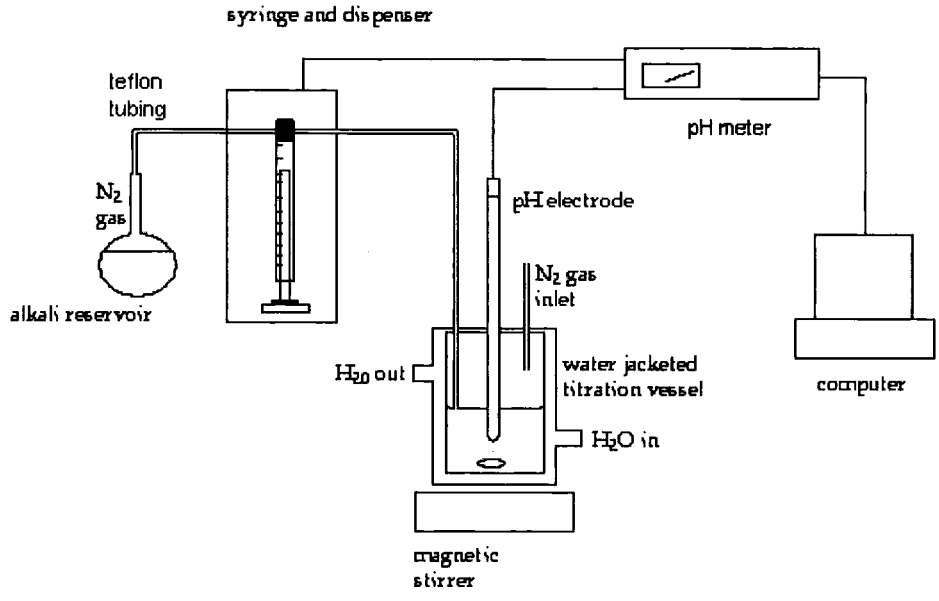

Figure 4.7 Schematic diagram of pH titration apparatus

The electrode was introduced to the 3ml titrant solution, allowed to equilibrate for a few minutes inside the 25°C water-jacketed titration cell. An atmosphere of nitrogen gas was created above the solution. The Teflon tubing (diameter 0.25mm) dispensing hydroxide was placed into the solution; this was necessary to ensure smooth titration data when adding aliquots of 1μL for 1mmol L^{-1} titrations.

The pH electrode was stored in supporting electrolyte containing 0.001mol L^{-1} $HNO_{3\,(aq)}$. If pH reading appeared to drift, reconditioning in 1M $HNO_{3\,(aq)}$ improved performance.

4.1.9 Solutions

Ligands 2-(*p*-Toluene sulfonylaminomethyl) pyridine (L^1), 2-(*p*-Toluene sulfonylaminomethyl)-6-methyl pyridine (L^4), 2-(Trifluoromethyl sulfonylaminomethyl) pyridine (L^2) and 2-(Trifluoromethyl

sulfonylaminomethyl)-6-methyl pyridine (L^3) were synthesized by Dr. Aileen Congreve.[59,193]

Water was purified by the 'Purite STILL plus' system. Stock 0.05 mol L^{-1} metal solutions are prepared with reagent grade cobalt(II), nickel(II), copper(II), zinc(II) and cadmium(II) nitrate salt (Aldrich). Tetramethylammonium nitrate, NMe_4NO_3, and potassium nitrate 0.1 mol L^{-1} salts (Aldrich) were used as background electrolyte.

10mmol L^{-1} or 1mmol L^{-1} solutions in 3ml volumes were titrated against 0.1mol L^{-1} NMe_4OH 80% MeOH, made from 10% 1mol L^{-1} aqueous stock (Aldrich) diluted to 0.1mol L^{-1} [OH^-] with degassed H_2O from boiling under N_2 gas for at least 5min.[194]

A 3ml glass bulb pipette was used to transfer solution to the titration vessel, the pipette was calibrated according to 80%MeOH, 20%H_2O density, the 3.0947ml exact volume calculated was used in subsequent mass balance equations.

Stock phosphate buffer pH 7.0 consisted of 30.5ml 0.2 mol L^{-1} Na_2HPO_4 and 19.5ml 0.2 mol L^{-1} NaH_2PO_4 per 100ml.[195] Fresh stock solutions of sodium and disodium phosphates were made from dried salts. Potassium hydrogen phthalate buffer pH 4.008 was made from high purity salt (99.9%, Aldrich).

4.1.10 Gran's Plot Alkali Standardisation

Hydroxide was standardized with 'Convol' 0.01mol L^{-1} HNO_3 (aq) (BDH). Concentration [OH^-] was calculated with equivalence volume, V_e, of the titration curve where [H^+] = [OH^-] extrapolated by Gran plot technique[196,197] and calculated by Equation 4-16 where n_H is moles H^+, and C_H is concentration of H^+.

Equation 4-16 $$\frac{n_H}{V_e} = C_H$$

Titration software settings in 'Molspin Titrator'[192] are 0.6ml volume to add, 'medium' reaction rate, and precision of 0.02 pH, 10μL aliquots with a 3ml titration volume.

In Chapter 5, potentiometric titration curves in most instances are displayed with x-axis converted to 'moles of alkali added per mole of acid'. This allowed for direct comparison between titrations by correcting any discrepancy caused by fresh solutions of alkali having slightly different concentration. Each titration point of OH volume, V_n is multiplied by the standardized alkali concentration, C_{OH} given by Gran plot[196,197] and divided by the known amount of acid present in test solution (Equation 4-17).

Equation 4-17 $$\frac{V_{1_{OH}} \cdot C_{OH}}{n_H} = n_{1_{OH}} / n_H \, present$$

Air bubbles were excluded from the hydroxide dispenser, and hydroxide was ready to dispense at the first increment. Bubbles could also develop at the tip of the electrode and thus, alter pH readings.

4.2 Voltammetric Analysis

The system in Figure 4.8 describes the circuit used in voltammetric measurement. The cell is made up of three electrodes immersed in stirred solution with supporting electrolyte. The working electrode was a 3mm diameter glassy carbon disk embedded in solvent resistant plastic body (7.5 cm length x 6 mm OD) (MF1000, Bioanalytical Systems). Reference electrode was an aqueous Ag/AgCl electrode (Bionanalytical Systems) in contact with solution. The third electrode was a counter electrode 1cm^2 platinum foil.

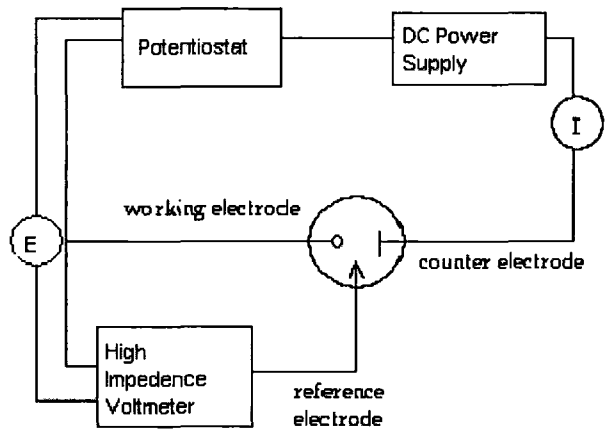

Figure 4.8 Three-electrode cell connected to a potentiostat used for voltammetry[198]

A potential was applied to the working electrode E_{we} measured *vs.* the reference electrode potential E_{ref}. The potential measured in volts is varied with a potentiostat, which measures the resultant current *i*. Current is passed between the WE and the CE. The RE potential was constant at its open circuit value.

The required E_{WE} (Ag/AgCl) is given to the potentiostat, when the circuit is complete, the P=E_{WE} (Ag/AgCl) is measured. The potentiostat will cause a change in the DC power supply so that P remains equal to E_{WE} (Ag/AgCl).

A Princeton Applied Research potentiostat Model 263 and Varied Multi-Potentiostat Version 1.0 (Princeton Applied Research) was used for electrochemical measurement controlled with software 'PAR' Dos version 2.03 and 'ECLab' (Princeton Applied Research) for the respective potentiostats. All experiments took place in a faradaic cage to reduce outside interferences. Electrodes were polished with alumina slurry and 10μm diamond paste on nylon pads (BAS), following by immersion in ultrasonic bath with deionised water.

4.2.1 Cyclic Voltammetry

Cyclic voltammetry was used primarily as a diagnostic tool, made of triangular waveforms seen in Table 3-2. The basic response to a linear sweep of potential is a peak shaped curve, as current begins to rise, when $E_{½}$ is reached, a concentration gradient is produced which pulls in more electroactive species resulting in a peak until depletion effects set in and the current begins to fall, Figure 4.9.

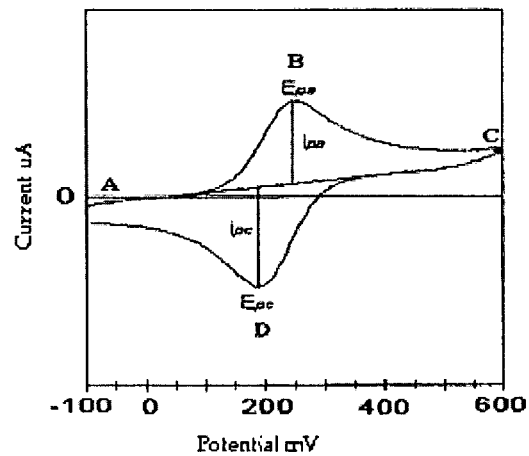

Figure 4.9 Cyclic voltammogram for reversible redox reaction

The total current obtained is a sum of contribution from faradaic reaction and a capacitative contribution described according to:

Equation 4-18 $$I = I_c + I_f = C_b \cdot \frac{dE}{dt} + I_f = \nu \cdot C_b + I_f$$

Here I_c and I_f is capacitative and faradaic current, ν is scan rate, and C_b is bulk concentration.

4.2.2 Differential Pulse Voltammetry

Pulse waveforms described in Table 3-2 include normal pulse, differential pulse and square-wave. These voltammetric techniques are required to

separate faradaic current from background interference, and thus obtain lower limits of detection.

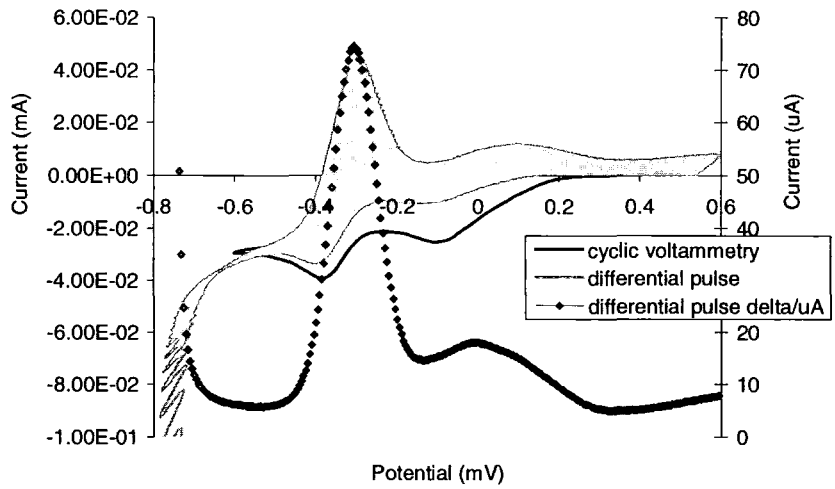

Figure 4.10 Cyclic voltammetry and differential pulse of [CuL$^1_2$] at pH 6.43

Figure 4.10 illustrates the differential pulse sampled current and linear cyclic voltammetry current along with ΔI curve in microamperes for voltammetric speciation of [CuL$^1_2$] complex. The sampled current in yellow shows the high and low samples taken at the end of each potential step resulting in increased sensitivity.

4.2.3 Electrode Modification

4.2.3.1 Diazonium Modification on Glassy Carbon Electrodes

A glassy carbon electrode was cleaned and polished thoroughly with 1μm diamond paste (BAS). An ultrasonic bath in deionised water ensured that polishing residue was removed.

Initial modifying solutions consisted of 0.7 - 1.8 mmol L^{-1} 4-nitrobenzenediazonium tetrafluoroborate in acetonitrile (ACN) with a 0.1 mol L^{-1} tetraethylammonium perchlorate (NEt_4ClO_4) or 0.1 mol L^{-1} NBu_4BF_4 supporting electrolyte, as reported by Pinson *et al.*[199,200,201202]

Diazonium salt was kept under argon atmosphere at 4°C. The electrolysis time and potential were varied. After modification the electrode was rinsed with deionised water, then sonicated with ethanol and rinsed with acetone and reinserted into blank dry ACN 0.1 mol L^{-1} NBu_4BF_4 solution or 0.1 mol L^{-1} NMe_4NO_3 aqueous solution.

4.2.3.2 Electro-Polymerisation of Pyrogallol

A poly(pyrogallol) modified glassy carbon electrode was made from the method used by Khoo.[203] The gce was polished with alumina slurry, rinsed with deionsed H_2O and sonicated for 5 mins. The modified electrode was prepared by immersion in 10 mmol L^{-1} pyrogallol solution 0.1 mol L^{-1} pH 7.0 phosphate buffer. The potential was swept 10 times in CV mode from –0.1V to +1.5V at 20 mVs^{-1}. Electrode was then rinsed with H_2O, immersed in blank phosphate buffer and cycled 10 times at 100 mVs^{-1} from –0.1V to 1.5V to unreacted ligand. The electrode was stored in open air.

Deposition solution consisted of antimony in pH 5.5 buffer 0.05 mol L^{-1} 2-(N-morpholino)ethanesulfonic acid (MES). At open circuit, antimony(III) was deposited for 3mins in a stirred solution, then rinsed and transferred to fresh, de-aerated, unstirred stripping solution of 1 mol L^{-1} HCl and 0.1 mol L^{-1} KCl for voltammetric analysis; typically with differential pulse at –0.4V to 0.3V. After the analysis sweep, the potential was held at 0.3V for 3 mins as a cleaning step.

4.2.4 Voltammetric Spectral pH Titration

A combination of UV/visible absorbance, differential pulse voltammetry, cyclic voltammetry and potentiometry measurement was taken simultaneously using a simple flow apparatus (Figure 4.11).

Absorbance was measured from light source (Ocean Optics) to spectrometer (Ocean Optics) with fibre optic cable through a quartz flow cell (BAS) with 1cm path length (Figure 4.11). Background dark and background light (80% MeOH and 0.1 mol L^{-1} KNO_3) was calibrated after the lamp had equilibrated for 10 minutes. Spectrometer settings included integration time = 10, Average = 10, and boxcar smoothing = 20.

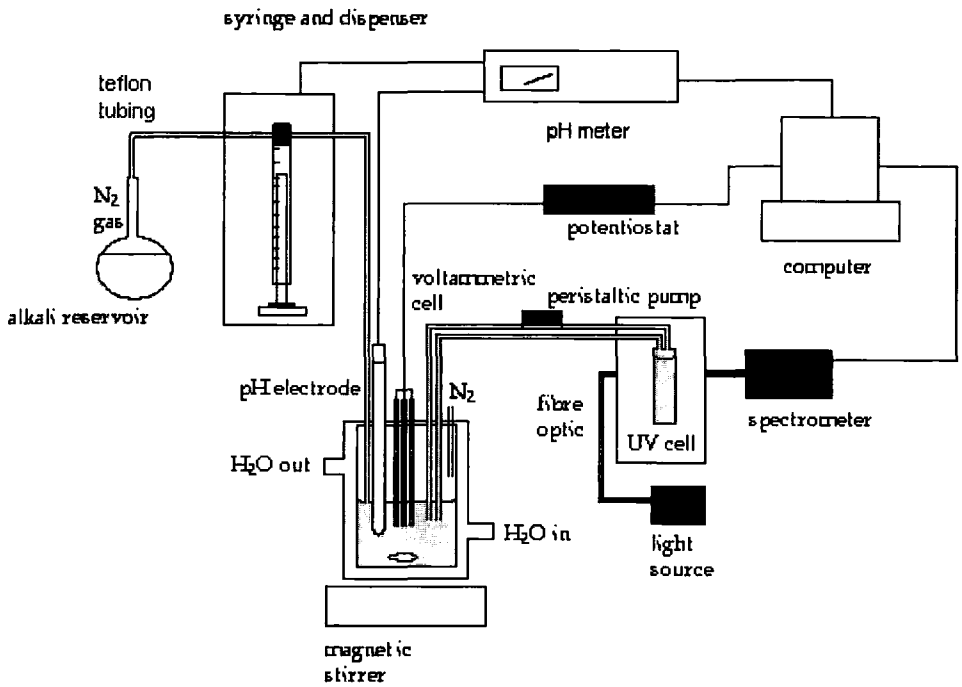

Figure 4.11 Spectrometric-voltammetric pH titration apparatus

The voltammetric cell, counter electrode, and reference electrode and a well-polished GCE were cleaned regularly. A 5 and 10 mmol L^{-1} (M/L) reactant solution in 80% MeOH and 0.1 mol L^{-1} KNO_3, with no acidification, was bubbled with N_2 for 10 minutes (Figure 4.11). *ECLab* software[204] with a varied multi-potentiostat Version 1.0 (VMP) from Princeton Applied Research was used to measure DP and CV curves in succession.

The electrode was calibrated with fresh buffer to p[H] scale, temperature 25°C and fresh standardized alkali was used to control pH. *Molspin Titrator* software and dispenser controlled addition of alkali.

4.3 Capillary Electrophoresis

Capillary electrophoresis (CE) with UV detection was applied to examine the speciation of chromium(III) in leather tanning waste solution and compared with established spectroscopic and MS methods.[97]

All CE measurements were performed with a Quanta 4000 (Water Division, Milford, USA) system with UV detection and a negative high-voltage power supply.[97] The electrophoretic fused silica capillary (Supelco, Bellefonte, USA) was 67cm in total length, 50cm to detector, 75μm ID and 375μm OD. An electro-osmotic flow modifier, tetradecyltrimethylammonium hydroxide (TTAOH) (Aldrich), was used to reverse the capillary wall charge to negative. A 0.5mmol L^{-1} solution of TTAOH in 20mmol L^{-1} pH 8.0 phosphate buffer was prepared from tetradecyltrimethylammonium bromide (Aldrich) using anion-exchange resin and used as the carrier electrolyte. The capillary was equilibrated at 20psi in forward rinse mode with water, 0.1 mol L^{-1} NaOH and carrier electrolyte all for 5min at the beginning of each day. Between all electrophoretic separations the capillary was rinsed for 2min with electrolyte.

The method followed was analogous to that of Pozdiakova *et al*[205]. All calibration, background and chromium leather tanning waste sample measurements had the following experimental conditions: -15 kV voltage application, 20s injection time, 10min analysis time, 0.01 sensitivity setting, 20mm/min recorder speed and 214nm wavelength absorbance detection, unless otherwise stated. Atomic absorption spectroscopy measurements were carried out by Krzysztof Kilian at the University of Warsaw using a Perkin-Elmer 3100 spectrometer.

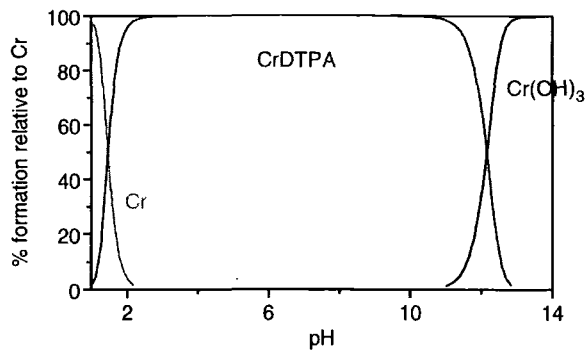

Figure 4.12 Species distribution of $[CrDTPA]^{-2}$ at 1:1 mmol L^{-1}

The complexant diethylenetriaminepentaacetic acid (DTPA) was used to convert Cr^{3+} to an anionically charged ion, $[CrDTPA]^{2-}$. Chromium(III) and DTPA form a stable 1:1 complex, which is preferred in capillary electrophoresis over EDTA and CDTA since the migration time is faster with the doubly charged anion.

The complex formed has a stability constant of $K_1=22.05$ [206] and is stable throughout much of the pH range (Figure 4.12), DTPA is deprotonated in the presence of chromium(III) and strongly bound below pH 2 and remains stable until pH 11. Since chromium is kinetically very stable (from its d^3 valence configuration) the complex formed very slowly, therefore $[CrDTPA]^{2-}$ was fully complexed only by boiling for 5 minutes.

4.4 Spectroscopy and Chromatographic Determinations

Chromium UV/Vis absorbance was measured by an UltroSpec spectrophotometer (Pharmacia Biotech); samples were placed in Hellma 10mm quartz precision cells (type 110-QG), and *Swift* software program (Pharmacia Biotech) was used to analyse the data.

Inductively coupled plasma-mass spectrometry (ICP-MS) was used to analyse chromium leather tanning waste solution. This was carried out by

Chris Otley (Department of Geography, University of Durham) with a Perkin-Elmer Elan 6000 mass spectrometer.

Ion chromatography was carried out with a Dionex DX120 liquid chromatographer for analysis of sulphate and chloride concentrations in leather tanning waste solution.

Chapter 5

Protonation and Complex Formation Equilibria with Ligands L^1 – L^4

5 Protonation and Complex Formation Equilibria with Ligands $L^1 - L^4$

5.1 Introduction

Potentiometric titrations were conducted to establish trends in thermodynamic equilibria of sulfonamide ligands designed for binding with late first row transition metals, in particular zinc(II) (see p.21). The protonation equilibria for each ligand were measured individually, then used in part to establish complex formation models. Various experimental parameters such as ionic strength, water protolysis, concentration of reactant, refinement of data, metal hydrolysis equilibria and solvent composition were considered as part of the investigation throughout by using particular equilibrium models as examples.

Initially a major consideration was to find the value of K, the ideal equilibrium constant, which refers to concentrations of species, in relation to the value of Q, the equilibrium quotient measured in activities for a particular ionic strength. The pH electrode was calibrated to account for the difference between proton activity a_{H+} and proton concentration $[H^+]$ to create an accurate model for K. The impact of this adjustment is evaluated in Section 5.2.1.

Titrations with sulfonamide ligands had to be conducted in 80% methanol 20% water because of the differing solubility of both ligand and complex. Protonation and formation constant equilibria as well as acid dissociation of water, K_w, are affected by altered ion solvation in mixed solvents. This effect was accounted for by analysis of the K_w value (Section 5.2.2), and protonation constants for sulfonamide ligands L^1 and L^2 at 10% ethanol,

35% methanol and 80% methanol aqueous solvent mixtures (Section 5.3.1.1 and 5.3.1.2).

Although the equilibrium constant, K, should give a value independent of concentration of reactants (as long as differing ionic strengths are taken into account), the effect of concentration of reactant is important, since hydroxide precipitation of metal ions competes with ligands in solution. Precipitation, therefore, is more dominant at lower pH when concentrations of ligand are reduced. The $[NiL^1_2]$ solution equilibria were compared in Section 5.3.2.2 at 1 and 1 mmol L^{-1}, 1 and 2 mmol L^{-1}, and 5 and 10 mmol L^{-1} [M]/[L] to establish whether significant differences exist in refined formation constant values.

Hydrolysis of metal ions in pH titrations is commonly encountered in the alkaline regions of the pH curve. While it was important to obtain as many data points as possible, it was not necessary to collect data from the entire pH range. The refinement procedure with *Hyperquad2003* software was analysed in Section 5.3.2 with $[CuL^4_2]$, $[ZnL^4_2]$ and $[NiL^4_2]$ data, where the effect of inclusion of more alkaline data points was evaluated.

The equilibrium constants of sulfonamide ligands, L^1 – L^4, have not been previously reported. Values quoted in Section 5.3 were compared with analogous sulfonamidoquinoline ligands discussed in Section 2.2.1. The evaluation procedure was also verified with known protonation constants cited in *SCDbase* Stability Constants Database program[207] with ligands *DL*-tartaric acid, 2,3-pyridinedicarboxylic acid and 2,6-pyridinedicarboxylic acid, which were investigated as suitable ligands for chromium chelation in Chapter 8.

The formation constant data described in Section 5.3.2 and 5.3.3 were related to the previously described structural observations, and give a good indication of selectivity for zinc(II). Species distribution model analysis also

provided useful information on the likely behaviour of reactants at varied concentrations when evaluating ligands for possible metal ion sensor constructs.

5.2 K_w Determinations

Titrations with background solvent were required to account for altered dissociation constants of water K_w when methanol was added for solvation of ligands L^1-L^4 and also for the addition of background electrolyte. Upon addition of 0.1mol L^{-1} tetramethylammonium nitrate (NMe_4NO_3) to pure water, the appropriate log K_w is –14.00 (Section 5.2.2). An 80% MeOH / 20% H_2O solution in the same electrolyte altered the log K_w to about -14.50 as seen in Section 5.2.

Addition of electrolyte causes the recombination of H^+ and OH^- to be hindered by electrostatic interactions and therefore equilibrium shifts away from the 'infinite dilution' ideal.[183] The pH electrode measures H_3O^+ in terms of *activity*. However, mass balance models for equilibrium constant analysis are measured in concentration. Thus, the electrode firstly needed to calibrated to read p[H^+] instead of pH (Section 5.2.1). The limited sensitivity associated with 'alkaline error' of the pH electrode can make absolutely precise determination of K_w difficult, and was assessed with varied concentrations of acid in Section 5.2.3.

5.2.1 pH versus p[H] Scale Calibration

The H^+ concentration scale, p[H] calibrated electrode takes into account the non-ideal behaviour of the high ionic strength solution with the activity coefficient γ relating a_H to [H^+], the p[H] scale calibration is described in Section 4.1.4.

Three titration curves, with data points in the alkaline region, were used to refine the model with p[H] calibration (Figure 5.1). Refinement resulted in a value of log K_w = -14.39 compared with –14.59 for a pa_H calibrated electrode. The refined log K_w value of a 1 mmol L^{-1} acid solution, calibrated to read p[H], was –14.35.

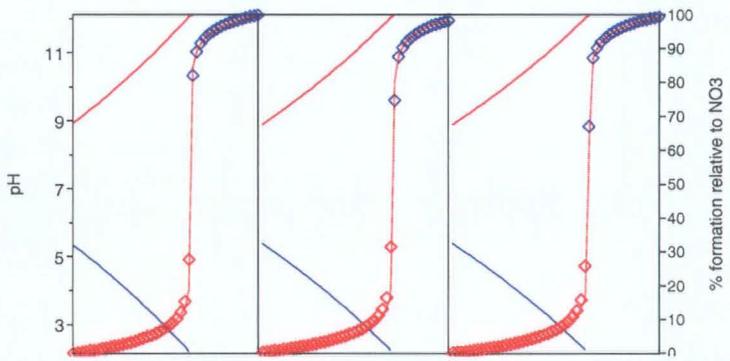

Figure 5.1 Refinement of three data sets in the alkaline region of a strong acid; p[H] calibrated, 10mmol L^{-1} HNO_3. Red squares represent omission of data points in model

5.2.2 Solvent Composition

The solvent composition was adapted as necessary to the solubility requirements of ligand and metal/ligand solutions. The acidity of the 80% MeOH-aqueous solvent was reduced compared with aqueous solution. This is illustrated by titration curve comparison of aqueous and 80% MeOH solutions in Figure 5.2 of the same acid and electrolyte concentration. The log Kw of the aqueous solution was refined to a value of –14.00.

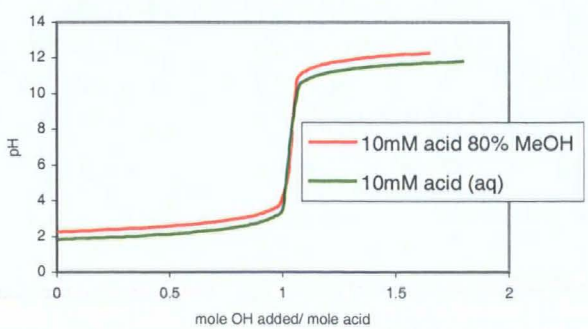

Figure 5.2 10 mmol L^{-1} HNO_3 titration in 80%MeOH / 20% H_2O; 0.1 mol L^{-1} NMe_4NO_3

Previous studies have shown that the pH electrode remains stable in this solvent composition.[208,209] A measured log K_w of 80% MeOH-water gave values of –14.49 ± 0.1, which compares well with -14.42 measured by Mussini *et al* for pure 80% MeOH-water.[208,209] Recently, the autoprotolysis of 80% MeOH-water was also measured, with a combination pH electrode, giving a value of –13.94.[210] The experimental log K_w values measured in this study are listed below in Table 5-1.

Table 5-1 Experimental pK_w values in alcohol-water media

Solvent Composition	Electrolyte	pK_w^*
10% EtOH- 90% Water	NMe_4NO_3	-14.03±0.01
35% MeOH - 65% Water	NMe_4NO_3	-14.35±0.02
80% MeOH - 20% Water	NMe_4NO_3	-14.49±0.1

*pH calibrated

5.2.3 K_w Conclusions

Table 5-2 gives the log K_w values with error estimates from *Hyperquad2003* for titration data showing the effect of solvent composition, calibration method and acid concentration.

Solvent composition of 80% MeOH - water increased the log K_w value from –14.00 to –14.47 ± 0.12. The pH electrode remained stable throughout experiments in this composition. The log K_w varied between –14.59 to –14.39, but once the electrode was calibrated in the p[H] scale, the value was almost constant at –14.37 ± 0.02.

Overall the log K_w has a significant effect on the fitting of an equilibrium model. Differences in Table 5-2 do not necessarily have a large impact on formation constant data, because in many cases data in alkaline regions are excluded due to hydrolysis. The log K_w has a more pronounced effect on

protonation constant values, especially basic protonations that are measured in alkaline media, as seen with ligands L^1 and L^4.

Table 5-2 pK_w values at varied concentration, calibration method and solvent composition

Solvent	Background Electrolyte	$[H^+]$ mmol L^{-1}	Calibration Method	log K_w ±std.dev.	Chi^2	σ
Aqueous	NMe_4NO_3	10	pH	-14.00 ±0.006	17.19	5.92
80% MeOH/ 20% H_2O	NMe_4NO_3	10	pH	-14.59 ±0.003	15.13	4.86
80% MeOH/ 20% H_2O	NMe_4NO_3	10	p[H]	-14.39 ±0.0036	19.73	4.01
80% MeOH/ 20% H_2O	NMe_4NO_3	1	pH	-14.50 ±0.003	3.25	0.67
80% MeOH/ 20% H_2O	NMe_4NO_3	1	p[H]	-14.35 ±0.007	32.05	1.12

5.3 Investigation of Sulfonamide Ligand Equilibria with Transition Metal Ions; Cobalt(II), Nickel(II), Copper(II), Zinc(II) and Cadmium(II)

5.3.1 Protonation Equilibria of L^1 - L^4

Thermodynamic equilibria of pyridylsulfonamide ligands L^1-L^4 in Figure 5.3 were investigated as part of the assessment of their utility as a luminescent zinc probe[59,193] as well as with electrochemical sensor methodology in this study. Protonation constants of ligands were first measured; then followed by their equilibria with various metal ions of interest.

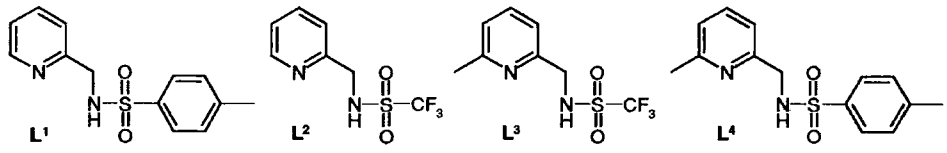

Figure 5.3 Pyridine sulfonamide ligands L^1 – L^4

5.3.1.1 L^1

Ligand L^1 contained a toluene moiety on the sulfonamide group that was known to have a high affinity for zinc(II), as previously discussed in Chapter 2. The sulfonamide nitrogen deprotonates in basic media with a log $K_1 \approx 12$ in the case of L^1. compared with a log $K_1 \approx 7.5$, expected for the trifluoromethylsuflonamide, by analogy to reported sulfonamidoquinoline ligands (Table 2.1).[90]

Ligands L^1 and L^2 were investigated in terms of the most appropriate solvent composition for formation constant equilibrium measurements. In each case it was found that a composition of at least 80% methanol was needed to retain the ML_2 species in solution.

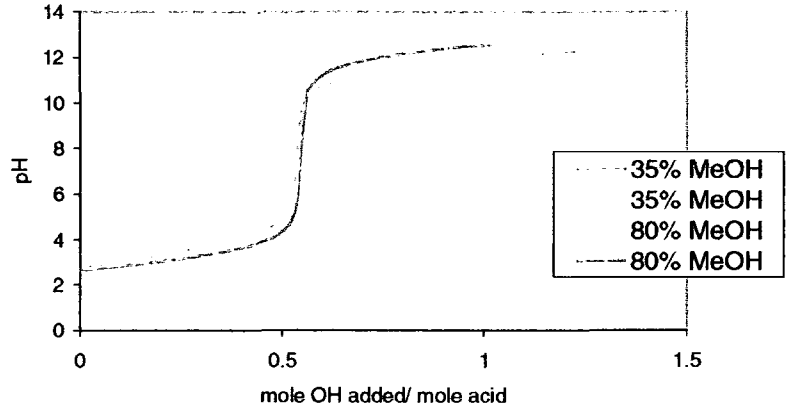

Figure 5.4 The effect of solvent composition on L^1 titration curve data

Preliminary tests with 35% MeOH gave log K_1=11.79 and β_2 15.53 (Table 5-3). The altered polarity of the solvent media is indicated in the above

titration curve (Figure 5.4). The altered K_w of the solvent is noticeable in the alkaline region of the curve. As the proportion of water present in the solvent increases, so does polarity and hydrogen bonding. Therefore, acidity of the ligand is augmented by the presence of water.

Table 5-3 L^1 protonation equilibria at varied solvent composition (±std.dev.)

Ligand	log K_1	β_2	Solvent composition	σ	Chi^2
L^1	11.79±0.012	15.53±0.017	35% MeOH/ 65% H_2O	7.88	22.23
	12.15±0.004	15.42±0.006	80% MeOH/ 20% H_2O	2.53	11.72

The value of log K_1 for ligand L^1, in the standard titration solution of 80% MeOH 0.1 mol L^{-1} NMe_4NO_3, was 12.09, refined using two titration curve data sets simultaneously in *Hyperquad2003*. Error values in

Table 5-5 were cumulative of both data sets. The L^1 protonation data sets for 10mmol L^{-1} 80% MeOH 0.1 mol L^{-1} NMe_4NO_3 were refined to log K_1 =12.15 and β_2 = 15.42.

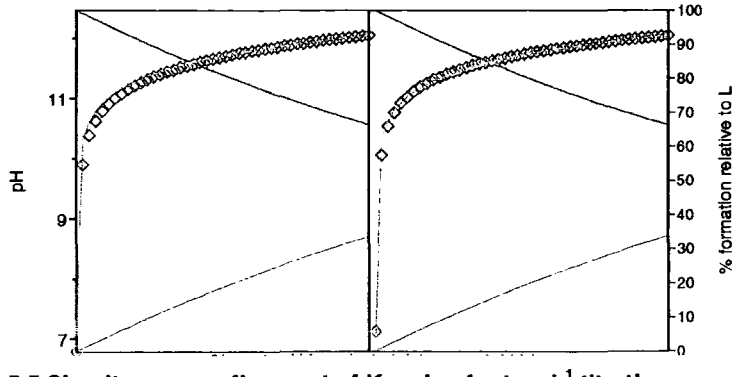

Figure 5.5 Simultaneous refinement of K_1 value for two L^1 titration curves (non-acidified); log K_1 =12.09

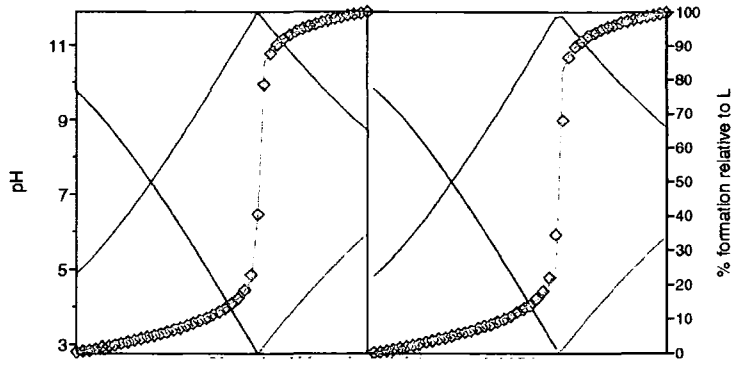

Figure 5.6 Simultaneous refinement of protonation constants for ligand L^1 (acidified solution); log K_1 =12.15 and β_2 =15.42

5.3.1.2 L^2

Ligand L^2 is expected to have a more acidic NH group. This is caused by strong electron-withdrawing effect of the CF_3 substituted sulfonamide group, which stabilizes the conjugate base of the sulfonamide. The corresponding sulfonamidoquinoline ligand CF_3SQ has log K_1 of 7.6.[90]

Initial protonation constants for L^2 were acquired with solutions of 10% EtOH-water and 35% MeOH-water solutions. Low ML_2 solubility in later experiments required the solvent mixture to be 80% MeOH-water; satisfactory in terms of solubility and electrode stability. All titrant solutions were 10mmol L^{-1} L^2 containing 0.1 mol L^{-1} NMe_4NO_3 and were titrated at 25°C. Figure 5.7 illustrates the effect of altered K_w and ligand protonation equilibria on the titration curve due to the solvent composition.

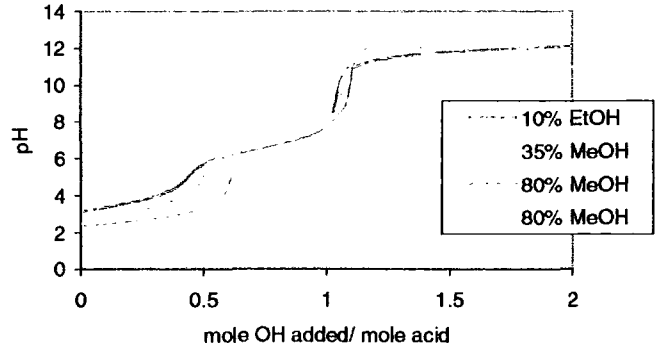

Figure 5.7 L^2 titration curves with altered solvent composition

The constants in Table 5-4 are refined values for protonation equilibria of L^2; the observed increase in basicity of ligand protonations from β_2= 10.00 to 10.17 was attributed to the decrease in polarity of the solvent.

Table 5-4 L^2 protonation equilibria at varied solvent composition (±std.dev.)

Ligand	Log K_1	β_2	Solvent composition	σ	Chi^2
L^2	6.50±0.018	9.60±0.026	10% EtOH, 90% H_2O	10.39	
	6.90±0.012	10.00±0.019	35% MeOH, 65% H_2O	8.45	13.9
	7.50±0.005	10.17±0.016	80% MeOH, 20% H_2O	7.31	7.45

5.3.1.3 L^3

The introduction of the α-methyl substituent at the 6-position of the pyridyl ring in ligands L^3 and L^4 was envisaged to increase the stability of a tetrahedral complex relative to asquare planar on by sterically hindering the formation of a planar complex geometry. Ligand L^3 behaved similarly to the L^2 CF_3 ligand with a similar log K_1 value. The basicity of the pyridyl nitrogen increased due to a less favourable solvation of the conjugate acid $[L^1H]^+$ that is usually associated with steric inhibition of hydration of the positively charged species.

The data for each of the three L^3 titrations were refined to give protonation constants of log K_1 =7.58 and β_2 =10.91. The acidity of the pyridyl nitrogen was decreased with values of log K_2 increasing from 2.69 to 3.33 due in part to the electronic effect of the methyl group.

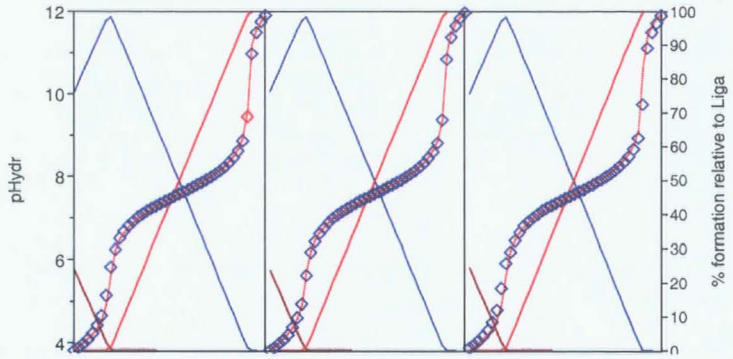

Figure 5.8 Hyperquad refinement of three L^3 titration data sets

5.3.1.4 L^4

The L^4 protonation constants measured, as for L^3, were similar to their non-methyl counterparts. Again the value of K_2 was consistent with a higher proton affinity caused by steric inhibition of hydration of $[L^4H]^+$.

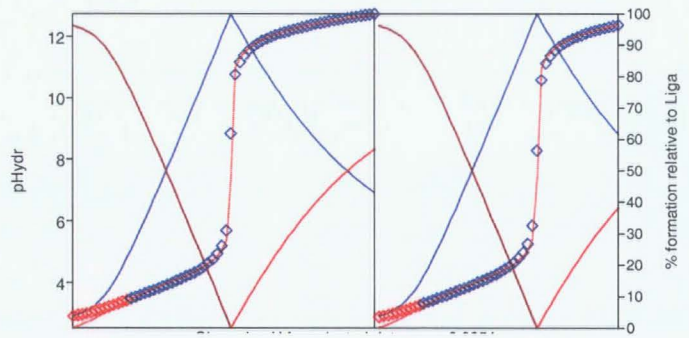

Figure 5.9 Hyperquad refinement of L^4 protonation constants

The two data sets for L^4 protonation equilibria were similar in terms of tosylsulfonamide protonation. Values for log K_1 =12.58 compared to log K_1 =12.21 for L^1, were consistent with a slight increase in basicity. The log K_2 value also showed an increase in basicity from 3.29 to 3.95.

5.3.1.5 Trends in L^1-L^4 Protonation Equilibria

The four sulfonamide ligands investigated have two marked differences in structure. This was exhibited in the protonation curves; experimental data in

Figure 5.10 and an ideal model Figure 5.11, constructed from refined constants, revealing the impact on variation of ligand acidity. The large difference in electronegativity of the sulfonamide CF_3 vs. tosyl is illustrated by electron withdrawing effect, the CF_3 group has, on increasing the acidity of the K_1 reaction. The second is the slight increase in basicity of the pyridyl nitrogen following introduction of the α-methyl group.

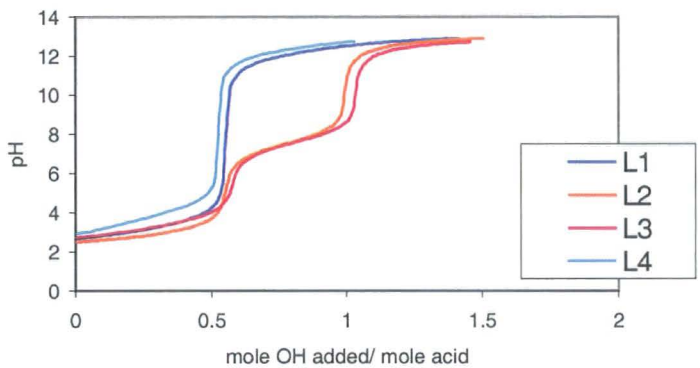

Figure 5.10 Experimental titration curves of ligands $L^1 - L^4$

Table 5-5 Protonation K values for ligands $L^1 - L^4$ 80% MeOH 0.1 mol L^{-1} NMe_4NO_3 pK_w = -14.5 (±std.dev.)

Ligand	Log K_1	Log K_2	β_2	Chi^2	σ
L^1	12.15±0.004	3.27	15.42±0.006	11.72	2.53
L^2	7.50±0.005	2.67	10.17±0.016	8.12	7.52
L^3	7.58±0.002	3.33	10.91±0.008	10.72	10.03
L^4	12.58±0.010	3.95	16.53±0.012	11.63	13.19

In Figure 5.11 the coloured squares indicate where $[H_2L] = [HL]$ and $[HL] = [L]$ respectively, at these points pH = pK_2 and pK_1. For example, the pH at coloured squares on the L^4 curve are ~ 3.9 and ~ 12.5; this agrees with log K_2 and log K_1 data in Table 5-5.

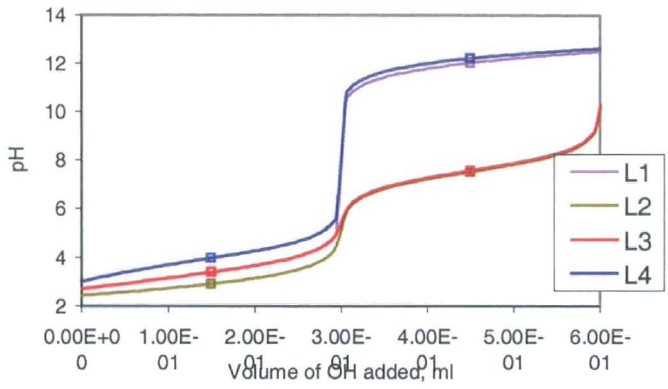

Figure 5.11 Theoretical titration curves of acidified L^1 – L^4 solutions generated in HySS speciation program[211]

Species distribution diagrams modeled from equilibrium data constructed with HySS software[211] illustrates the increased basicity of the L^1 tosylsulfonamide nitrogen compared with the L^2 trifluoromethylsulfonamide nitrogen. This is exemplified by the high concentration of the LH species throughout the pH 6-10 range.

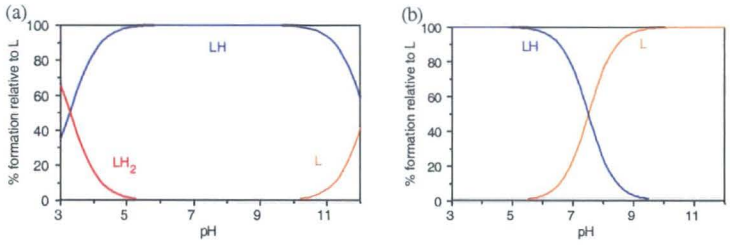

Figure 5.12 Species distribution of ligand deprotonation at 10mmol L^{-1} (a) L^1 and (b) L^2

5.3.2 Toluenesulfonamide Ligands; Formation Constants of L^1 and L^4 Complexes

The formation equilibria of metal complexes formed in the presence of the sulfonamide ligands were calculated using titration data with fixed metal to ligand ratios and varied pH. Experimental protonation constants were included in the refinement of metal / ligand equilibrium constants, and trends in stability of the complexes of the late first row transition metals to the selected ligands were defined. Hydrolysis of metal ions occurred at lower pH

(~7 – 8) when ligands did not compete effectively for metal coordination. In these instances equilibrium constants could only be estimated.

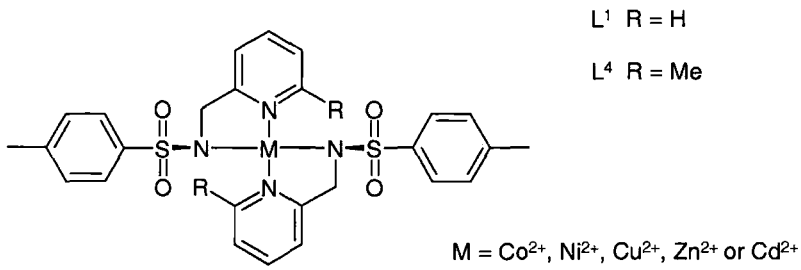

Figure 5.13 Structure of tosylsulfonamide complexes

It was hypothesized that the α-methyl group in L^3 and L^4 would reduce stability of both copper(II) and nickel(II) complexes.

5.3.2.1 [CoL$^1_2$]

Figure 5.14 shows two titration curves obtained for a Co^{2+} and L^1 solution with concentrations of 5 and 10 mmol L^{-1}. The data is plotted as a function of the amount in moles of hydroxide added to the amount of acid in solution. In this way it was convenient to illustrate the inflections of the curve in relation to the neutralization point, where the ratio mole OH^-/ mole H^+ = 1. Unless indicated otherwise, all titrations were conducted at 80% MeOH 0.1 mol L^{-1} NMe_3NO_3 at 25°C.

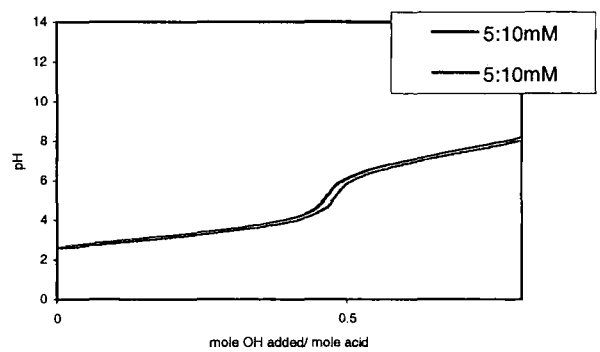

Figure 5.14 Co^{2+}/ L^1 complex formation equilibria titration curves at 5 and 10 mmol L^{-1} (M/L)

The two data sets are refined to β_{ML} =7.96 and β_{ML2} =14.28. The model is refined to a better fit with the inclusion of $[CoL^1H]^+$ species; β_{MLH} =14.73. Data are excluded above pH 8.0 to avoid the presence of hydrolysis in calculation an illustration of the Hyperquad analysis is seen below in Figure 5.15.

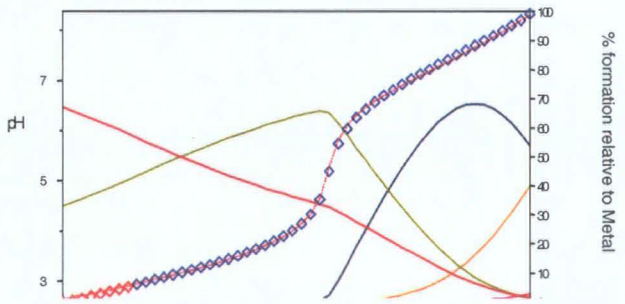

Figure 5.15 Hyperquad analysis of Co^{2+}/ L^1 complex equilibria; -- M, -- MLH, -- ML, -- ML_2, -- $M(OH)_2$

5.3.2.2 $[NiL^1{}_2]$

Formation equilibria were investigated with Ni^{2+} / L^1 complexation at different concentration and M/L ratios. The results show very similar outcomes at 1 and 2 mmol L^{-1}, and 5 and 10 mmol L^{-1}, as well as for the β_{ML} refinement at 1 and 1 mmol L^{-1} (M/L). Resultant titration curves are shown below along with tabulated β value and error estimates.

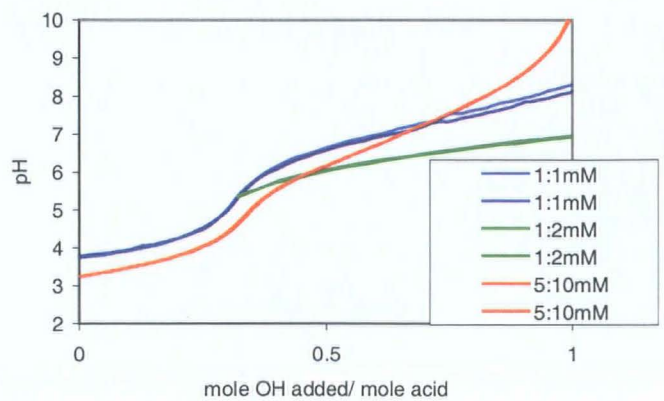

Figure 5.16 Ni^{2+} / L^1 titration curves non-acidified at 1 and 1, 1 and 2, and 5 and 10 mmol L^{-1} (M/L)

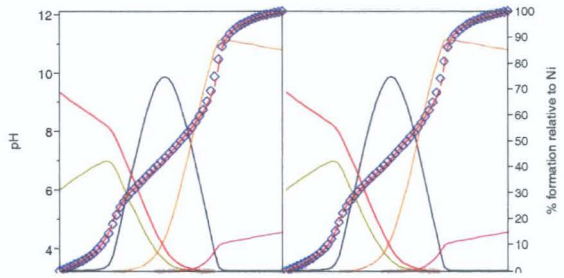

Figure 5.17 Refinement of Ni^{2+}/ L^1 equilibria at 5 and 10 mmol L^{-1} (M/L); -- M, -- MLH, -- ML, -- ML_2, -- $M(OH)_2$

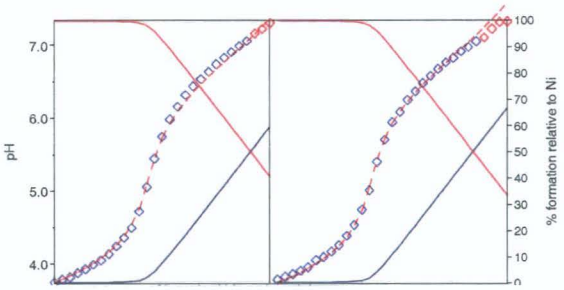

Figure 5.18 Refinement of Ni^{2+}/ L^1 equilibria at 1 and 1 mmol L^{-1} (M/L); -- M, -- ML

At 1 and 1 mmol L^{-1} (M/L) precipitation occurred early ~ pH 7.5 (Figure 5.17) and did not yield data except for the beginning of the ML curve. The 1 and 2 mmol L^{-1}, and 5 and 10 mmol L^{-1} (M/L) titrations yielded very similar β values, and in both instances required the postulation of an MLH species for adequate refinement of error values.

Table 5-6 Ni^{2+}/ L^1 titration β values and error estimates (±std.dev.)

mmol Ni	mmol L^1	β_{ML}	β_{MLH}	β_{ML2}	Chi^2	σ
1	1	8.28±0.013			9.39	0.48
1	2	8.28±0.013	14.21±0.084	15.50±0.022	29.05	1.33
5	10	**8.50±0.012**	**14.29±0.015**	**15.28±0.019**	10.67	2.06

The species distribution diagrams in Figure 5.19 shows models the concentrations in the above table. It indicates, with $[NiL^1_2]$, the diminishing ability to measure ML_2 species at lower concentration before hydrolysis

competes. The 5 and 10 mmol L^{-1} (M/L) titration values are therefore the most reliable.

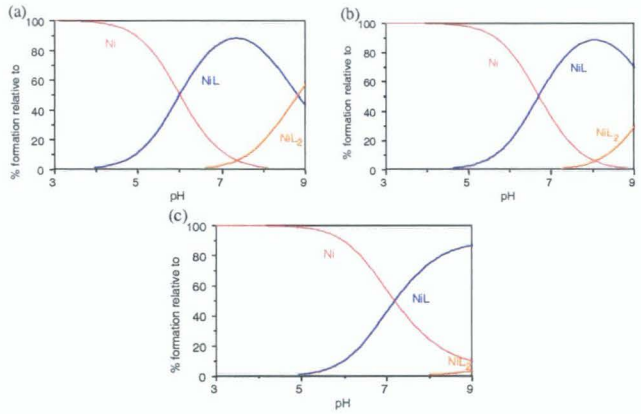

Figure 5.19 Species distribution of Ni^{2+}/ L^1 solution equilibria with decreasing concentration of L^1 (a) 5 and 10 mmol L^{-1} (b) 1 and 2 mmol L^{-1} and (c) 1 and 1 mmol L^{-1} (M/L)

5.3.2.3 [CuL^1_2]

The [CuL^1_2] complex was a well-behaved system with good complex stability and reversible redox behaviour. Additionally, [CuL^1_2] observable absorbance changes with pH and also between square planar and distorted tetrahedral [CuL^4_2] (UV/Vis absorbance is discussed in Chapter 6). The [CuL^1_2] complex is expected to have the highest stability of the metals studied because of Irving-Williams order and ability of [CuL^1_2] to form a square planar complex.

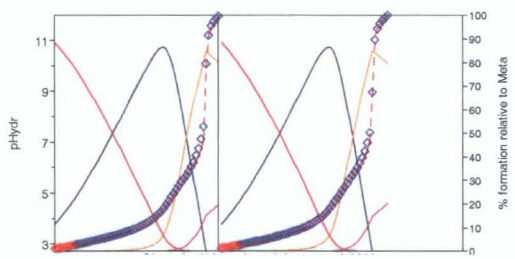

Figure 5.20 Hyperquad refinement of Cu^{2+}/ L^1 equilibria at 5:10mmol L^{-1}; -- M, - - ML, -- ML_2, -- $M(OH)_2$

A 5 and 10 mmol L^{-1} (M/L) solution of Cu^{2+}/ L^1 had refined formation constants of β_{ML} = 11.35 and β_{ML_2} = 20.50. The β_{ML} value was first refined with data in the ML region then the β_2 was added during refinement. The colour of solution quickly turned from blue to green increasing in intensity as the titration progressed. No precipitation was noted at higher pH. However, over period of a few hours, a dark green crystalline formed, consistent with formation of ML_2 as an insoluble solid.

5.3.2.4 [ZnL^1_2]

In the absence of the methyl group that disrupts copper(II) geometry, the stability of [ZnL^1_2] was expected to be lower than copper(II).

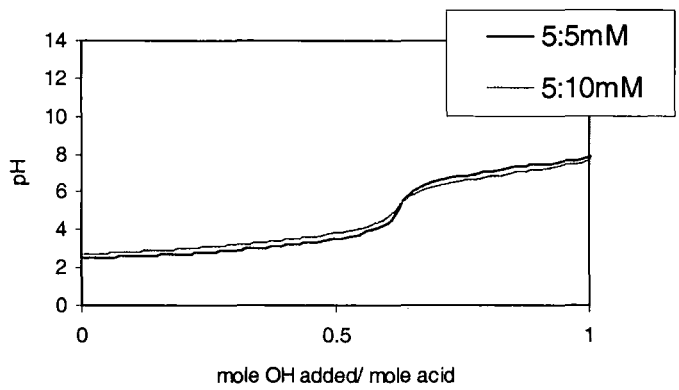

Figure 5.21 Titration curves having 1:1, and 1:2 ratios of Zn^{2+} / L^1 solutions at [L] = 10 mmol L^{-1}

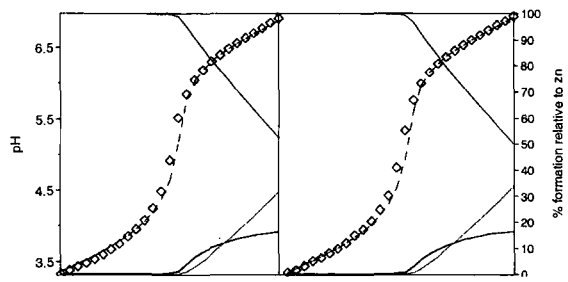

Figure 5.22 Hyperquad refinement of 5 and 10mmol L^{-1} solution Zn^{2+} / L^1 titration curves; -- M, -- ML, -- ML_2

Refinement of the 5 and 10mmol L^{-1} (M/L) solution (Figure 5.22) gave values of β_{ML} = 7.12 and β_{ML_2} = 15.03. The overall stability is higher than

that of cobalt(II) (β_{ML_2} = 14.28) and just slightly lower than nickel. Precipitation occurred early in the titration of 5 and 5 mmol L^{-1} (M/L), solution refinement was unsuccessful; the two curves are seen in Figure 5.21.

5.3.2.5 [CdL^1_2]

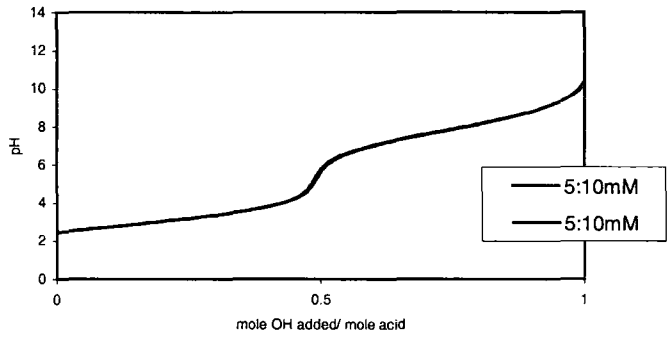

Figure 5.23 Titration curves of Cd^{2+} / L^1 solution at 5 and 10 mmol L^{-1} concentration

Precipitation occurred above pH 8.0. However, the inflections observed in Figure 5.23 at 0.5 and 1.0 OH^-/H^+ were stable and reproducible. Analysis of two equilibrium scenarios shows one where hydrolytic product [$Cd(OH)_2$] was included, and another that excluded all data points above pH 8.0, the resultant formation constants are seen below.

Table 5-7 Cd^{2+}/ L^1 titration K values and error estimates (±std.dev.)

Cd^{2+}/ L^1 ratio	pH range	β_{ML}	β_{ML2}	β_{MLH}	$\beta_{M(OH)2}$	Chi^2	σ
5:10	**2.5-8.0**	**7.81±0.021**	**14.01±0.024**	**14.81±0.021**		29.45	10.91
5:10	2.5-12.0	7.61±0.033	13.96±0.033	14.66±0.039	-17.25±0.095	8.69	19.79

The β values are similar, although the pH 2.5-8.0 data is the only reliable result. The β_{MLH} was needed to fit the model, without an MLH species the error is much greater with σ =57.69.

5.3.2.6 [CuL$^4_2$]

The complex formed between copper and ligand L^4 is sterically inhibited from adopting a square planar geometry. Instead, it is forced into a distorted tetrahedral structure that was expected to be less stable than the previous L^1 complex. The altered *d*-shell transitions were noted by colour change from green L^1 complex to orange L^4 complex. This is explored with further spectroscopic measurements in Chapter 6.

The Cu^{2+}/ L^4 titrations were also used to analyse the effect of varied pH ranges of data points to be included in the refinement procedure. Ranges included pH 4.6 - 5.0, 4.6 -6.7 and 4.6 -12.2, illustrated in Figure 5.24 to Figure 5.26. The formation constant values are summarised in Table 5-8.

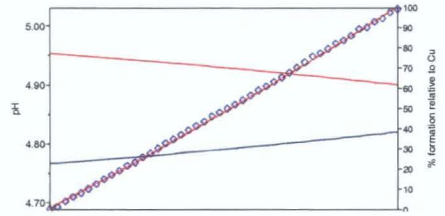

Figure 5.24 Refinement of 5 and 10 mmol L^{-1} Cu^{2+}/ L^4 solution in lower pH region depicting ML species formation only; -- M, -- ML

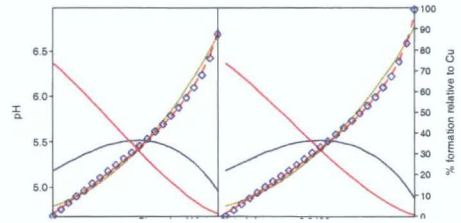

Figure 5.25 Refinement of 5 and 10 mmol L^{-1} Cu^{2+}/ L^4 solution at mid-pH range depicting ML and ML_2 species; -- M, -- ML, -- ML_2

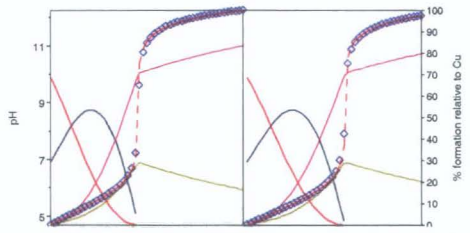

Figure 5.26 Refinement of Cu^{2+}/ L^4 5 and 10 mmol L^{-1} solution with entire pH range including estimated hydrolysis constants; -- M, -- ML, -- ML_2, -- $M(OH)_2$

The titration data for the three models show a high confidence in β value refinements, as seen from the *Hyperquad* graphs above, and in results Table 5-8. The β_{ML} values were similar (9.43-9.63), especially the first two pH ranges that excluded the alkaline region.

The β_{ML_2} value was similar, however, a variation was incurred when the speciation was fundamentally altered with the inclusion of the $M(OH)_2$ species. The difference in models is clearly visible (Figure 5.26). Although the Chi^2 and σ values were acceptable for the full pH range data, the lower pH data was more reliable.

Table 5-8 Cu^{2+}/ L^4 β values at different pH ranges, accepted values highlighted. *Same titration (±std.dev.)

M/L ratio	pH range	β_{ML}	β_{ML_2}	$\beta_{M(OH)_2}$	Chi^2	σ
5:10 mM	4.6 - 5.0	9.45±0.010				0.36
5:10 mM *	4.6 - 6.7	**9.43±0.011**	**18.75±0.011**			1.79
5:10 mM *	4.6 - 12.2	9.63±0.007	18.00±0.015	-11.02±0.029	7.49	1.86

The decreased ligand field stabilization contribution was exhibited by the lowered β_{ML} and β_{ML_2} values 9.43 and 18.75, respectively, compared to L^1 values of 11.35 and 20.50 for K_{ML} and β_{ML_2}.

5.3.2.7 $[ZnL^4_2]$

The refinement procedure at different pH ranges was also exemplified with Zn^{2+}/ L^4 equilibria, ranges from pH 5.3 – 6.5, 5.3 – 8.0, and 5.3 – 12.1, illustrated below in Figure 5.27 to Figure 5.29. The pH 5.3 – 6.5 range refined both ML and ML_2 species, while excluding any hydrolysis reaction in the model. The latter two pH ranges required $M(OH)_2$ species for refinement.

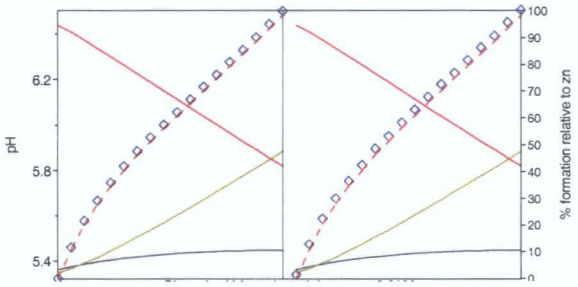

Figure 5.27 Refinement of Zn^{2+}/ L^4 titration inclusion of ML (blue curve) and ML_2 (green curve) species formation; -- M, -- ML, -- ML_2

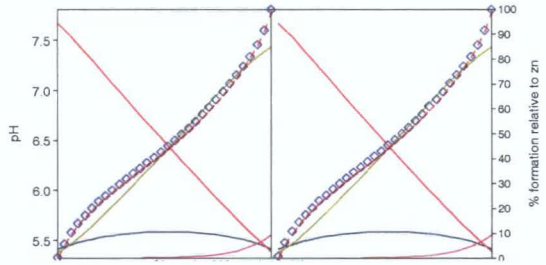

Figure 5.28 Refinement of Zn^{2+}/ L^4 titration in mid-pH range with inclusion of low level of $M(OH)_2$ species; -- M, -- ML, -- ML_2, -- $M(OH)_2$

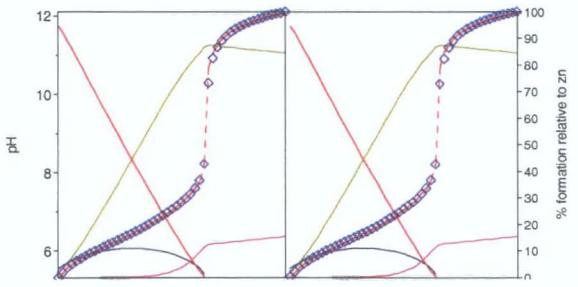

Figure 5.29 Refinement of Zn^{2+}/ L^4 equilibria at 5 and 10 mmol L^{-1} over the entire pH range; -- M, -- ML, -- ML_2, -- $M(OH)_2$

Refinement of Zn^{2+}/ L^4 data at different ranges seen in Table 5-9, show very little variation; β_{ML} =7.83 ±0.03, β_{ML_2} =16.83 ±0.01, and $\beta_{M(OH)_2}$ = -14.96

±0.03. However, the inclusion of hydrolysis constants added complexity to the model because new species are likely form over time and thus alter the model. Therefore, the data only in the low pH range was judged to be reliable.

Table 5-9 Zn^{2+}/ L^4 β values at different pH ranges, accepted values highlighted (±std.dev.)

Zn^{2+}/ L^4 ratio	pH range	β_{ML}	β_{ML2}	$K_{M(OH)2}$	Chi^2	σ
5:10 mM	5.3 – 6.5	**7.80±0.017**	**16.84±0.0024**			0.68
5:10 mM	5.3 – 8.0	7.86±0.015	16.83±0.0024	-14.93±0.023	3.50	0.77
5:10 mM	5.3 – 12.1	7.81±0.035	16.83±0.005	-14.99±0.036	18.94	1.92

Although hydrolysis occured early, it was much weaker than in the L^1 equilibria, as indicated in Figure 5.28 and Figure 5.29 curves above. The overall stability of the complex was enhanced relative to the L^1 complex (β_{ML2} =15.03), and also approached the stability of the inhibited tetrahedral $[CuL^4_2]$, β_{ML2} =18.75.

5.3.2.8 $[NiL^4_2]$

The speciation of nickel(II) depicted in the *Hyperquad* graphs below indicates that the hydrolysis product, $M(OH)_2$, was formed near the beginning of the titration, while a small amount of ML_2 species was also formed. This was confirmed by observation made during titration. A buffering effect occurred, i.e., where the metal ion reacted with hydroxide as it was added. This stoped the pH from increasing appreciably. Hydrolysis followed at pH 7-8 (Figure 5.32) with increased cloudiness. Only in the lowest pH range 6.28 – 7.5, seen in Figure 5.30, was the hydrolysis product

excluded from the model. This was still not a reliable result because of lack of data points, and the fact that such a small amount of ML_2 species (green curve) is present in the model (<15%).

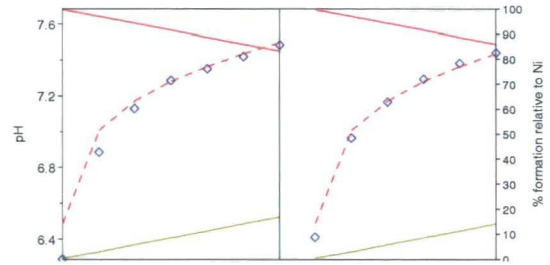

Figure 5.30 Refinement of Ni^{2+}/ L^4 equilibria without hydrolysis constant at low pH range; -- M, -- ML_2

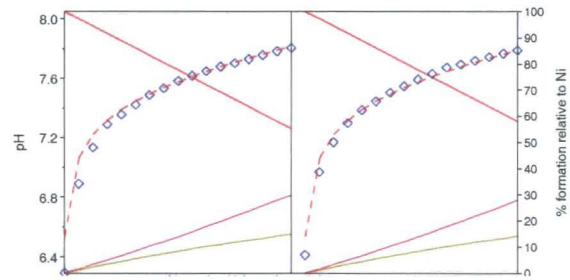

Figure 5.31 Refinement of Ni^{2+}/ L^4 titration at mid-pH range inclusive of hydrolysis constants; -- M, -- ML_2, -- $M(OH)_2$

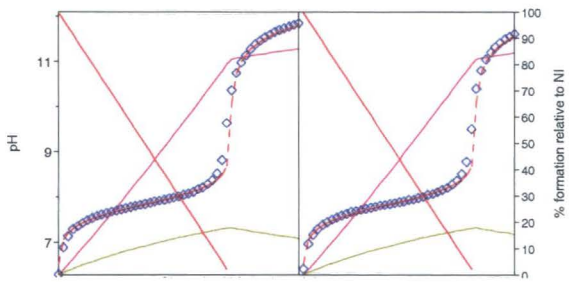

Figure 5.32 Refinement of Ni^{2+}/ L^4 titration with $M(OH)_2$ formation (pink curve) present below pH 7.0; -- M, -- ML_2, -- $M(OH)_2$

Table 5-10 Ni^{2+}/ L^4 β values at different pH ranges

M/L ratio	pH range	β_{ML}	β_{ML2}	$\beta_{M(OH)2}$	Chi^2	σ
5:10mM	6.3 – 7.5	-	13.58±0.097			2.00
5:10mM	6.3 – 7.8	-	**13.08±0.11**	**-15.9±0.048**		2.76
5:10mM	6.3 – 11.8	-	12.90±0.106	-15.8±0.0246	8.82	4.76

Although the model was refined to a low error, no reliable β value was obtained from this data because of competitive hydrolysis. However the mid-pH range gave a good estimate of the ML_2 equilibrium. Refinement of β_{ML_2} was 13.08. At this range the ML_2 formation was at its highest percentage relative to $M(OH)_2$ species.

$[NiL^1{}_2]$ forms a square planar complex but in the case of L^4 it was inhibited by the α-methyl substituent, and therefore has to adopt distorted tetrahedral structure. The stability of this arrangement is reduced indicated by the decreased β_{ML_2} from 15.28 to 13.08.

5.3.2.9 Trends L^1 and L^4 Complex Equilibria

The β_{ML_2} of the four first row transition metals followed the Irving-Williams order $Mn^{2+} < Fe^{2+} < Co^{2+} < Ni^{2+} < Cu^{2+} > Zn^{2+}$. Cobalt(II) and zinc(II) invariably formed distorted tetrahedral complexes, while with L^1 copper(II) and nickel(II) were able to form square planar complexes allowing for greater ligand field stabilization. The order of stability indicated empirically in Figure 5.33 in the buffered region of the curve, between 0.5 and 1.0, where the lower the curve the higher the stability.

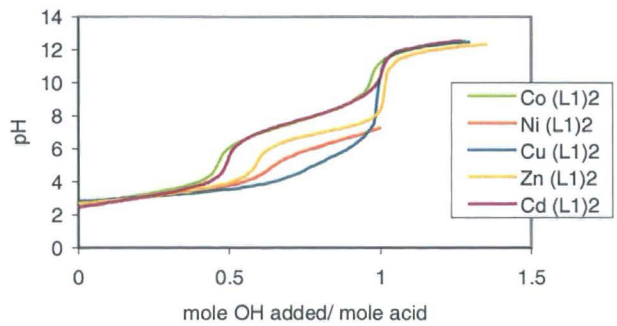

Figure 5.33 Comparison of L^1 complex formation equilibrium titration curves

Zinc complexes appeared to exhibit positive cooperativity, not observed with other metals. All β_{ML} values were higher than β_{ML_2} values, except for zinc(II) complexes $[ZnL^1{}_2]$, $[ZnL^3{}_2]$, and $[ZnL^4{}_2]$ (Table 5-11).

Table 5-11 Comparison of metal formation equilibria with L^1 (±std.dev.)

M^{2+}	β_{ML}	K_{ML2}	β_{ML2}
Co	7.96 ±0.025	6.32	14.28 ±0.0247
Ni	8.50 ±0.012	6.78	15.28 ±0.019
Cu	11.35 ±0.011	9.15	20.50 ±0.014
Zn	7.12 ±0.087	7.91	15.03 ±0.023
Cd	7.81 ±0.021	6.2	14.01 ±0.024

The complexation of nickel(II) and copper(II) was altered with L^4 because of the presence of the α-methyl group. This was confirmed with crystal structure data, and formation constant measurements (Table 5-12). The zinc(II) complex was enhanced in part due to the slight increase in basicity of the ligand. Titration curves are illustrated in Figure 5.34.

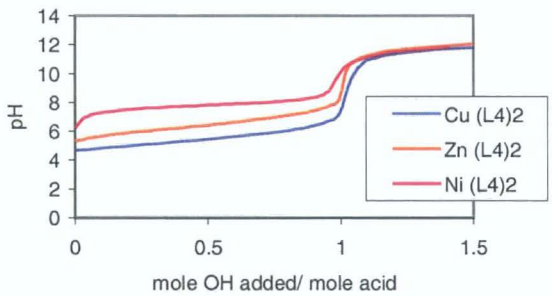

Figure 5.34 Comparison of L^4 complex formation equilibrium titrations curves

Table 5-12 M^{2+} complex formation equilibria with ligand L^4

M^{2+}	β_{ML}	K_{ML2}	β_{ML2}
Ni			13.08 ±0.11
Cu	9.43 ±0.011	9.32	18.75 ±0.011
Zn	7.80 ±0.015	9.04	16.84 ±0.0024

Figure 5.35 was constructed with formation constant data in HySS. The models indicate behaviour of metal ions with changing concentrations of reactants. They indicate that as long as there is adequate level of ligand present in solution the level of complexation is relatively unperturbed even

at $[M_T] = 10^{-6}$ mol L^{-1}. However, Figure 5.35 indicates that the ligand concentration has a pronounced effect on metal speciation, hydrolysis begins earlier as the ligand concentration is decreased.

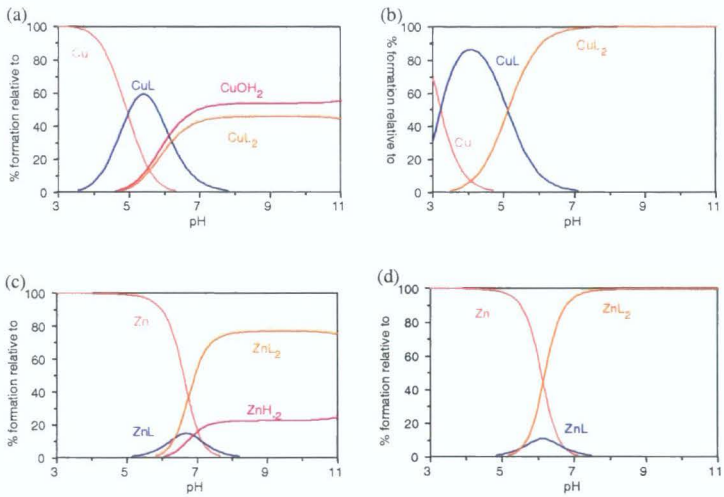

Figure 5.35 Species distribution diagrams of (a) $[CuL^4_2]$, (b) $[CuL^1_2]$, (c) $[ZnL^1_2]$ and (d) $[ZnL^4_2]$ at $[M_T] = 0.001$ mmol L^{-1} and $[L_T] = 10$ mmol L^{-1}

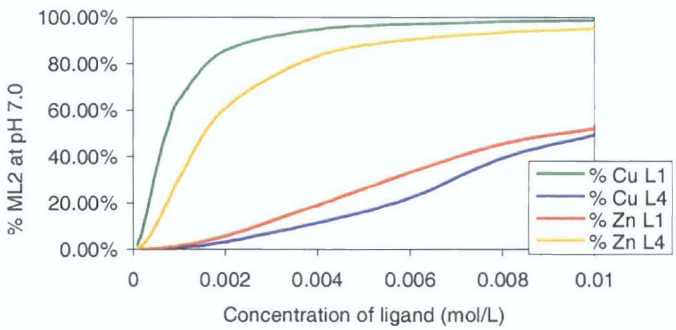

Figure 5.36 Percentage 0.001 mmol L^{-1} metal ion as ML_2 species at pH 7.0 related to concentration of ligand 0.1 – 10 mmol L^{-1}

Figure 5.36 indicates $[CuL^1_2]$ dominant speciation until a sharp decrease below 0.1 mmol L^{-1}, and $[CuL^4_2]$ declines sharply as $[L_T]$ decreases. The reverse was true for zinc complexes. $[ZnL^1_2]$ does not dominate at any ligand concentration, while $[ZnL^4_2]$ shows a marked increase in ML_2 formation at lower ligand concentrations.

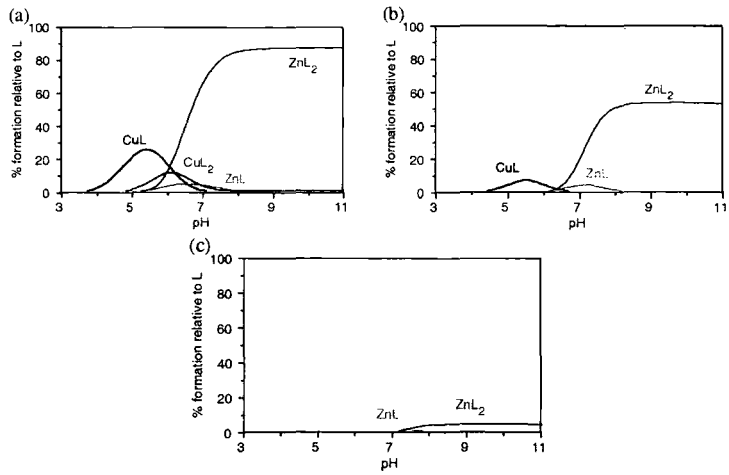

Figure 5.37 L^4 species distribution of competing metal ions Cu^{2+} and Zn^{2+} at (a) 5 and 10 mmol L^{-1} (b) 0.5 and 1 mmol L^{-1}, and (c) 0.05 and 0.1 mmol L^{-1} (M/L)

Direct competition between Cu^{2+}, Zn^{2+} and L^4 was modeled in Figure 5.37 with a 1:2 M/L ratio and decreasing concentrations. Zn^{2+} complexation dominated over Cu^{2+} in the alkaline region of the curve. However, the percentage of L^4 bound to the metal ions decreases sharply as $[L_T]$ decreases below 0.1 mmol L^{-1}.

5.3.3 Trifluoromethylsulfonamide Ligands; Formation Constants of L^2 and L^3 Complexes

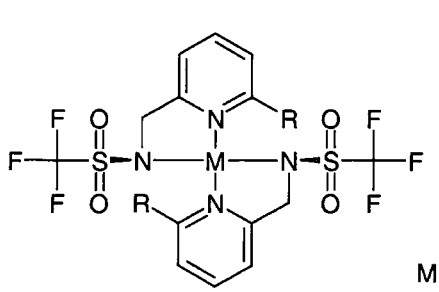

L^2 R = H

L^3 R = Me

M = Co^{2+}, Cu^{2+}, Zn^{2+} or Cd^{2+}

Figure 5.38 Structure of trifluoromethylsulfonamide complex

The CF_3 ligand is more polarizing, leading to harder Lewis base character than the tosyl ligands. Therefore L^2 and L^3 bind less well with borderline Lewis acids such as zinc(II), cobalt(II) and copper(II). Additionally stability

is also affected by structural considerations already known. Nickel(II) forms an octahedral complex and the remaining cations Co^{2+}, Cu^{2+} and Zn^{2+} form a distorted tetrahedral structure. Therefore, $[CuL^2_2]$ is expected to be much lower in stability than $[CuL^1_2]$.

5.3.3.1 $[CuL^2_2]$

Refinement of the Cu^{2+}/ L^2 titration required introduction of an added species MLOH (β_{MLOH} = -0.34) for improved fit of the model in Figure 5.39 (indicated with the green curve in the latter part of the pH range). The stability of the $[CuL^2_2]$ complex is reduced to β_{ML} =6.81 and β_{ML_2} =13.28 compared with L^1 complex β_{ML_2} =20.50.

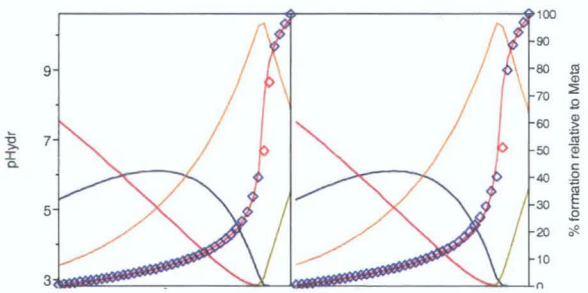

Figure 5.39 Refinement of Cu^{2+}/ L^2 equilibria at 5:10mmol L^{-1}; -- M, -- ML, -- ML_2, -- MLOH

5.3.3.2 $[ZnL^2_2]$

The model for Zn^{2+}/ L^2 titration is refined with ML and ML_2 species gave a β_{ML} = 5.11 and β_{ML_2} =10.21 in the lower pH range before hydrolysis began (Figure 5.40). The dominant species at pH 7.0 appeared to be the ML_2 species. Although, above this pH, metal ion hydrolysis also competes.

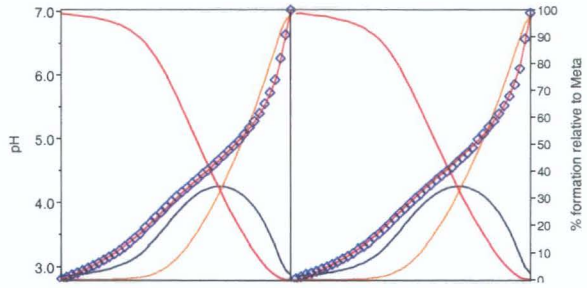

Figure 5.40 Refinement of 5 and 10 mmol L^{-1} Zn^{2+}/ L^2 at pH < 7.0; -- M, -- ML, -- ML_2

The more acidic K_1 of ligand L^2 relative to L^1 lead to increased dominance of ML_2 species at lower pH. This was apparent in the speciation diagrams (Figure 5.41) at a relatively high concentration of L^2, 1mmol L^{-1}.

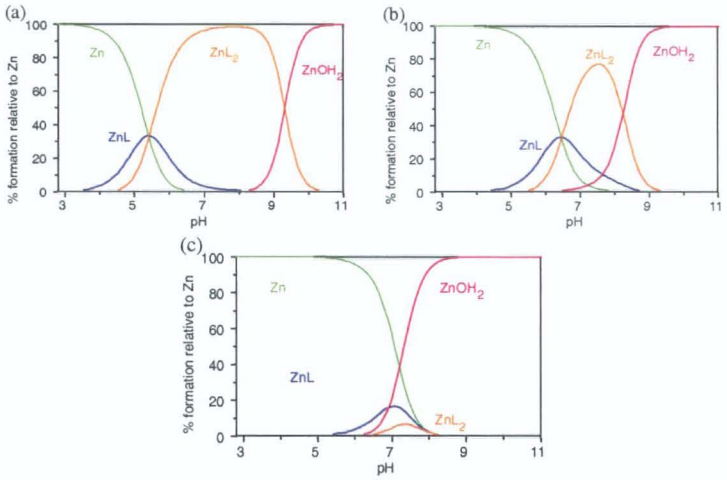

Figure 5.41 Species distribution diagram of varied concentrations of L^2; at (a) 1 mmol L^{-1} (b) 0.1mmo L^{-1} and (c) 0.01 mmol L^{-1}; when $[Zn^{2+}]$ = 0.001 mmol L^{-1}

5.3.3.3 [CoL$^2_2$]

The Co^{2+}/ L^2 equilibria were refined to a best fit with the inclusion of an MLOH species. The harder Lewis base CF_3 ligand is again exemplified in terms of the stability of species formed. Values of 5.39 and 10.18, respectively, for log K_{ML} and β_{ML_2} were calculated in comparison to the analogue of [CoL^1_2] which gave values of 7.99 and 14.32, for the respective formation constants.

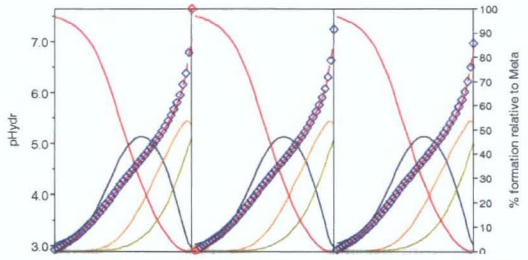

Figure 5.42 Refinement of 5 and 10 mmol L^{-1} Co^{2+}/ L^2 titration at pH < 7.0; -- M, -- ML, -- ML_2, -- MLOH

5.3.3.4 [CdL^2_2]

Figure 5.43 shows Cd^{2+}/ L^2 equilibria was refined with the inclusion of MLOH species represented in the latter part of the curve, ~5%. The model gives values of β_{ML} = 4.74 and β_{ML_2} = 9.97, again much lower than for the analogous tosyl ligand, where β_{ML_2} = 14.01.

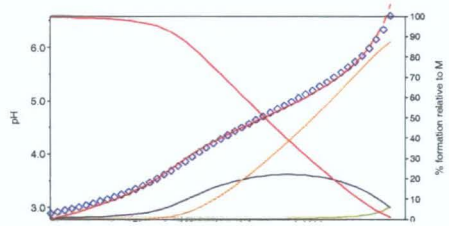

Figure 5.43 Refinement of 5 and 10 mmol L^{-1} Cd^{2+}/ L^2 solution equilibria at pH < 7.0; -- M, -- ML, -- ML_2, -- $M(OH)_2$

5.3.3.5 [CuL^3_2]

The L^3 complexes have α-methyl groups that inhibit formation of square planar or octahedral geometry. The results for L^2 show that the more polarized donor atom sulfonamide nitrogen invariably reduced the stability of the ML_2 complex. The effect of the methyl group could also reduce further the stability of the copper complex.

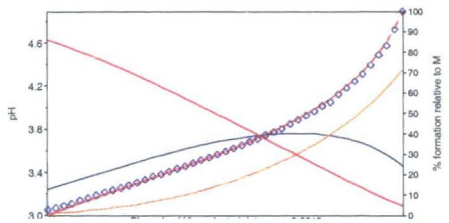

Figure 5.44 Refinement of Cu^{2+}/ L^3 in lower pH region showing ML and ML_2 species; -- M, -- ML, -- ML_2

Refinement of Cu^{2+}/ L^3 titration showed a reduction from the stability of the L^2 complex from β_{ML2} = 13.28 to β_{ML} = 6.23, and β_{ML2} = 12.46. Data above pH 7.0 was discarded because of precipitation of a yellow ML_2 complex and $M(OH)_2$ formation.

5.3.3.6 [ZnL^3_2]

A model for ML and ML_2 species was refined in the lower pH region below pH 6.0 to exclude any precipitate formation. It was noted that a precipitate formed in neutral pH and was thought to be an $ML_n(OH)_m$ species. A solvent composition of 90% MeOH did not alter this outcome. The [ZnL^3_2] complex behaved similarly to [ZnL^4_2] whereby stability was increased slightly from L^1 and L^2 ligands, refined values are β_{ML} = 5.62 and β_{ML2} = 11.50 compared with L^2 values of 5.11 and 10.21 respectively.

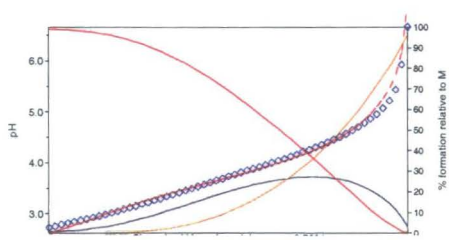

Figure 5.45 Refinement of 5 and 10 mmol L^{-1} Zn^{2+}/ L^3 at pH 2.8 - 6.8 concentration; -- M, -- ML, -- ML_2

5.3.3.7 Trends L^2 and L^3 Complex Equilibria

Equilibrium values follow the Irving-Williams order with copper(II) the most stable complex. However, the stability values were invariably lower

than those seen with the tolylsulfonamide ligands, with formation constants of $\beta_{ML_2} \approx 15$ reduced to $\beta_{ML_2} \approx 10$. The CF_3 ligand is a harder Lewis base nitrogen donor, and a lesser stability for the borderline Lewis acids. Complex formation data is therefore less extensive because of hydrolysis problems. A pH drift occurred extensively, seen in the latter part of the titration curves for Co^{2+}, Zn^{2+} and Cd^{2+} (Figure 5.46), which extended past the neutralization point (denoted mole OH added/ mole acid =1) indicating hydroxide reaction with metal ions. In some cases an MLOH species was included as part of the model for best fit, e.g. for $[CuL^2OH]$, $[CoL^2OH]$ and $[CdL^2OH]$.

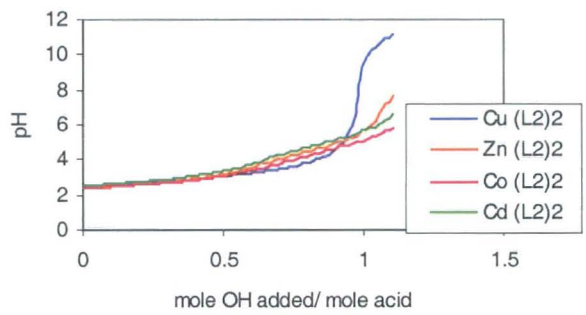

Figure 5.46 Titration curves of M^{2+}/ L^2 solution equilibria

Table 5-13 L^2 and L^3 complex formation equilibria values (±std.dev.)

Ligand	M^{2+}	β_{ML}	K_{ML2}	β_{ML2}	Chi^2	σ
L^2	Co	5.39 ±0.024	4.79	10.18 ±0.023	27.85	7.27
	Cu	6.81 ±0.015	6.47	13.28 ±0.018	28.9	8.85
	Zn	5.11 ±0.033	5.1	10.21±0.023	11.07	4.45
	Cd	4.74 ±0.012	5.23	9.97 ±0.039	13.36	12.09
L^3	Cu	6.23 ±0.008	6.23	12.46 ±0.013	-	1.78
	Zn	5.62 ±0.074	5.88	11.50 ±0.050	9.75	11.18

In regard to the effect of the α-methyl group, the L^2 and L^3 complex equilibria show similar relationship to that between the L^1 and L^4 complexes. The stability of $[CuL^3_2]$ decreased and the stability of $[ZnL^3_2]$ increased (Table 5-13). The reduced stability of the copper complex was of interest

since the structural data of $[CuL^2_2]$ showed that it adopts the same structure as $[CuL^3_2]$. Figure 5.47 and Figure 5.48 compare L^2 and L^3 complex formation curves for copper(II) and zinc(II) solutions. The decreased stability of $[CuL_3]$ is indicated, visually, by a more alkaline titration curve; the opposite is true for $[ZnL_3]$.

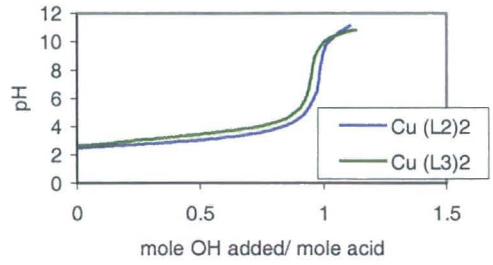

Figure 5.47 α-methyl on L^3 ligand reduces stability of $[CuL^3_2]$

The stability of $[ZnL^3_2]$ and $[ZnL^4_2]$ increases with respect to the L^1 and L^2 complexes. This may be associated with enhanced basicity of the pyridyl nitrogen. Data analysis was not successful for $[CoL^3_2]$ and $[CoL^4_2]$ which could have confirmed this supposition.

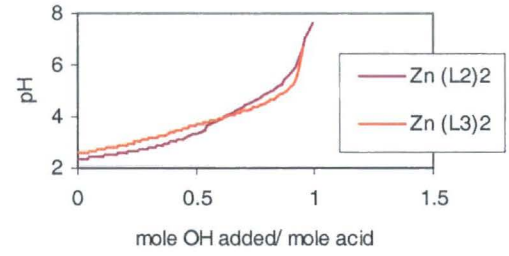

Figure 5.48 α-methyl effect on $[ZnL^3_2]$ increases stability

The species distribution diagrams in Figure 5.49 illustrate the decreased stability of $[CuL^3_2]$ compared to $[CuL^2_2]$. While an increased presence of the $[ZnL^3_2]$ species, is observed, relative to the $[ZnL^2_2]$ model.

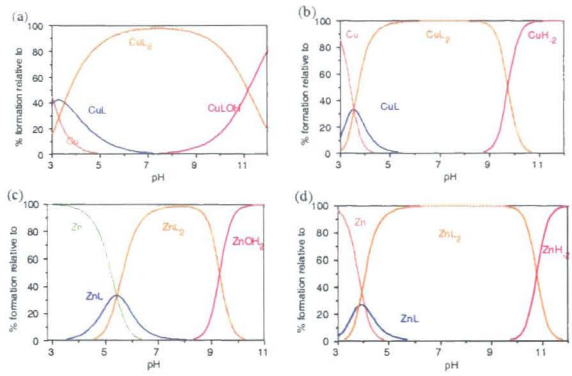

Figure 5.49 Species distribution diagrams of (a) $[CuL^2_2]$, (b) $[CuL^3_2]$, (c) $[ZnL^2_2]$ and (d) $[ZnL^3_2]$; $[M_T]$ = 0.001mmol L^{-1} and $[L_T]$ = 10mmol L^{-1}

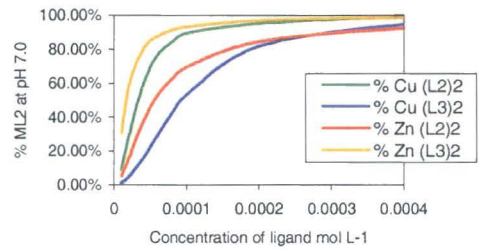

Figure 5.50 Percentage 0.001 mmol L^{-1} metal ion as ML_2 species at pH 7.0 related to concentration of ligand L^2 and L^3 0.01 mmol L^{-1} – 1mmol L^{-1}

Figure 5.50 shows that despite the lower thermodynamic stability of L^2 and L^3 complexes, the reduced ligand basicity allows ML_2 species to remain the dominant metal species in solution at a much lower concentration than with L^1 and L^4. The effect is again exemplified in speciation models in Figure 5.51, showing direct competition between L^1 and L^2 copper(II) complexes and how $[CuL^2_2]$ dominates at lower concentrations of ligand.

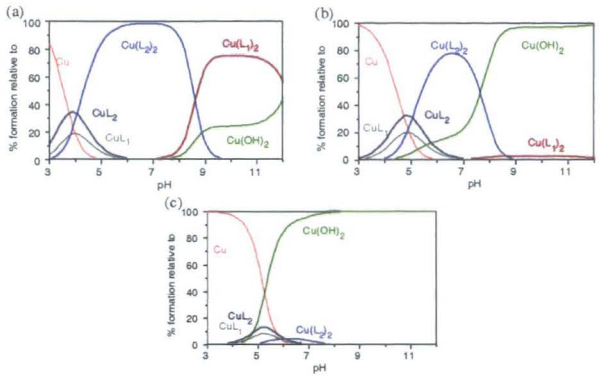

Figure 5.51 Species distribution of 1 μmol L^{-1} Cu^{2+} with competing ligands L^1 and L^2 at $[L_T]$ = (a) 1000 μmol L^{-1}, (b) 100 μmol L^{-1}, and (c) 10 μmol L^{-1}

The species distribution diagrams show that the L^2 trifluoromethyl sulfonamide ligand is able to bind copper at more acidic pH and therefore avoids competition with OH, as the relative concentration of ligand decreases.

Chapter 6

Voltammetric and Spectrophotometric Speciation of L^1 and L^4 Sulfonamide Complexes

6 Voltammetric and Spectrophotometric Speciation of L^1 and L^4 Sulfonamide Complexes

6.1 Introduction

Theoretical speciation models described in the previous chapter allowed a pictorial representation of the behaviour of metal species in solution. Speciation models were based on thermodynamic constants measured by varying the pH. However, it was also possible to measure the species in solution directly and to understand metal ion species' chemistry and electrochemistry directly.

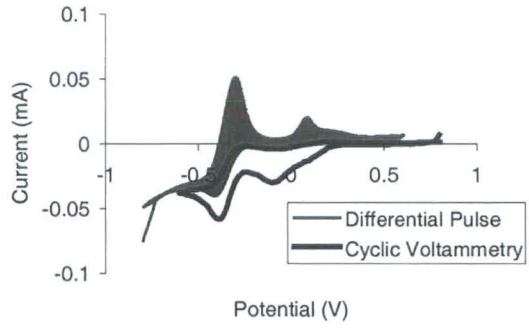

Figure 6.1 Differential pulse and cyclic voltammetry speciation of $[CuL^1_2]$ at pH 3.8 25mV s^{-1}

In this chapter cyclic voltammetry (CV) and differential pulse (DP) voltammetry (Figure 6.1) were used to observe ML_2 as well as ML^+ and M^{2+} species. Also, U.V. / visible absorbance data were collected using a fibre optic probe in the solution during voltammetric pH titration to allow comparison of results.

6.2 Voltammetric Speciation of Copper(II) L^1 and L^4 Sulfonamide Complexes

The well-defined $[CuL^1_2]$ complex was selected as a test case in order to assess factors such as concentration, scan rate, de-aeration, conditioning time and potential. An analysis procedure measuring CV, DP and U.V. / visible spectra was developed and used to evaluate metal ion speciation of copper(II), cobalt(II), nickel(II) and zinc(II) with L^1 and L^4 sulfonamide ligands. Complexes of ligands L^2 and L^3, each a trifluoromethylsulfonamide ligand, could not be studied further under the current conditions because of a lack of solubility and complex stability throughout the pH range.

6.2.1 Voltammetric Analysis free Copper(II) at a GCE

Differential pulse and cyclic voltammetry were firstly employed to analyse free Cu^{2+} ion current response in a background of 0.1 mol L^{-1} NMe_4NO_3 electrolyte and 80% methanol at a glassy carbon working electrode (GCE) vs. Ag/AgCl. The reaction vessel was kept under de-aerated condition to ensure potentiostatic oxidation of analyte rather than oxidation from surroundings.

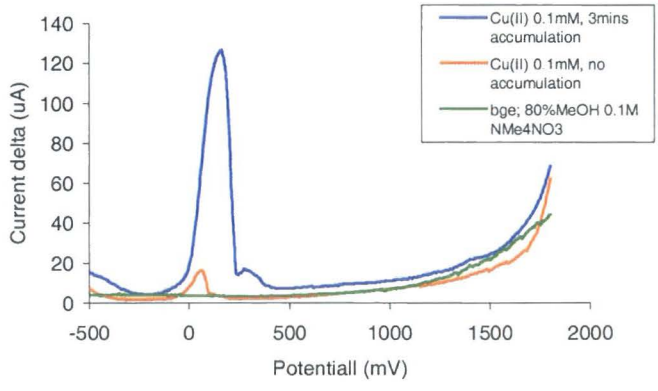

Figure 6.2 Effect of conditioning time on free Cu^{2+} DP-ASV at pH 2.1, 50 mV s^{-1} 3 mins conditioning at –0.5V with GCE

The peak potential $E_{p,a}$ of 0.17V was representative of the production of Cu(II) (Figure 6.2).[213] This is typically from two one-step processes

involving Cu and Cu(I) (Equation 6-1 and Equation 6-2). The presence of the two redox couples adds complexity to the analysis of the free metal signal.

Equation 6-1 $Cu^{2+} + e^{-} \leftrightarrow Cu^{+}; \quad E^{\circ} = +0.153V$

Equation 6-2 $Cu^{2+} + 2e^{-} \leftrightarrow Cu(s); \quad E^{\circ} = +0.337V$

The Cu^{2+} ion was adsorbed and held at the GCE surface during the reductive step without the use of a mercury film. However, the electrode surface became increasingly contaminated with adsorbed analyte. This necessitated regular polishing. Contamination of the GCE increased as the preconcentration potential became more negative. At a potential of –0.5V data was reproducible with little contamination. Preconcentration time had the expected effect of increasing free copper(II) current response (Figure 6.3).

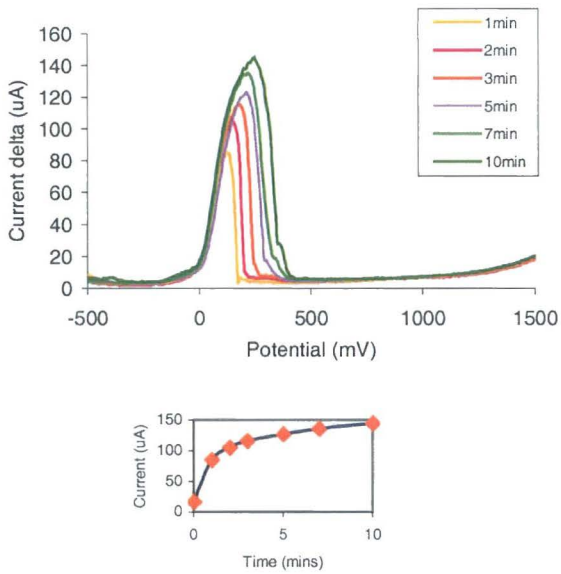

Figure 6.3 Effect of accumulation time on Cu(II) DP-ASV 50 mV s^{-1} at –0.5V conditioning potential

Figure 6.3 illustrates the significant increase in peak signal that is observed after one minute of conditioning. After this time, the current response

continued to increase at a lesser rate. A preconcentration time of 1 min was therefore adopted for subsequent differential pulse.

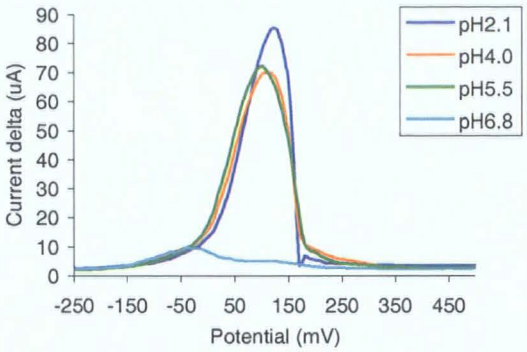

Figure 6.4 The differential pulse current response of 0.1mmol L^{-1} free Cu^{2+} with varied pH; 50 mV s^{-1}, 60 s conditioning at –0.5V

The effect of pH on stripping current for the free copper aquocomplex is seen in Figure 6.4. Copper(II) was rapidly hydrolysed and precipitated out of solution, as the [OH^-] increased. This expected behaviour is dictated by the log K_{sp} of $Cu(OH)_2$ = –20.4, and corresponds to hydrolysis at pH 5.98 (Table 4.3). In the presence of other ligands, competition inhibited hydrolysis from occurring until higher pH.

Cyclic voltammetry with free labile copper(II) at a GCE illustrates a number of features (Figure 6.5). The small anodic current *1a* was previously reported to be the oxidation of Cu to Cu(I).[212,213] The anodic peak *2a* is associated with formation of Cu(II) species from Cu and Cu(I).[213]

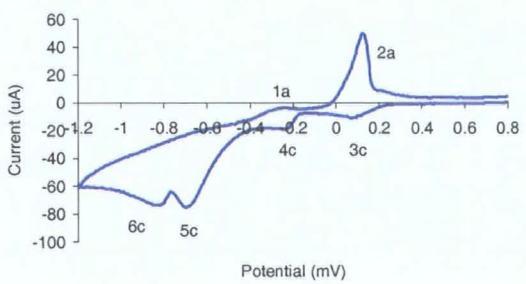

Figure 6.5 Cyclic voltammetry of labile copper peaks in 5 and 10 mmol L^{-1} copper(II) and L^1 at pH 2.65; 100 mV s^{-1}

The cathodic peak *4c* corresponds to the reduction of Cu(II) to Cu(I).[213] The peaks *5c* and *6c* result from the composite processes of Cu(II) to Cu, and Cu(I) to Cu.[213] The cathodic peak *3c* was associated with labile CuL^{+} present in solution.

Cyclic voltammetry at pH 3.3, indicated a shift in potential of the anodic Cu(II) peak as scan rate was increased. A nonlinear response of $i_{p,c}$ with $\sqrt{\nu}$ resulted indicated that this was an irreversible process, Figure 6.6.

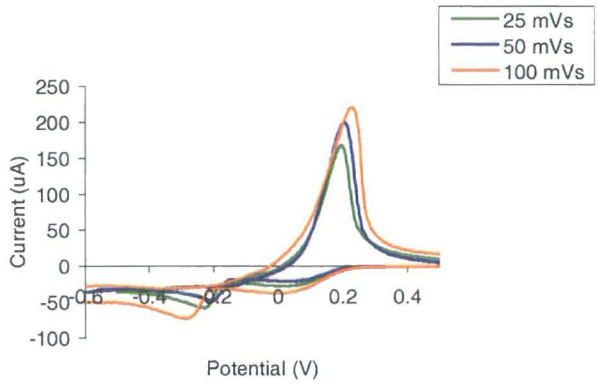

Figure 6.6 Cyclic voltammetry at pH 3.3 scan rate 25, 50 and 100 mVs^{-1} 5:10mmol L^{-1}

6.2.2 Analysis of Free L^1 Ligand

Background tests with free ligand, L^1, in 0.1mol L^{-1} NMe_4NO_3 and 80% MeOH demonstrated that no substantive interference of U.V. / visible spectra and voltammetric measurement were observed from pH 3.9 to 11.4 (Figure 6.7).

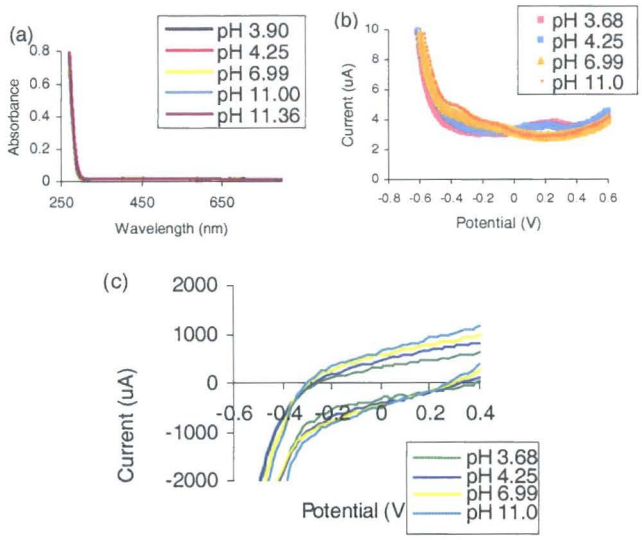

Figure 6.7 Background measurements of L^1 at 10 mmol L^{-1} concentration, pH 3.68 - 11.0, 80% MeOH 0.1 mol L^{-1} NMe_4NO_3 BGE N_2 atm (a) absorbance spectra, (b) differential pulse; 60 s conditioning at –0.8V 60 mV s^{-1} and (c) cyclic voltammetry; 25 mV s^{-1}

6.2.3 Reversibility of Copper(II) / L^1 Complex Species

Formation of the copper sulfonamide complex resulted in the appearance of a reversible redox. Nernstian behaviour dictates a peak separation of 59.16 mV according to

$$\text{Equation 6-3} \quad \Delta E = E_p^a - E_p^c = \frac{59.16}{n} mV$$

The CV of the $[CuL^1{}_2]$ had a peak separation of 120 mV ($E_{p,a}$ = -0.28V and $E_{p,c}$ = -0.4V). This signified a two-electron transfer from copper(II), Figure 6.8.

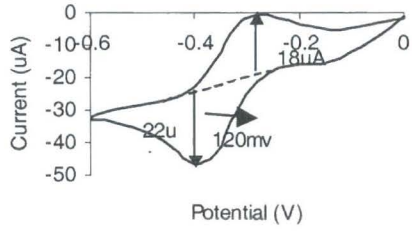

Figure 6.8 CV of $[CuL^1{}_2]$ redox; peak current ratio 18 μA / 22 μA = 0.82, ΔE_p = 120 mV, 40 mV s^{-1}, 5 and 10 mmol L^{-1} Cu^{2+} and L^1 respectively

The ideal ratio of peak currents for a reversible reaction is unity:

Equation 6-4

$$\left|\frac{i_p^a}{i_p^c}\right| = 1$$

The peak ratio for $[CuL^1{}_2]$ was 18 μA / 22 μA = 0.82, which indicated a less then ideal Nernstian response.

The peak current i_p for a reversible system is given by Randles-Sevcik equation, below.

Equation 6-5

$$i_p = (2.69 \cdot 10^5) n^{3/2} A C D^{1/2} \nu^{1/2}$$

Here, n is the number electrons, A is electrode area, C is concentration, D is the diffusion coefficient, and ν is scan rate. A reversible redox is, therefore, proportional to $\sqrt{\nu}$.

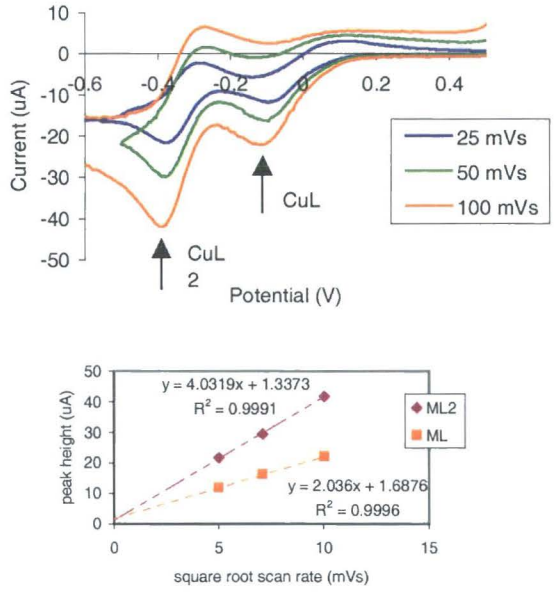

Figure 6.9 Cyclic voltammetry at pH 5.5 with scan rate 25, 50, and 100 mV s^{-1}; 5 and 10 mmol L^{-1} Cu^{2+} and L^1 respectively

The reversibility of $[CuL^1_2]$ and the $[CuL]^+$ species were evaluated by the proportionality of $\sqrt{\nu}$ to $i_{p,c}$, Figure 6.9. The $[CuL^1_2]$ redox couple gave an ideal linear response to this relationship at $E_{p,c}$ = -0.4V. Although a proportional response of the $[CuL]^+$ signal also signified a reversible reaction, the $E_{p,c}$ shifted from -0.11V to –0.13V for the increasing, respective, scan rates. This is indicative of an irreversible process.

6.2.4 Voltammetric Analysis of Copper(II) / L^1 Equilibria

The complex speciation of copper(II) / L^1 remained fairly constant, as long as $[L_T] > 2$ mmol L^{-1} (Figure 6.10). When $[L_T] < 2$ mmol L^{-1}, hydroxyl formation increases substantially. Ligand concentrations in species models in Figure 6.10 were used throughout this section to aid in the interpretation of voltammetric speciation data.

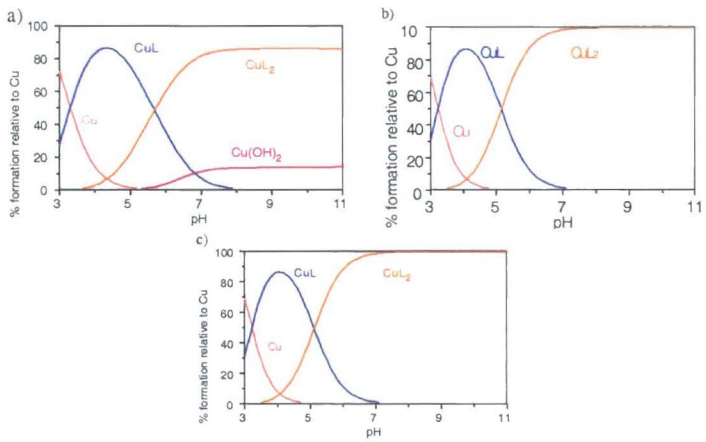

Figure 6.10 Species distribution diagrams of Cu^{2+}/ L^1 at (a) 5 and 10 mmol L^{-1} (b) 0.5 and 10 mmol L^{-1} and (c) 0.01 and 10 mmol L^{-1} (M/L)

Voltammetry, with fixed Cu^{2+}/ L^1 ratio and varied pH, indicated that ML^+ and ML_2 species had separate electrode potentials that could be measured simultaneously (Figure 6.11). These measurements were a good agreement with speciation models created from potentiometric data.

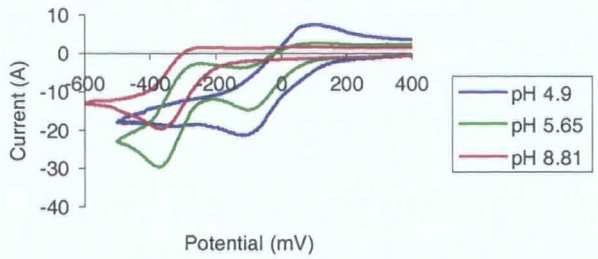

Figure 6.11 Cyclic voltammetry of Cu^{2+}/ L^1 speciation 5 and 10 mmol L^{-1} 50 mV s^{-1}, de-aerated solution

Cyclic voltammetry at pH 4.9 and 8.8 corresponded to predicted maximum $[ML^+]$ and $[ML_2]$, according to Figure 6.10. The position of the ML_2 redox potential was confirmed with measurements of $[CuL^1{}_2]$ previously taken in acetonitrile.[59] The two species were present at pH 5.7, as predicted in the model (Figure 6.10).

The intensity of the current response of ML_2 was diminished relative to the free Cu^{2+} signal (Figure 6.12). This was caused in part by the altered diffusion characteristics of the complex species.

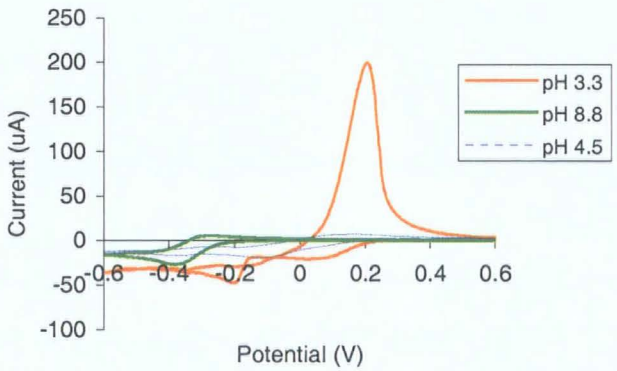

Figure 6.12 Cyclic voltammetry of M^{2+}, ML^+ and ML_2 Cu^{2+}/ L^1 species; 5 and 10 mmol L^{-1} (M/L), 25mV s^{-1}, de-aerated solution

The oxidation peak of free Cu^{2+} at pH 3.3 was observed at 0.2V (Figure 6.12). As the pH increased, free Cu^{2+} signal rapidly dissipated. At pH 4.5, formation of metal complex species was indicated by reduction at –0.125V. This peak was clearly separate from ML_2 redox signal, and was thus

attributed to ML^+ formation. In more alkaline media, the reversible peak observed at –0.31V was ML_2 redox.

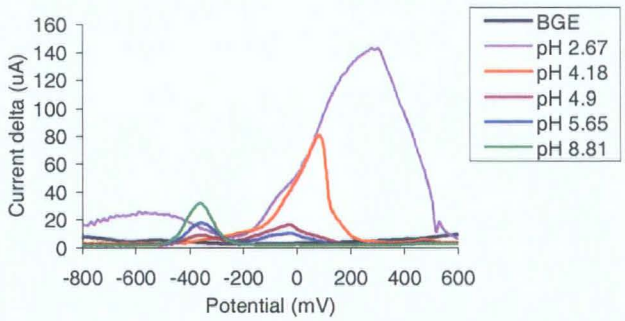

Figure 6.13 DP-ASV of Cu^{2+}/ L^1 speciation; 5 and 10 mmol L^{-1} (M/L), 60s conditioning at –1.2V 50mVs^{-1}, de-aerated solution

Similarly, differential pulse coincided with a rapid decrease in M^{2+} at 0.2V. The peak potential E_p of the labile peak shifts to -0.05V, which was attributed to the formation of ML^+. The formation of a peak current at –0.35V was assigned to the formation of the electroactive ML_2 complex (Figure 6.13). This ML_2 peak was separate from the labile copper(II) fraction since the complex does not dissociate to a significant degree during the time of the experiment.

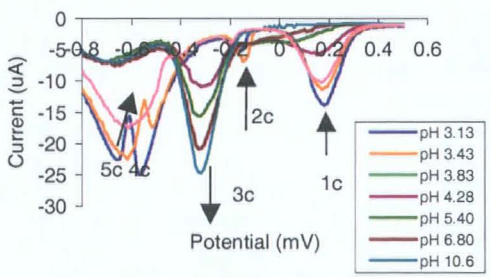

Figure 6.14 5 and 10 mmol L^{-1} Cu^{2+} / L^1 speciation with cathodic differential pulse; 60 s at 0.5V, 50 mV s^{-1}

Formation of $[CuL^1_2]$ was also observed with cathodic differential pulse (Figure 6.14), illustrating the altered reduction potentials of the central metal atom as it was coordinated by the sulfonamide ligand. In Figure 6.14, cathodic peaks 1c, 2c, 4c and 5c correspond to reductions associated with the

labile CuL^+ peak, Cu(II) to Cu(I), Cu(I) to Cu, and Cu(II) to Cu reductions, respectively.[213] All of these redox couples dissipate as pH increases, while the cathodic peak 3c, attributed to the formation of the ML_2 species and its subsequent reduction, increases ($CuL^1{}_2 + 2e \rightleftharpoons Cu + 2L^-$).

6.2.5 Effect of Concentration on Voltammetric Speciation of $[CuL^1{}_2]$

Species distribution of copper(II) was altered by varying $[L_T]$. Voltammetric and potentiometric models were in good agreement. Species models indicated that $[ML^+]$ was maintained relative to rapidly decreasing $[ML_2]$ at a concentration of 1 and 2 mmol L^{-1} (M/L) (Figure 6.15). In addition, the ML_2 species is charge neutral, and not subject to preconcentration from application of reducing potential prior to analysis. Therefore, sensitivity is not enhanced relative to charged ML^+ and M^{2+} species. The result is illustrated in Figure 6.16. The ML_2 signal was reduced in intensity relative to the ML^+ peak.

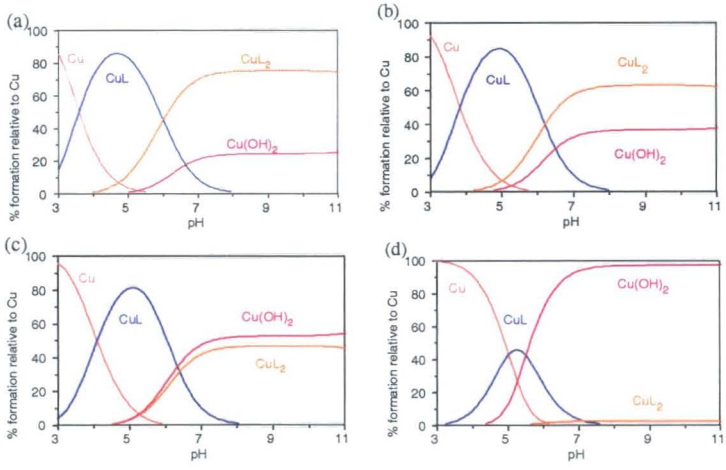

Figure 6.15 Species distribution diagrams decreasing concentration at 1:2 ratio (a) 2 and 4 mmol L^{-1} (b) 1 and 2mmol L^{-1} (c) 0.5 and 1mmol L^{-1} and (d) 0.05 and 0.1 mmol L^{-1}

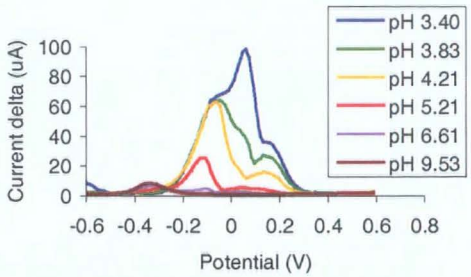

Figure 6.16 DP-ASV 1:2 mmol L^{-1} Cu^{2+}/ L^{1} speciation 60 s conditioning at –1.2V 50 mV s^{-1} de-aerated solution

Each differential pulse curve in Figure 6.16 was individually scaled below to accentuate the sequential movement of the copper complex formation (Figure 6.17). Three distinct potentials relating to ML_2, ML^+ and M^{2+} at –0.34V, -0.11V and 0.08V, respectively, were observed.

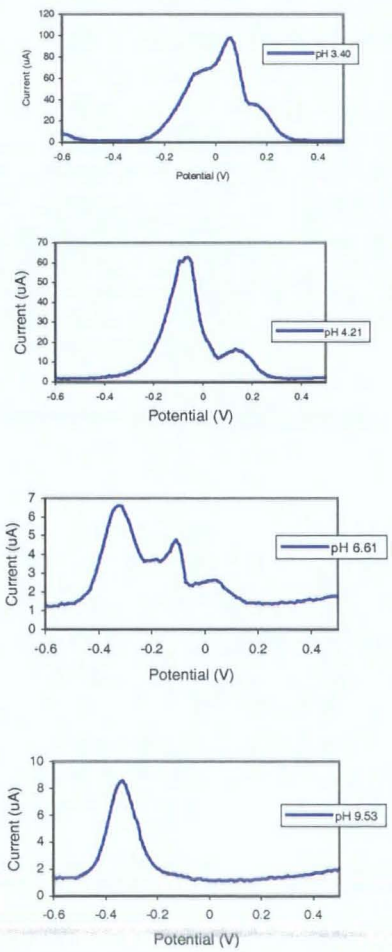

Figure 6.17 Individual DP-ASV runs from Figure 6.16; 1 and 2 mmol L^{-1} Cu^{2+} / L^{1}

In future determinations aimed at targeted sensing of copper(II) through adsorptive binding with this ligand, it may be best served with ML^+ signal at pH 4-5. This is because the increasing competition with OH^-, at lower ligand concentration, would make measurement of the metal ion at ambient pH more prone to hydrolysis. However, a thorough understanding of speciation would be required to anticipate shifts in the labile copper(II) peak.

6.2.6 Effect of De-aeration of Solution

De-aeration of solution with inert gas is important in voltammetry, especially when using stripping techniques. Differential pulse-anodic stripping was used to illustrate the effects of de-aeration on sensitivity and altered species distribution caused by the altered preconcentration of neutral and charged species.

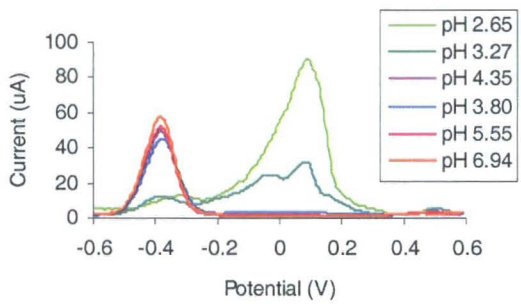

Figure 6.18 DP-ASV of 5 and 10 mmol L^{-1} Cu^{2+}/ L^1 speciation; non de-aerated, 60 s conditioning at –1.2V, 50 mV s^{-1}

The DP-ASV recovery of positively charged analyte was reduced in absence of a de-aerated solution. The M^{2+} and ML^+ peaks in Figure 6.18 at concentration 5 and 10 mmol L^{-1} (M/L) were ~ 50% of previously observed i_p (Figure 6.13).

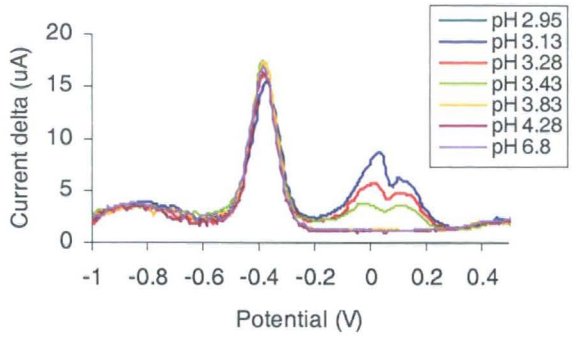

Figure 6.19 DP-ASV 1:2 mmol L^{-1} Cu^{2+}/ L^{1} speciation; conditioning 60s at –1.2V 60mVs^{-1} non de-aeration

The effect was more pronounced at a lower concentration of 1 and 2 mmol L^{-1} (M/L). The peak signal of charged species, ML^{+} and M^{2+}, decreased ten-fold (Figure 6.19). The ML_2 oxidation was unhampered by the lack of de-aeration (Figure 6.16).

6.2.7 Detection of the CuL^{+} Species

The ML^{+} was individually addressed by choosing an appropriate pH and ligand concentration. Models indicated with pH of 4.07, $[L_T]$ = 10mmol L^{-1}, and $[M_T]$ = 0.01mmol L^{-1}, in percentage terms, speciation was 86% ML^{+}, 7% M^{2+} and 7% ML_2 (Figure 6.10). With these experimental conditions, differential pulse was used to examine the speciation.

A standard addition of copper(II) was added to the solution containing $[L_T]$ = 10 mmol L^{-1} at pH 4.07. Using differential pulse, an oxidation peak at –0.08V was observed (Figure 6.20). From previous observations the peak at –0.08V was assigned to the ML^{+} signal.

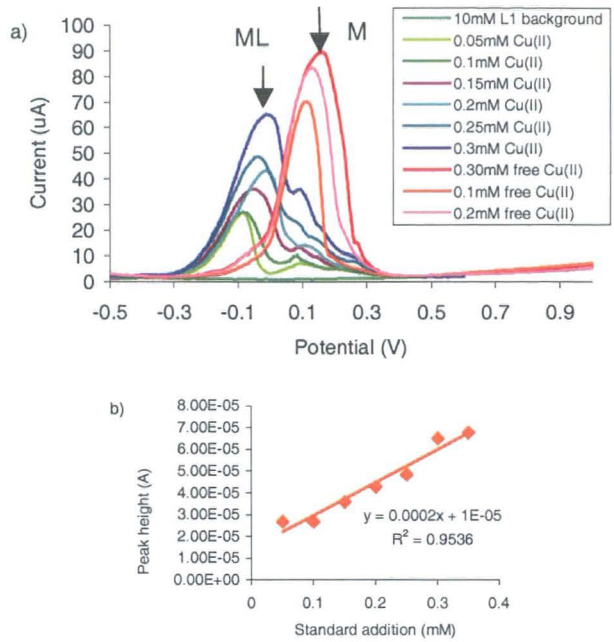

Figure 6.20 DP-ASV standard addition Cu^{2+} at pH 4.05 with (a) [L_T] = 10 mmol L^{-1}, and (b) [L_T] = 0; 60 s at –1.0V, 50 mV s^{-1}

At a concentration of 1 and 2 mmol L^{-1} (M/L) the species model (Figure 6.15) indicated that ML^+ formation was maximised at pH 5.24. In percentage terms, speciation was expected to be 86% ML^+, 11% ML_2, and 3% M^{2+}. Cyclic voltammetry under these conditions agreed qualitatively with the predictions. An optimised ML^+ peak at –0.09V was observed (Figure 6.21).

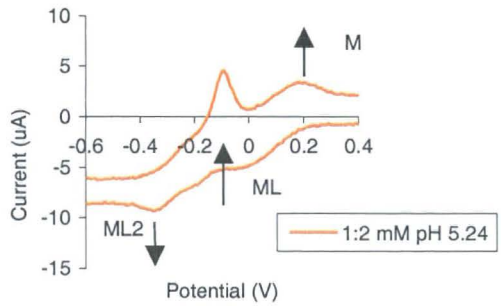

Figure 6.21 CV of Cu^{2+}/ L^1 current response at 1 and 2 mmol L^{-1} (M/L); 100 mV s^{-1}, de-aerated solution

Metal speciation in solution may be interpreted qualitatively using voltammetry in conjunction with potentiometric equilibrium models, as

depicted above (Figure 6.21). However, the actual refinement of stability constants that involves simultaneous solution of mass balance equations, is possible only if either the free metal ion, free ligand or free proton concentration, [M], [L], or [H], respectively, which can vary over a wide concentration range, be monitored with high accuracy throughout an experiment.[214]

6.2.8 Voltammetric Determination of Complex Formation Equilibria of Copper(II) / L^1 & Copper(II) / L^4 Systems

Simultaneous measurement of U.V. / visible spectra, cyclic voltammetry, differential pulse and pH was carried out via a flow apparatus at a fixed $[M_T]$:$[L_T]$ ratio of 5 and 10 mmol L^{-1}. This concentration was appropriate for potentiometric and spectral measurements, as well as for qualitative examination of voltammetric peaks.

6.2.8.1 Copper(II) / L^1 Voltammetric Titration

The objective here was to obtain quantitative voltammetric data for copper(II) / L^1 equilibria. Following a mathematical treatment developed by Cukrowski,[215] measurements of i_p and E_p at varied pH could theoretically be used to create 'virtual' potentiometric data, which would be selective to $[M]_{free}$. This 'virtual' potentiometric data could be used to refine mass balance equations in a dedicated program, such as *Hyperquad,* to obtain complex formation constants.

Cyclic voltammetry of the Cu(II) / L^1 system, showed observations previously discussed. The intensity of the oxidation current of free copper was much greater due to the altered diffusion coefficients of the metal as it was complexed by the ligand.

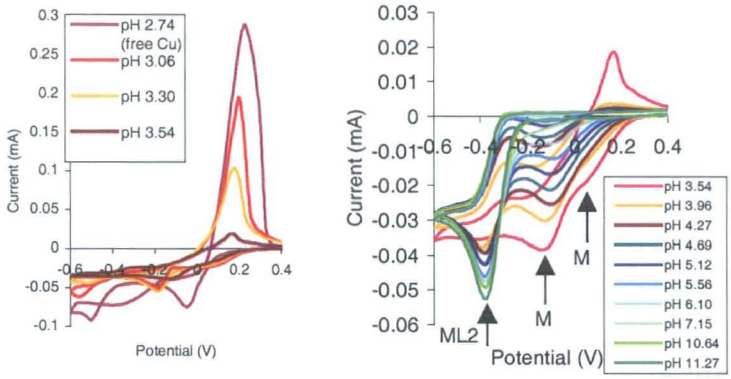

Figure 6.22 Cyclic voltammetry of 5 and 10 mmol L^{-1} copper(II) / L^{1} solution; 25 mV s^{-1}

The pH data set was initially analysed with *Hyperquad* (Figure 6.23a). The refined formation constants were identified as $\beta_{ML} = 11.68$ and $\beta_{ML2} = 20.83$. These values were used to construct a species distribution model (Figure 6.23b).

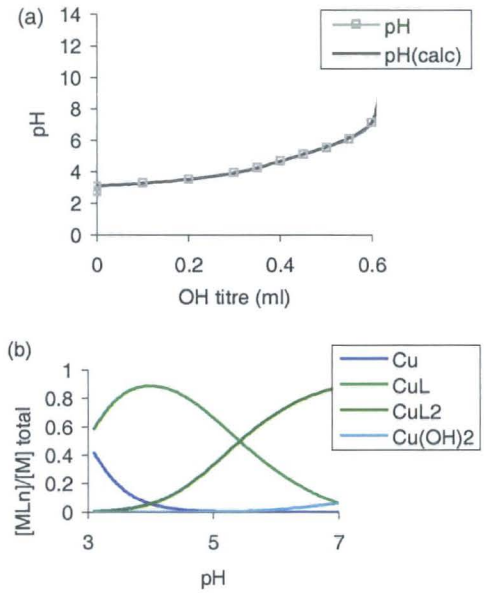

Figure 6.23 pH titration recorded simultaneously with voltammetric titration data (a) experimental and refined model titration curve, and (b) species distribution model; 5 and 10 mmol L^{-1} copper(II) / L^{1}

The $[M_T]$ and [M] values, obtained from a *HySS* titration simulation model (Figure 6.23b), were used to calculate the right hand side of Equation 3-9 and plotted vs. the OH titre. This model titration curve represented the computed complex formation curve (CCFC) (Figure 6.24a), from which the experimental complex formation curve (ECFC) was fit.

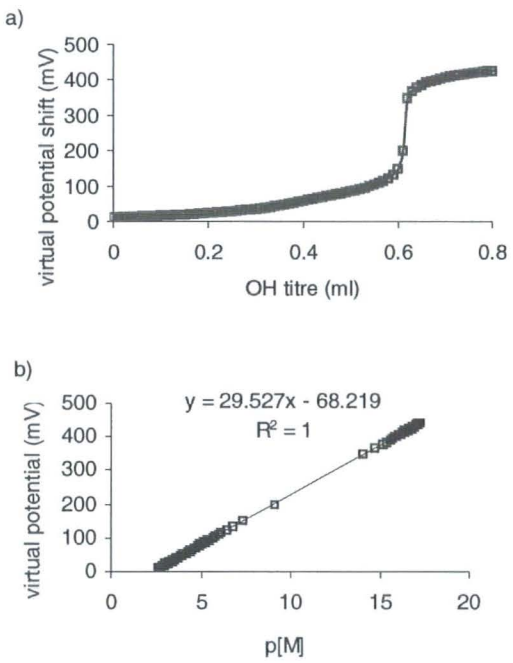

Figure 6.24 A 'virtual' potentiometric model for Cu(II) / L^1 equilibria based on $\ln([M_T]/[M])$; a) simulated titration curve, b) virtual potential vs. p[M]

The experimental complex formation curve is constructed by monitoring the $[M]_{free}$, using i_p and E_p values for the labile metal ion peak, with and without, the presence of the ligand. The $[M]_{free}$ is assessed by the shift of the labile peak to a more negative potential, as the complex species are formed. This reflects the additional energy required for the decomposition of the complex.

It is imperative to have an accurate, well-defined I(M) value and subsequent I(comp) measurements. Although the differential pulse (Figure 6.25a) shows a well-defined ML_2 oxidation at –0.3V, the free copper(II) peak, in this case, was distorted. The [L]:[M] ratio would have to increase from 2:1, used here, to about 30:1 for a better result.[162] At this ratio, however, it would not be

possible to construct a conventional potentiometric model. A 2:1 ratio was used to ensure a good outcome with potentiometric and spectrophotometric measurement of equilibria, but this hampered efforts to obtain reliable differential pulse or cyclic voltammetry data for free copper(II) peak currents.

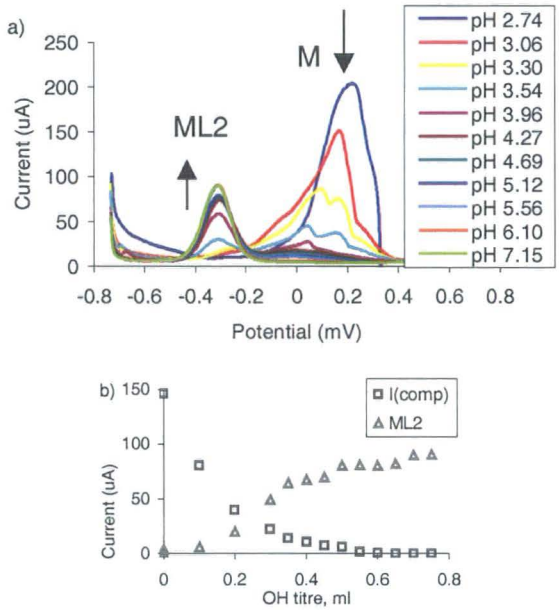

Figure 6.25 Differential pulse pH titration; 5 and 10 mmol L^{-1} copper(II) / ligand, 25 mV s^{-1}

For example, in this instance, the virtual potential shift may be calculated by:

Equation 6-6

$$\Delta E_{pH_i} = (0.225 - E(comp))_{pH_i} - \frac{59.16}{2} \cdot \log\left(\frac{I(comp)}{183.07}\right)_{pH_i}$$

Here, virtual potential shift, ΔE, values are the experimental function used to fit the equilibrium model for each pH value. The E(M) value of 0.225V represents the initial free copper E_p, and 183.07 μA is the free copper i_p I(M), from which all ΔE values are based. The potential values can only be calculated in the part of the curve where [Cu] is present, i.e., prior to the neutralization point, here, represented at 0.6 ml OH (Figure 6.26).

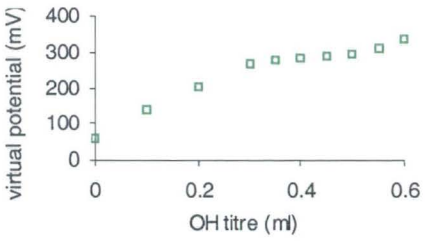

Figure 6.26 Experimental complex formation curve derived from differential pulse data for 5 and 10 mol L copper(II) / L^1

The experimental virtual potential values in Figure 6.26 could not be refined with the model. Empirically, however, the magnitude of the shift appears to agree with a two-electron process. The primary cause for the distortion of the labile copper(II) current peak was the ratio of $[L_T]$:$[M_T]$. The ratio must be ~ 30, in order to maintain constancy of $[L_T]$ at the electrode surface.

6.2.8.2 Copper(II) / L^4 Voltammetric Titration

The formation of the electroactive $[CuL^4_2]$ complex, also studied by voltammetric and spectrophotometric titration, is compared with $[CuL^1_2]$ redox in Figure 6.27. The position of the $E_{½}$ was an indication of the augmented stabilization energy obtained from the formation of a square planar complex for $[CuL^1_2]$ (-0.33V). The $[CuL^4_2]$ complex had a more positive redox potential of $E_{½}$ = – 0.21V caused by the formation of a distorted tetrahedral complex.

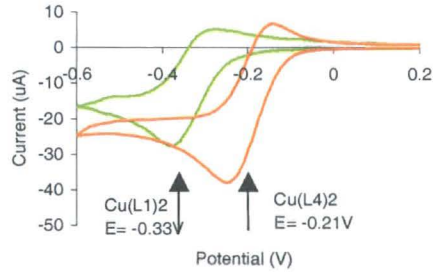

Figure 6.27 Comparison of cyclic voltammograms of $[CuL^1_2]$ and $[CuL^4_2]$; 5 and 10mmol L^{-1} (M/L)

The $[CuL^4_2]$ complex had a redox couple in keeping with a reversible two-electron transfer, with peak potentials of $E_{p,c}$ = -0.275V and $E_{p,a}$ = -0.125V. The peak separation was ΔE_p = 125 mV (Figure 6.27). Peak current ratio, $i_{p,a}$ / $i_{p,c}$ was 0.72, which was well below unity. This indicated a possibly quasi-reversible process.

Cyclic voltammetry, differential pulse and U.V. / visible spectra, at varied pH with the 5 and 10 mmol L^{-1} copper(II) / L^4 were recorded simultaneously. The smaller LFSE contribution has the effect of shifting the ML_2 reduction to a more positive potential of $E_{½}$ = –0.21V. Again, the lability of the free and fully complexed species is apparent with current intensity being much greater for free copper.

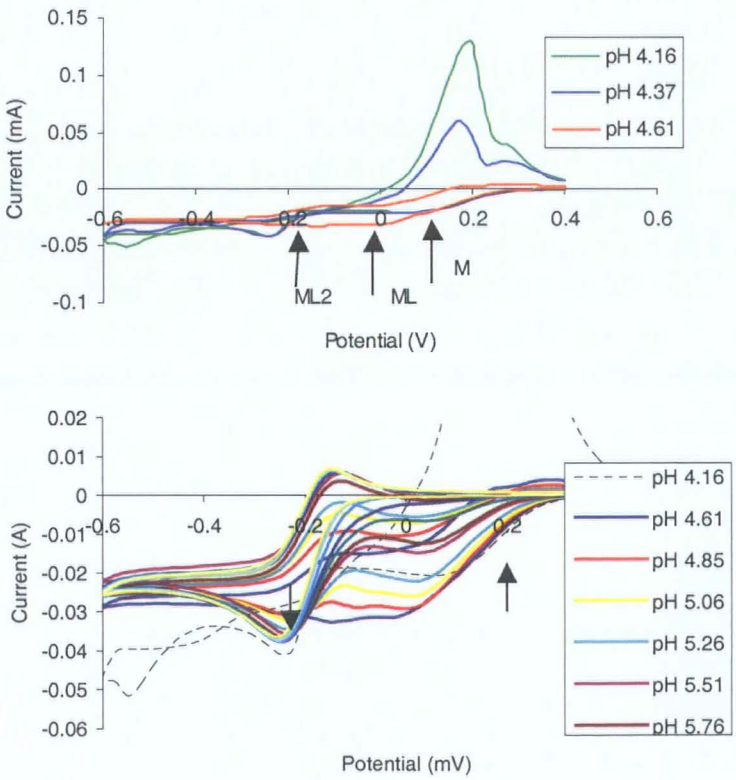

Figure 6.28 Cyclic voltammetry pH titration 5 and 10mmol L^{-1} Cu^{2+}/ L^4 25mVs^{-1}

A qualitative assessment of $[CuL^{+}]$ is not possible because separation between M^{2+} and ML_2 is less by ~ 0.2V. However, differential pulse measurements clearly show the transition between the labile metal fraction and the ML_2 complex (Figure 6.29).

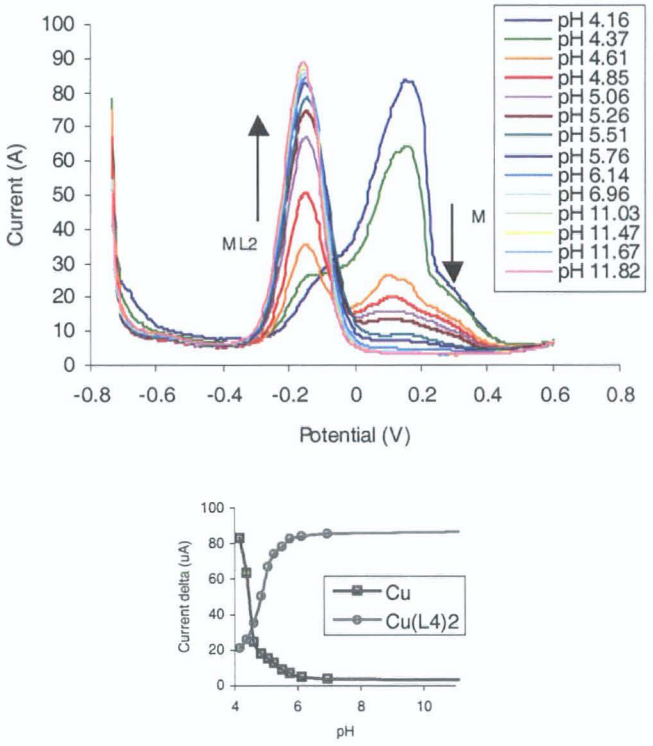

Figure 6.29 Differential pulse pH titration 5 and 10mmol L^{-1} Cu^{2+}/ L^4 60s conditioning at –0.8V 25mVs^{-1}

Using i_p and E_p differential pulse values for the labile current response (Figure 6.29), 'virtual' potentials were calculated in the same way as just described. The outcome was very similar in that, although valuable data were obtained potentiometrically and spectrally, voltammetric analysis required a larger excess of ligand. The E(virt) values could not be refined with the model constructed with potentiometric data collected simultaneously (Figure 6.30).

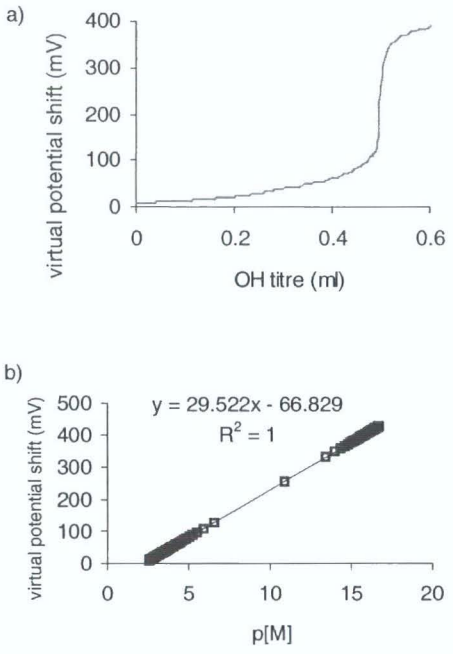

Figure 6.30 A 'virtual' potentiometric model for Cu(II) / L^4 equilibria based on $\ln([M_T]/[M])$; a) simulated titration curve, b) virtual potential vs. p[M]

6.2.8.3 Cobalt(II) / L^1 Voltammetric Titration

Differential pulse, cyclic voltammetry and U.V / visible spectra were recorded with the automated pH titration apparatus as previously employed with copper(II).

Species distribution diagrams of 5 and 10 mmol L^{-1} cobalt(II) / L^1 solution were used as a guide to evaluate resultant voltammetric and spectrophotometric data. The model showed that M^{2+} and MLH dominated in the acidic region, and ML^+ was present ~70% at pH 7.5.

Cyclic voltammetry of 5 and 10 mmol L^{-1} Co^{2+} / L^1 equilibria, gave a shifting redox current in the positive region related to cobalt current response. Voltammetric conditions were optimised with potential range –1.4V to 0.9V at 75 mV s^{-1}. In the positive range, the voltammogram shows an oxidative current at 0.6V that steadily increases until pH 7.45, this was attributed to

formation of ML^+. Then redox potential shifts to more negative potential. The redox in this region could have been caused by an $ML_n(OH)_m$ species

There was no well-defined electroactive labile peak identified under the present conditions. Therefore, further voltammetric investigation with this M-L system at a GCE, was not undertaken.

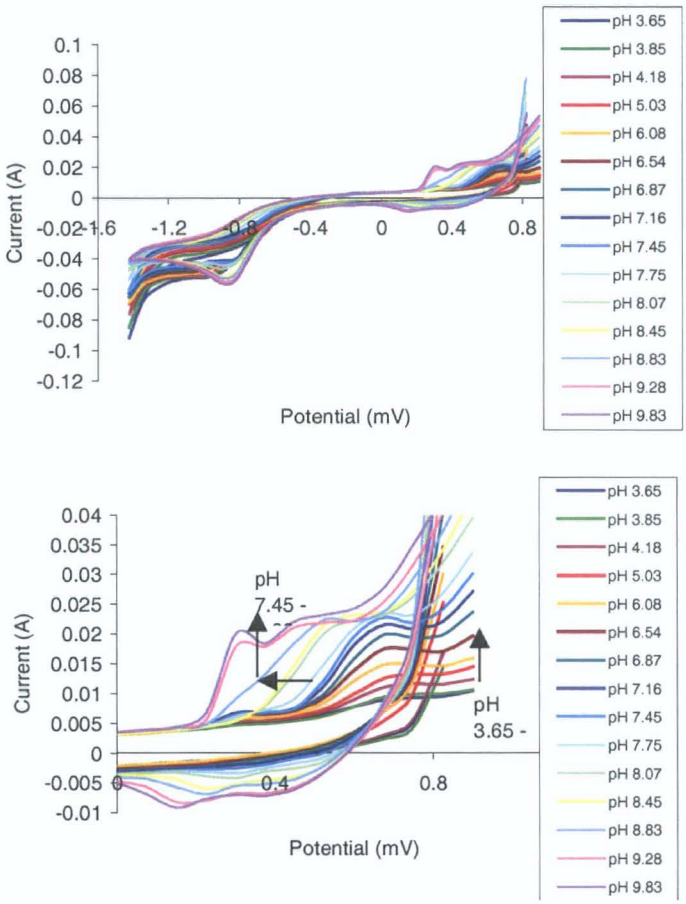

Figure 6.31 Cyclic voltammetry 5:10mmol L^{-1} Co^{2+}/ L^1 75mVs^{-1}

6.2.8.4 Nickel(II) and Zinc (II) / L^1 Voltammetric Titration

Precipitation was found to occur at pH 7.5 with both metals, which hampered efforts at equilibrium investigation because of weak binding. There was no well-defined reduction identified for nickel(II) at the current conditions. Zinc(II) analysis was not reproducible with a bare glassy carbon

electrode, under the current conditions. Therefore no further experiments were undertaken with a GCE under these conditions.

6.3 Spectrophotometric Determination of Complex Formation Equilibria

The absorbance spectra of the metal-ligand systems were observed as a function of pH by simultaneous voltammetric spectral pH titrations. Absorbance data were used to successfully refine complex formation constants with *pHab* software.[216]

6.3.1 Copper(II) / L^1 U.V. / Visible Absorbance titration

The copper(II) complex gave rise to two main transitions (Figure 6.32) a ligand-to-metal charge transfer (LMCT) at 380 nm and a d-d transition in the 600-800 nm range.

The wavelength peak, λ_{max}, shifted from 762nm at pH 3.06 to 630nm at pH 7.15. This indicated an increase in energy associated with the widening of HOMO $\rightarrow$ LUMO caused by greater ligand field strength during formation of the square planar $[CuL^1{}_2]$ complex. The shape of the λ_{max} and absorbance curves, showed a plateau after pH 7.0 that was in keeping with the formation of ML_2 species according to species distribution models (Figure 6.23b).

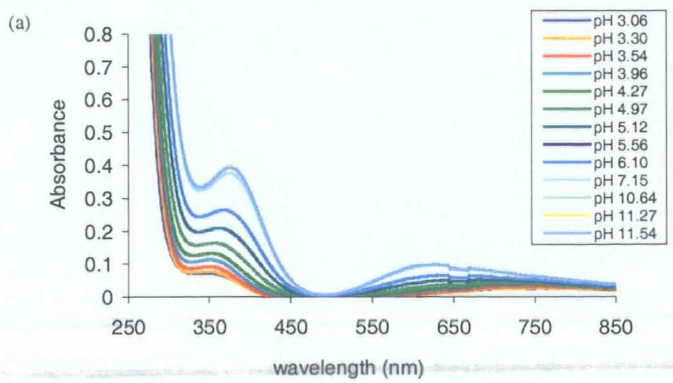

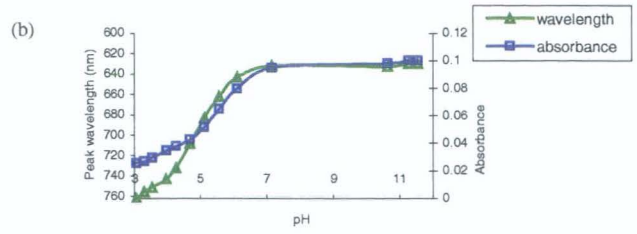

Figure 6.32 (a) Spectral titration of 5 and 10 mmol L^{-1} copper(II) / L^1 solution (b) λ_{max} and absorbance vs. pH at 630nm

Absorbance titration data sets were analysed using *pHab* software[216] to determine the formation constants for the system. The determination of constants from absorbance data, firstly, required that the weighting of errors on the absorbance values be estimated. Since absorbance errors usually depend on the magnitude of absorbance, a functional relationship between absorbance and absorbance error, may be obtained. The error function, calculated in *pHab*, gives the absorbance data reasonable weights in the least-squares process of refining formation constants (Figure 6.32).

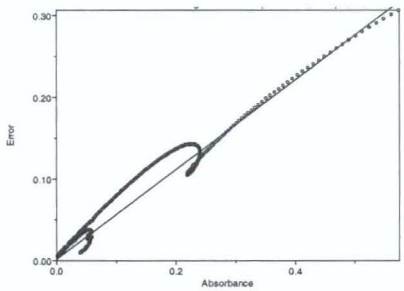

Figure 6.33 Linear error function for absorbance data of copper(II) / L^1 titration calculated in *pHab*

.

The refinement procedure was similar in format to that of *Hyperquad.* Spectral data sets were loaded into the refinement model. The wavelengths were chosen in the absorbing regions of the curve. Previously reported ligand protonation values were added to the model. The refined values of absorption for each selected wavelength are fit with experimental values. The refined β constants agreed well with the previously established values (Table 5-11) with $\beta_{ML} = 11.58 \pm 0.06$ and $\beta_{ML2} = 20.98 \pm 0.06$ (Figure 6.34).

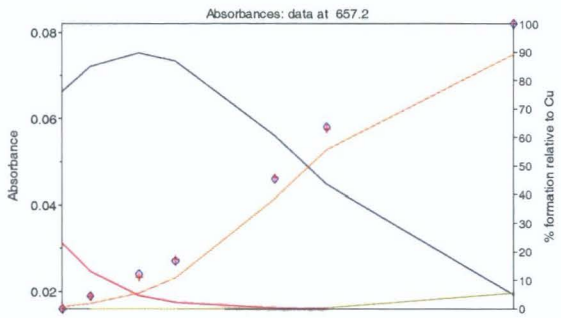

Figure 6.34 Absorbance and speciation of copper(II) / L^1 at 657 nm; ◊ experimental, + model; species present -- M, -- ML, -- ML_2, -- $M(OH)_2$

For a higher degree of accuracy a larger set of pH values would be needed. Although potentiometric data reported previously was more reliable in this instance, the spectrophotometric stability constant refinement approach gives a greater amount of certainty compared with a simple potentiometric titration since a model can be fit at upwards of one hundred wavelengths per pH value.

6.3.2 Copper(II) / L^4 U.V. / Visible Absorbance titration

Absorbance measurement of the $[CuL^4_2]$ complex formation provided more evidence of the steric hindrance that inhibited the complex from forming a square planar complex. Absorbance data show a strong absorbance with a ligand-to-metal charge transfer at 451 nm and another peak associated with *d-d* transition (Figure 6.35a). The absorbance data demonstrated that there was not a significant change in LFSE during complexation, with only a small shift in λ_{max} from 801nm to 796nm (Figure 6.35b & c).

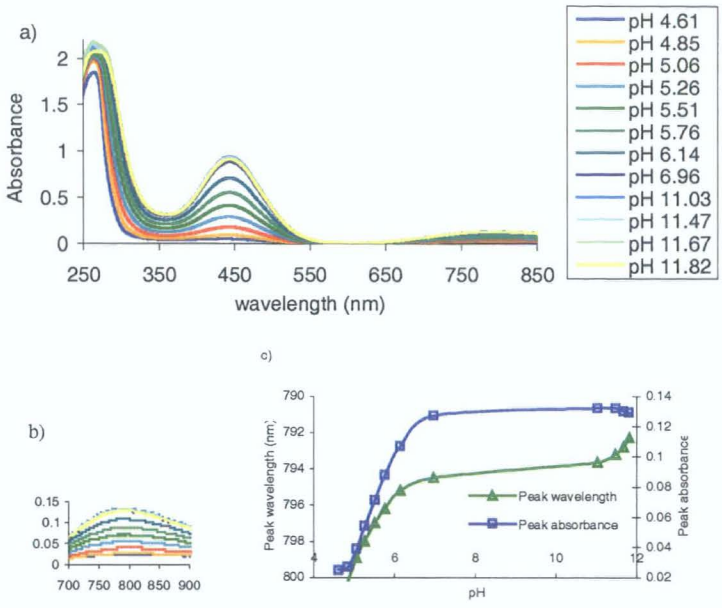

Figure 6.35 (a) Titration absorbance spectra of 5 and 10mmol L^{-1} Cu^{2+}/ L^4 (b) λ_{max} and absorbance vs. pH

Hydrolysis was noted at a pH of 11 by the slight shift to lower wavelength, and by a decrease in absorbance (Figure 6.35c). Refinement was consistent with values previously reported in this study (Table 5-12) with $\beta_{ML} = 9.98 \pm 0.014$ and $\beta_{ML2} = 18.26 \pm 0.0269$ (Figure 6.36).

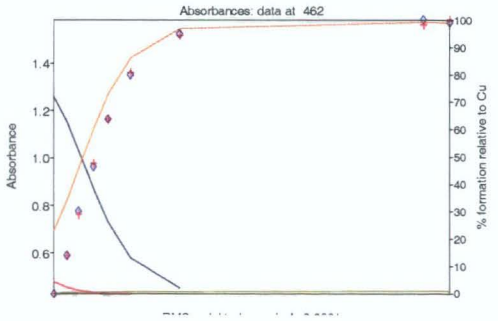

Figure 6.36 Absorbance and speciation of 5 and 10 mmol L^{-1} copper(II) / L^4; ◊ experimental, + model; species present -- M, -- ML, -- ML_2, -- $M(OH)_2$

6.3.3 Cobalt(II) / L^1 U.V. / Visible Absorbance titration

Absorption spectra were recorded for cobalt(II) / L^1 solution at concentrations of 5 and 10 $mmol^{-1}$. Absorbance titration was again

advantageous in that it easily detected the pH value where precipitation commenced. Data above pH 8.45 were omitted from the model refinement.

The λ_{max} attributed to the *d–d* transition shifted from 483 nm to 516 nm during formation of the cobalt(II) complex. The low absorbance values observed created uncertainty with the calculation of cobalt(II) equilibria under the current conditions (Figure 6.37b).

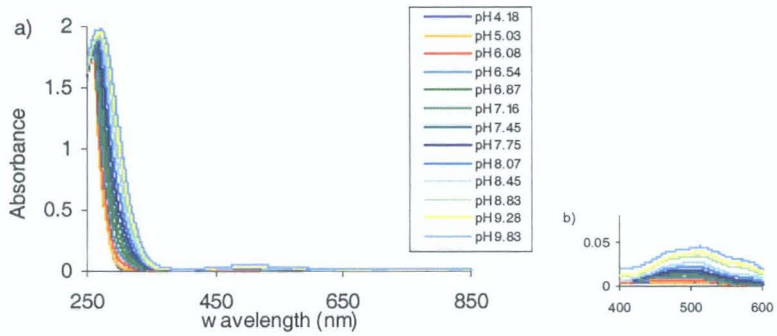

Figure 6.37 Absorbance titration of 5 and 10 mmol L^{-1} cobalt(II) / L^{1}

Data above 350 nm was largely not acceptable due to a lack of well-defined absorption. Below 350 nm the charge transfer transition was much higher, and as the refinement model shows (Figure 6.38), wavelength data at 293 nm agreed well with the calculated values. However, from this data only β_{ML} was refined to a value of 7.98 ± 0.08. This correlated well with potentiometric models but is more uncertain than potentiometric results previously reported at this concentration (Table 5-11).

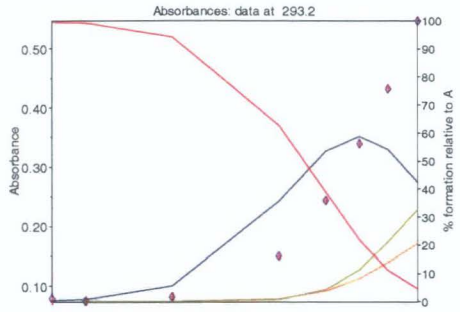

Figure 6.38 Absorbance and speciation of cobalt(II) / L^1 at 293nm; ◊ experimental, + model; species present -- M, -- ML, -- ML_2, -- $M(OH)_2$

The combined measurement of absorbance and voltammetric response at constant [M]:[L] ratio and varied pH, was a useful technique in that it allowed for increased amount of data to be collected from the same experiment. This enabled more assurance of the refined formation constant values, and enabled comparison with electroactive species obtained with voltammetry.

Chapter 7

Chromium Speciation in Leather Tanning Waste

7 Chromium Speciation in Leather Tanning Waste

7.1 Introduction

In the course of this study, chromium detection was carried out in industrial samples of leather tanning waste. Leather tanning is the treatment of natural collagen fibre of animal hide to stabilize and toughen the material. Stabilisation of hide leads to increased water resistance and restricted swelling, and avoids putrefication and drying of leather into an inflexible mass.[217] Tanning also leads to the change of appearance and feel, as well as boilfast attributes useful in industry.

Hide is made up of a series of layers that perform different functions such as hair growth, chemical barriers, blood supply, flexibility, etc, and in doing so have different molecular compositions. A set of chemical procedures is carried out to eliminate unwanted material, eventually leaving a composition mostly of collagen and elastin.[217] The tanning procedure uses chromium(III) to form stable cross-linkages between collagen micro-fibrils.

Collagen micro-fibrils are primarily a triple-helix structure caused by the orderly tripeptide periodicity of the amino acid pattern gly-X-Y, where X and Y are variable amino acids.[217] The gly-pro-hyp is a collagen-typical pattern that is bunched in clusters along the chain. Between these clusters are the 'valleys' where charged tripeptides occur, i.e. gly-glu-asp. This is where chromium(III) cross-linking of carboxyl groups occurs. Figure 7.1 illustrates the single collagen chain folding around itself for stability, the twisting chain wraps around two others to form a triple-helix. Small lobes denote tripeptide areas that contain carboxyl-binding groups.

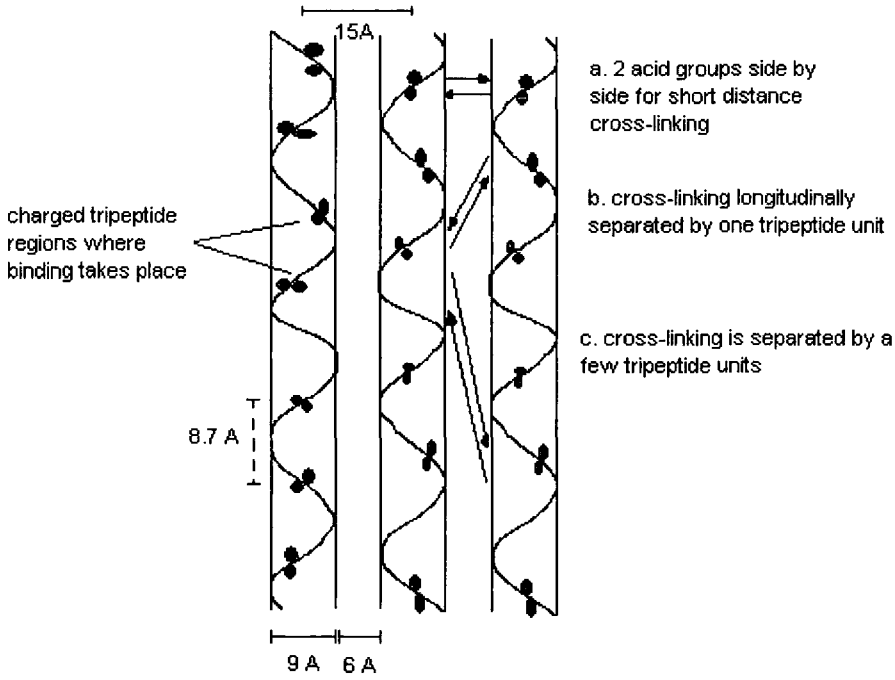

Figure 7.1 Chromium(III) binding sites in collagen during tanning process[217]

Cross-linking distances illustrated in Figure 7.1 are (a) 9A°, (b) 15A°, and (c) 20A°. Alkaline chromium(III) tanning solutions contain mainly complexes of 2, 3, and in minor part, 4 nuclear entities that correspond to extensions of 7A°,12A° and 17A°.[217] Cross-linking distance between carboxyl binding groups on a single collagen micro-fibril also corresponds to a chromium(III) dimer extension with distance of 8.7A° illustrated in Figure 7.1.[217] Acid groups commonly occur side-by-side in tripeptide arrangements. This leads to the following binding structure in Figure 7.2. Chromium(III) is naturally accommodating in this hydrolytic capacity showing why it is ideal for this application.

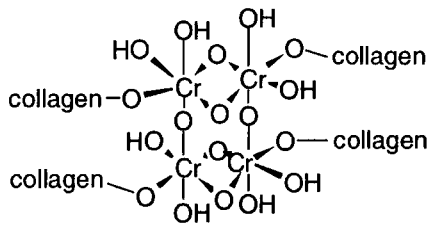

Figure 7.2 Cross-linking structure of two chromium(III) hydrolytic dimers[217]

The tanning procedure is optimised by a high concentration of chromium(III) ~ 0.1 mol L^{-1}, the solution containing hide matter and a high amount of chromium is expelled as waste. An online system for monitoring chromium(III) was needed for recycling tanning solution to improve efficiency and reach E.U. targets to reduce chromium release into the environment.

Speciation of chromium using capillary electrophoresis, CE, methods have been applied for processing electrolyte from plating baths,[218] wastewater from electro-plating plant,[218,205] and extracts from contaminated soil.[219] In these applications simultaneous detection of trivalent and hexavalent chromium was achieved with derivatisation of chromium(III) to anionic form with ligands such as cetyltrimethylammonium bromide (CDTA)[218], pyridinedicarboxylic acid (PDCA)[219], and diethylenetriaminepentacetic acid (DTPA),[205] with limits of detection in the μg L^{-1} range.[205] In this work, DTPA was used for speciation of chromium in leather tanning waste.

Capillary electrophoresis represents a separation method that is an alternative to the more expensive analytical techniques. Capillary electrophoretic separation and UV detection,[220,221] has been evaluated as an effective means for a simultaneous measurement of both chromium(III) and chromium(VI) in leather tanning waste.[193] In this chapter, voltammetric analysis was also investigated as a sensor format for monitoring of chromium(III) in tannery waste.

7.2 Chromium Speciation of Leather Tanning Waste by Capillary Electrophoresis

The leather tanning waste solution contains high amounts of soluble and insoluble protein material from hide as well as a high concentration of electrolyte described in Table 7.1. Solid phase extraction (SPE) was used to

separate insoluble material. The effect of this recovery method was investigated (Section 7.2.2).

Table 7.1 Elemental analysis by ICP-MS and ion chromatography of ions present in tannery sample ion chromatography

Ion	Concentration (mol dm^{-3})
Iron(III)	1.55×10^{-2}
Sodium	2.10×10^{-1}
Magnesium	5.25×10^{-2}
Calcium	1.29×10^{-2}
Potassium	6.95×10^{-4}
Chloride*	5.65×10^{-1}
Sulphate*	5.21×10^{-2}

Chromium(III) reacts with diethylenetriaminepentaacetic acid (DTPA) to form a stable anionic complex, $[CrDTPA]^{2-}$. Elution time of this complex was compared with CrO_4^{2-} as well as possible interferences from iron in the form of $[FeDTPA]^{2-}$. Sulfate and chloride anions were also tested for interference. Determination of total chromium by CE was in good agreement with other established techniques such as flame atomic absorption spectroscopy (FAAS), inductively coupled plasma-mass spectroscopy (ICP-MS) and UV/Vis spectroscopy (Section 7.2.3).

7.2.1 Chromium Speciation by CE

Preliminary experiments show the CrO_4^{2-} ion was detectable at 254nm, but trivalent $[CrDTPA]^{2-}$ complex was not detected. At 214nm both species were detected at the elution times of 3.8 mins and 5.9 mins respectively (Figure 7.3). All electropherograms had the following parameters: -15kV potential, 20sec injection time, 10 mins analysis time, 0.01 sensitivity, wavelength λ= 214nm. Other parameters were discussed earlier.

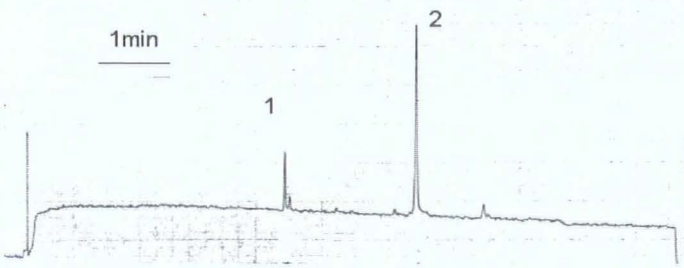

Figure 7.3 Electropherogram λ = 214nm, 1) 0.05 mmol L^{-1} CrO_4^{2-} at 3.8 mins 2) 0.05 mmol L^{-1} $[CrDTPA]^{2-}$ at 5.9 mins

The $[CrDTPA]^{2-}$ complex is very stable yet complexation was slow, and boiling for 5 mins was required to ensure complexation was complete. Figure 7.4.1 shows partial $[CrDTPA]^{2-}$ formation with other DTPA species (Figure 7.4.2 –5) also formed, in the absence of the boiling step. After 5 mins boiling, only fully complexed chromium(III) is seen in Figure 7.5-1. The free DTPA ligand had an elution time of 5.7min (Figure 7.5-2) Tests for optimum peak clarity showed that a two-fold excess of DTPA had a minimal disturbance from free DTPA at 5.7 min, while $[CrDTPA]^{2-}$ peak height remains at 55mm (Figure 7.6-1). Free DTPA is seen in Figure 7.7.

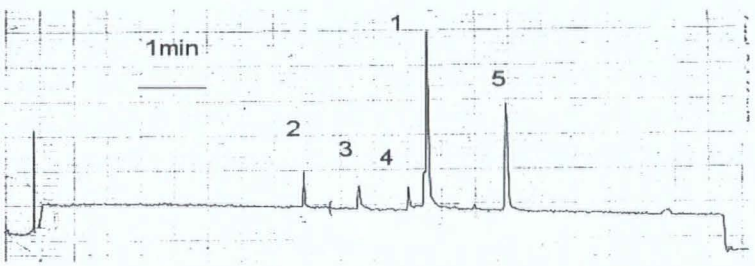

Figure 7.4 Electropherogram partially formed complex with $[Cr^{3+}]$ = 0.05mmol L^{-1} with 5-fold excess DTPA; no boiling 1) $[CrDTPA]^{2-}$ at 5.8 mins 2-5) LH and MLH species at 4.0, 4.8, 5.6, 5.7, 7.1 mins

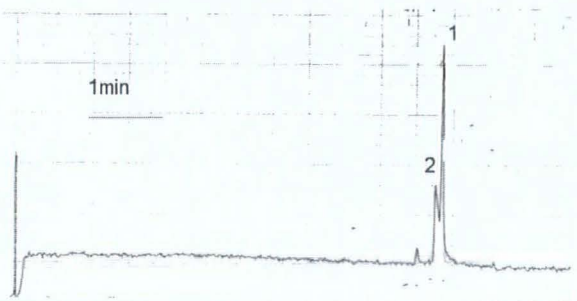

Figure 7.5 Electropherogram after 5mins boiling $[Cr^{3+}]$ = 0.05mmol L^{-1} 5-fold excess DTPA 1) $[CrDTPA]^{2-}$ at 5.9 mins 2) $DTPA^{5-}$ 5.7 mins

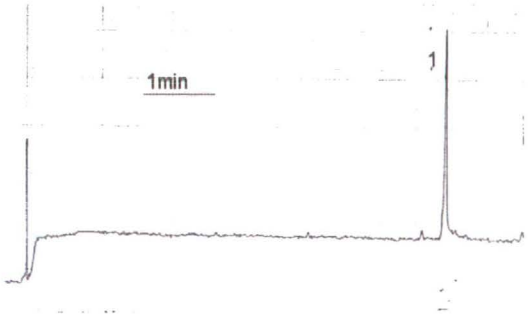

Figure 7.6 Electropherogram of 2-fold excess DTPA, $[Cr^{3+}]$ = 0.05mmol L^{-1} with 5 mins boiling 1) $[CrDTPA]^{2-}$ at 5.8 mins elution time

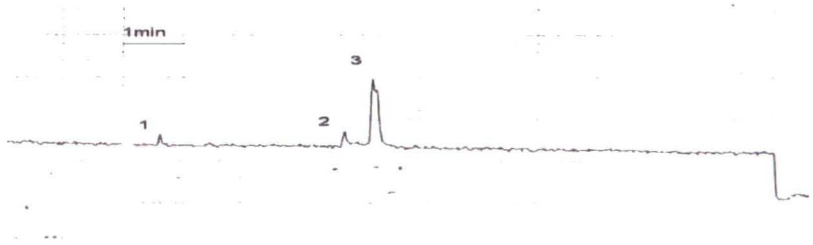

Figure 7.7 Electropherogram 0.25mmol L^{-1} DTPA, 1) - 3) DTPA species

7.2.1.1 CrO_4^{2-} and $[CrDTPA]^{2-}$ Calibration

The range of detection for the chromium ions was 5 µmol L^{-1} to 125 µmol L^{-1}. Calibration for combined CrO_4^{2-} and $[CrDTPA]^{2-}$ in the presence of 565 mmol L^{-1} chloride and 52 mmol L^{-1} sulphate, can be seen in Figure 7.8. The slope of the $[CrDTPA]^{2-}$ and CrO_4^{2-} calibration curves corresponded to 1.3 mm per µmol L^{-1} and 0.34 mm per µmol L^{-1} respectively.

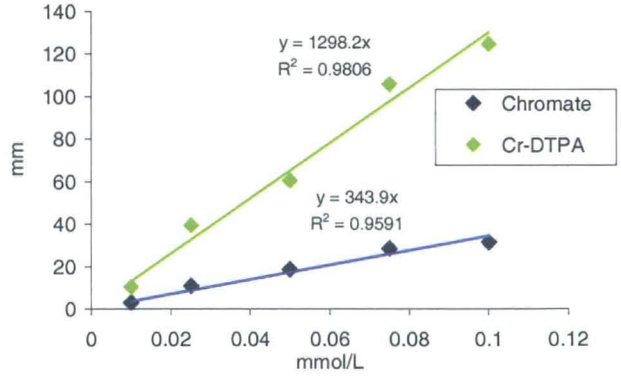

Figure 7.8 Calibration curve for CrO_4^{2-} and $[CrDTPA]^{2-}$

7.2.1.2 *Effect of $[FeDTPA]^{2-}$*

Tannery sample contains iron at about 10mmol L^{-1}. Iron(III) forms a strong complex with DTPA (K_{ML}= 27.8)[222], therefore elution time of $[FeDTPA]^{2-}$, and its effect on the chromium(III) complex was investigated. Figure 7.9 shows the separation of $[FeDTPA]^{2-}$ with elution time of 7.0min. As Table 7.2 indicates, there was no observed effect on chromium peak height.

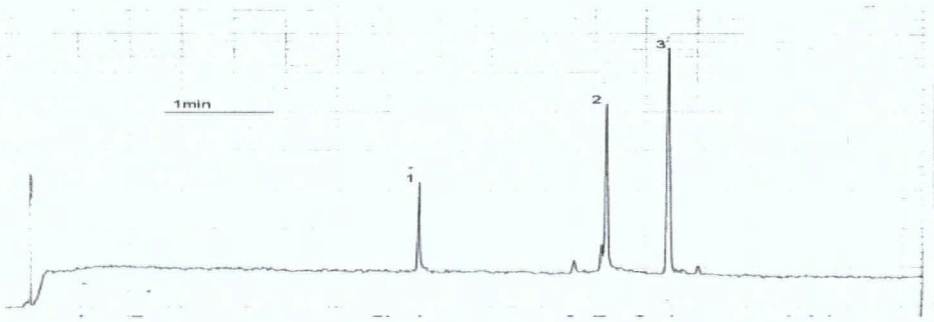

Figure 7.9 Electropherogram 1) 0.1 mmol L^{-1} CrO_4^{2-} at 3.75mins 2) 0.05 mmol L^{-1} $[CrDTPA]^{2-}$ at 5.8mins 3) 0.05 mmol L^{-1} $[FeDTPA]^{2-}$ at 7.0mins

7.2.1.3 *Effect of Sulfate and Chloride*

Other anions present in tannery sample included 52 mmol L^{-1} sulphate and 565 mmol L^{-1} chloride. Neither sulfate nor chloride ions neither gave any peak signal (Appendix I) nor had any effect on the elution time or peak height as seen in Table 7.2.

Table 7.2 Effect of sulfate, chloride and iron(III) on CE speciation of chromium

Sample composition	Cr(VI)		Cr(III)DTPA	
	t_m (min)	Peak height (mm)	t_m (min)	Peak height (mm)
0.05mM Cr(III) 0.1mM Cr(VI)	3.8	31	5.9	55
0.05mM Cr(III) 0.1mM Cr(VI) 0.56mM Cl^- 0.052mM SO_4^{2-}	3.75	29	5.85	54

0.05mM Cr(III) 0.1mM Cr(VI) 0.56mM Cl^- 0.052mM SO_4^{2-} 0.1mM Fe(III)	3.8	29	5.9	54

7.2.1.4 Chromium speciation by CE with $[CrPDCA]^{2-}$

Chromium(III) was derivatised with 2,6-PDCA. The result showed that the CrO_4^{2-} (peak 1) peak height was unaffected at 4.0 mins, but the $[Cr(PDCA)_2]^{2-}$ (peak 2) was much less defined at 6.1 mins than $[CrDTPA]^{2-}$ (Figure 7.10). Complex stability was reduced with PDCA (β_{ML2}= 7.06). It is likely that chromium(III) was coordinated in a number of mixed sulfate, chloride, or aquocomplexes that vary in elution time, and thus resulted in a less defined peak (Figure 7.10).

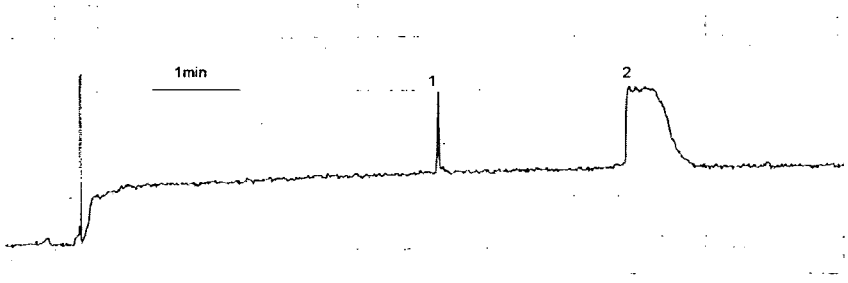

Figure 7.10 Electropherogram 1) 0.1 mmol L^{-1} CrO_4^{2-} at 4.0mins 2) 0.05 mmol L^{-1} $[CrPDCA]^{2-}$ 2-fold excess 26-PDCA at 6.1mins

Other chelating agents CDTA and EDTA have been used to chelate chromium(III) for capillary electrophoresis by others,[223,224,205] The singly charged complexes $[CrEDTA]^-$ and $[CrCDTA]^-$ were reported to result in slower elution time of over 10mins. $[CrEDTA]^-$ is also not completely separated from the iron(III) complex.[205]

7.2.2 Application of CE with Leather Tanning Waste

A tannery sample was first diluted 1000-fold, then solid phase extraction (SPE) was employed with micro-C_{18} columns to prevent adsorption of protein material on the capillary walls. Two procedures were compared; after dilution, one sample was passed through the C_{18} column prior to complexation with DTPA. The other sample was complexed firstly with DTPA then passed through the C_{18} column. The sample, that underwent SPE prior to complexation, had a reduction in signal corresponding to $[Cr^{+3}]$ = 14 mmol L^{-1} compared with post-complexation SPE of $[Cr^{+3}]$ = 17 mmol L^{-1} This indicated a loss of chromium in the solid phase extraction process. Further tests showed that without any solid phase extraction, recovery was higher with $[Cr^{+3}]$ = 21.5 mmol L^{-1}.

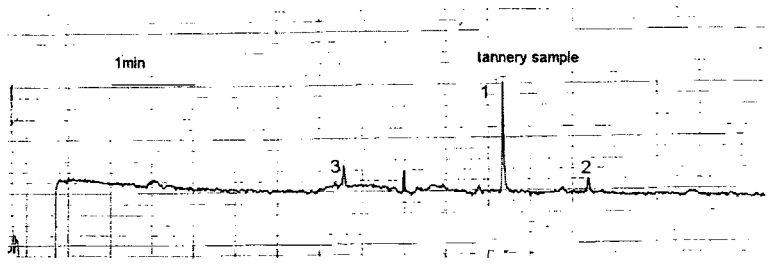

Figure 7.11 Electropherogram of tannery sample dilution x1000, SPE post-complexation, DTPA 0.1mmol L^{-1} 1) $[CrDTPA]^{2-}$ 2) $[FeDTPA]^{2-}$ 3) CrO_4^{2-}

The chromium(III) in the tannery sample with a pH of 5.0 was likely to have formed hydrolytic oligomers as well as being tightly bound with insoluble hide tissue. Both fractions were removed during SPE with a recovery of 14 mmol L^{-1}. However, when complexation took place first, the polymerized species reconfigured to form the $[CrDTPA]^{2-}$ complex with a recovery of 17 mmol L^{-1} (Table 7.3).

Table 7.3 Effect of sample preparation on recovery of chromium

Sample preparation	Chromium(III) concentration (mmol L^{-1})
SPE before complexation	14.0
SPE after complexation	17.0
Without SPE	21.5

The uncomplexed, 1000-fold diluted, tannery sample with SPE is seen in Figure 7.12. Without the presence of DTPA, no chromium(III) was detected, but the chromate peak remained.

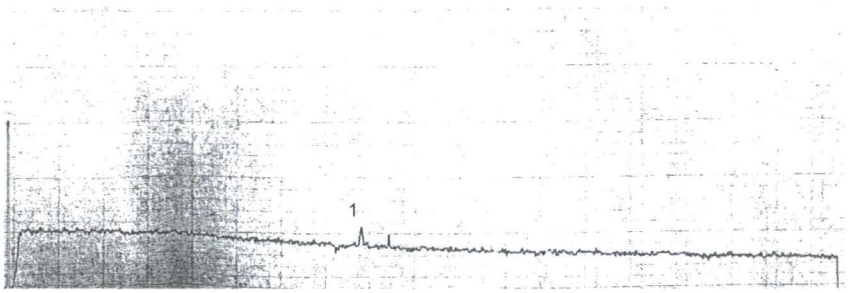

Figure 7.12 Electropherogram of tannery sample without DTPA complexation dilution x1000, SPE 1) CrO_4^{2-}

The raw sample in Figure 7.13 with no solid phase extraction, no dilution, and no complexation indicated CrO_4^{2-} = 0.18 mmol L^{-1}. The identity of the CrO_4^{2-} signal was confirmed with a spiked sample (Appendix II).

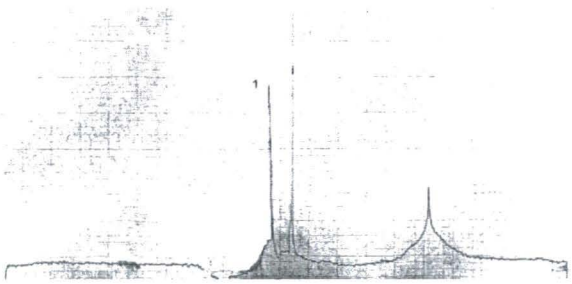

Figure 7.13 Electropherogram of tannery sample undiluted without complexation or SPE 1) CrO_4^{2-} at 4.6 mins, (Appendix II)

7.2.3 Spectroscopic and MS determination of Tannery Waste

At 421nm wavelength, the absorbance of a tannery sample was measured without prior preparation against a standard of chromium(III). At 421nm, the

absorbance from the tannery sample corresponded to a concentration of 21.6 mol L^{-1} (Figure 7.14). This was in good agreement with CE results.

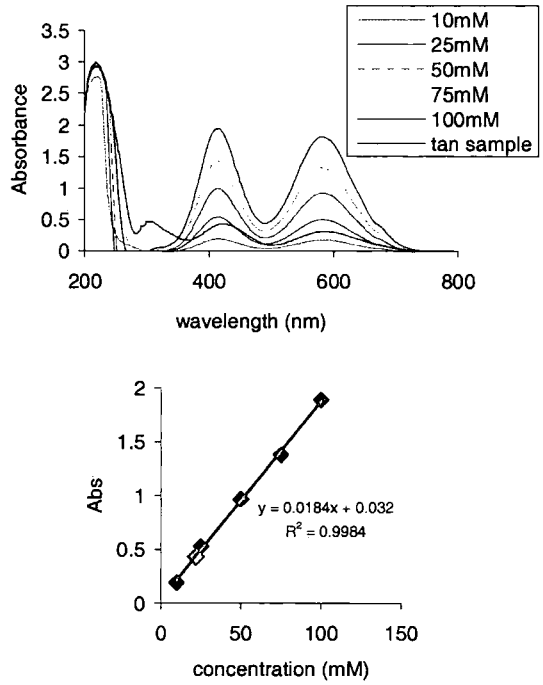

Figure 7.14 UV/Vis absorbance calibration for chromium(III)

FAAS and ICP-MS determinations were also in good agreement with CE and UV/visible absorbance measurements. However, there was a slight decline in concentration to 16 mmol L^{-1} and 19 mmol L^{-1}, respectively. Capillary electrophoresis was the only technique that enabled simultaneous chromium speciation.

Table 7.4 Results obtained by CE and other analytical methods for determination of chromium in leather tanning waste

Analytical method	Cr(III) Total Cr (mM)	Cr(VI)
CE	21.5	1.8
FAAS	19.0	
ICP-MS	16.0	
UV/Vis spectrophotometry at 421nm	21.6	

7.3 Voltammetric analysis of chromium(III)

Chromium(III) is a stable and rather electrochemically inert oxidation state. The d^3 electronic configuration tends to inhibit rapid ligand exchange and electron transfer kinetics are slow.[93] An oxidation potential of 1.38V for the Cr(III)/ Cr(VI) couple is found using a gold working electrode. However, the presence of chloride can interfere with differential pulse voltammetry (DPV) of chromium(III) and chromium(VI).

7.3.1.1 Voltage Window for Chromium Sensing

A high anodic voltage window was needed to allow examination of the Cr(III)/Cr(VI) couple at 1.38V. Figure 7.15 illustrates how gold is a suitable electrode substrate for sensing in the positive potential range in dilute sulfuric acid, compared with glassy carbon or platinum working electrodes.

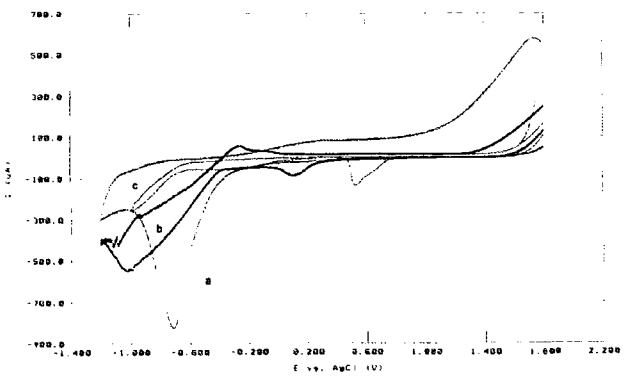

Figure 7.15 Cyclic voltammetry of voltage window (a) glassy carbon (b) platinum (c) gold electrodes in 10 mmol L^{-1} sulfuric acid 50 mVs^{-1}

The reductive current at 0.6V (Figure 7.15-c) occurred at the gold electrode in H_2SO_4 (aq). Background current in this region is associated with oxidation and reduction of oxides on the electrode surface.[109] Figure 7.16 shows the reductive current at 0.6V dissipated after multiple sweeps. Gold appeared to exhibit some of the required characteristics for analysis of chromium(III).

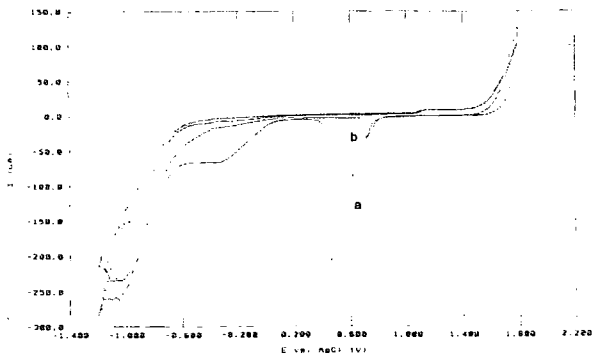

Figure 7.16 Cyclic voltammetry of 10 mmol L^{-1} sulfuric acid at gold electrode multiple sweep 50mVs^{-1} (a) scan 1 (b) scan 5 0.1 mol L^{-1} KCl

7.3.1.2 Effect of Chloride on Electroanalysis at a Gold Electrode

Preliminary results appeared to show good reductive differential pulse signals with a gold working electrodes in chromium(III) and chromium(VI) solutions. Inside the potential window, a highly positive peak was observed at 1.1V (Figure 7.17). This appeared to be reduction of chromium(VI) to chromium(III) after an oxidative cathodic stripping voltammetry (CSV) step. The signal at 0.42V may have corresponded to Cr(VI)/Cr(V) reduction (Figure 7.18).

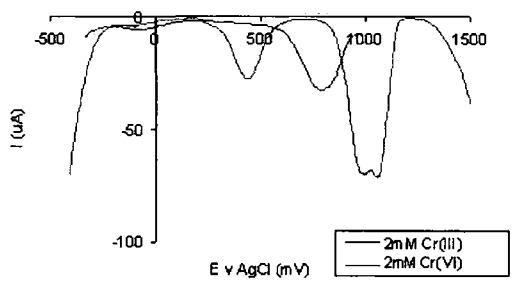

Figure 7.17 DP-CSV of chromium(III) and chromium(VI) solution pH 1.5 HCl 50mVs^{-1}

Further investigation showed that when using the gold electrode with chloride present in the background solution, a $[AuCl_4]^-$ complex was quickly formed. This species is also responsible for an oxidation peak at 1.1V peak (Figure 7.18).[225,226] Dissolution of the gold electrode occurs at potential above 1.1V in the presence of chloride.[225,226]

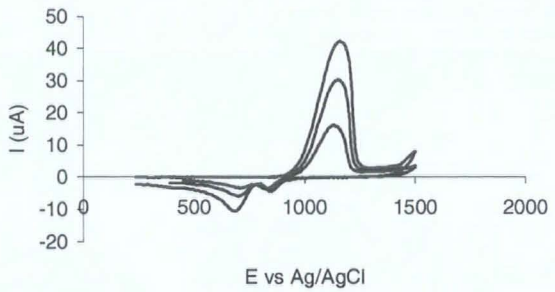

Figure 7.18 Adsorption of chloride on gold electrode, standard additions of 0.2, 0.4 and 0.6 mol L^{-1} HCl

7.3.1.3 Cyclic Voltammetry of Tannery Waste

Voltammetric interference from background ions present in tannery waste (Table 7.1) was not expected as indicated by reduction potentials (Fe^{3+}/Fe^{2+} =-0.44V).[227] The voltammetric behaviour of the anion background of chloride and sulphate was compared with tannery waste samples. The simulation and the actual tannery sample is seen below in Figure 7.19 and Figure 7.20 with a gold electrode. An electrochemical response from chromium(III) was not observed

.

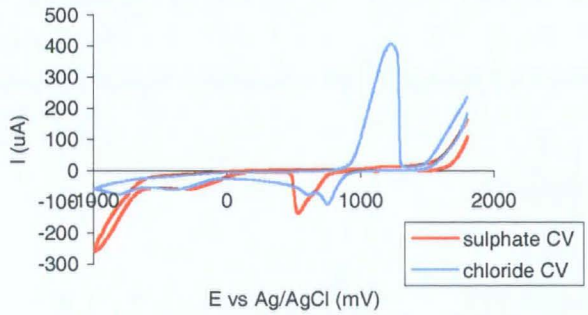

Figure 7.19 Cyclic voltammograms at a gold electrode of (a) sulphate 10mmol L^{-1}, (b) chloride 10mmol L^{-1} with 0.1 mol L^{-1} KNO_3 BGE

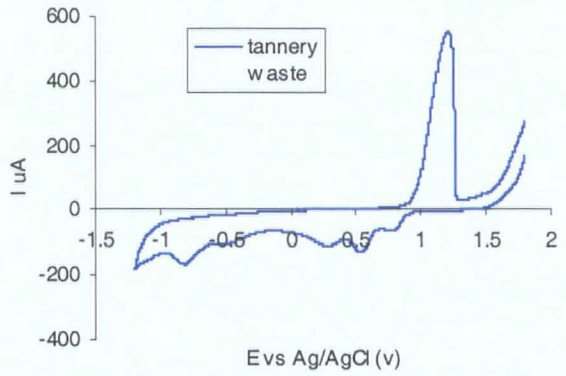

Figure 7.20 Cyclic Voltammogram of tannery waste 50 mV s^{-1}

Multiple cyclic voltammetry scans of tannery waste in Figure 7.21 show a reduction in cathodic peaks after 4 scans. Irreversible oxidation at 1.1V and reduction at 0.8V and 0.2V was attributed to $[AuCl_4]^-$ formation (Figure 7.18). The current dissipated as the electrode surface is passivated by the presence of chloride.

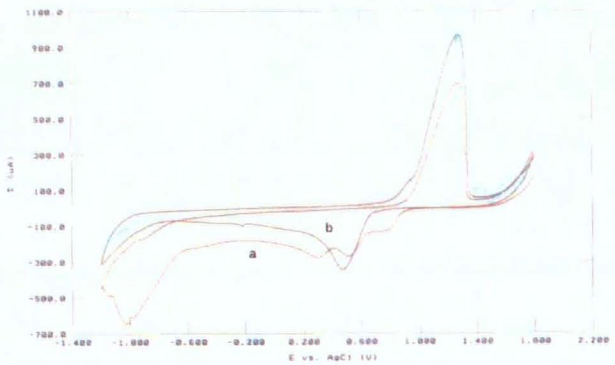

Figure 7.21 cyclic voltammetry of tannery waste multiple scans 50mV^{-1} (a) scan 1 (b) scan 4

Square-wave anodic and cathodic stripping voltammetry (SW-ASV and SW-CSV) provided increased sensitivity in analysis. Although both SW-ASV and SW-CSV, at a gold electrode, show very similar outcomes compared with cyclic voltammetry seen below in Figure 7.22. The increased signal output was seen with increasing conditioning time (Figure 7.23).

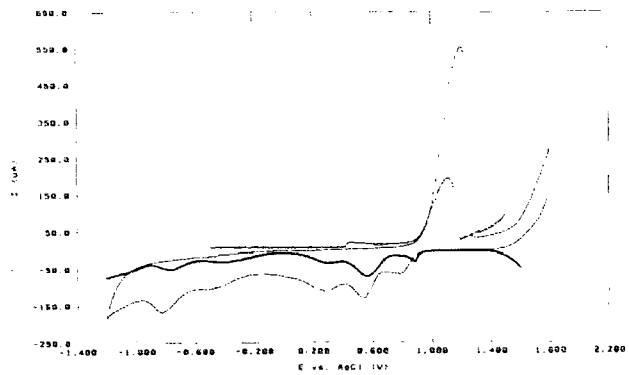

Figure 7.22 Voltammograms of tannery waste, conditions; gold electrode CV 50mVs^{-1}, SW-ASV and CSV pulse 3mV 5Hz increment 2mV

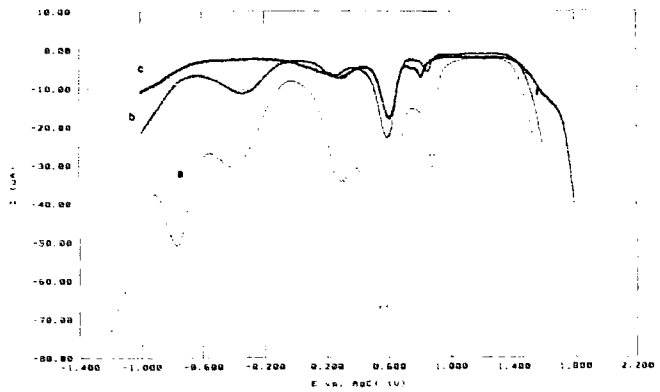

Figure 7.23 Successive SW-CSV runs 1.8V to –1.2V conditioning time (a) 4min, (b) 3 min (c) 2min at 2.0V

7.3.1.4 Cyclic Voltammetry of [Cr(PDCA)$_2$]

Chromium(III) can be made electroactive with binding to a ligand that forms an electroactive complex. An electroactive response for chromium(III) complex with 2,6-pyridinedicarboxylic acid (2,6PDCA) was investigated as a prospective ligand for chromium(III) sensing.

An oxidation was seen in Figure 7.24 at 0.28V and a smaller signal on the reductive scan at 0.12V. There was no interference from background current of 2,6PDCA (Figure 7.24). The $[Cr(26PDCA)_2]^-$ complex gave an electroactive response in pH 7.0 phosphate buffer within an hour, after this time the complex was not active electrochemically.

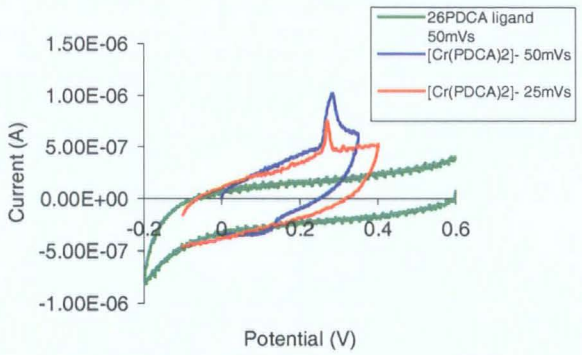

Figure 7.24 Cyclic voltammetry of free 26PDCA ligand and $[Cr(PDCA)_2]$ 1:2 mmol L^{-1} 50 mVs^{-1} and 25mVs^{-1} pH 7.0 phosphate buffer

The formation of chromium(III) hydrolytic polymer species occurred at pH values above 4.0,[228,229] but coordination with low stability organic ligands still occurred at higher pH values. This is exemplified in Figure 7.25 with 2,3PDCA $\beta_{ML2} = 4.45$ bound at pH 4.0 (violet colour) and neutral media at pH 7.0 (blue/green colour) compared with unbound Cr^{3+} in acidic pH 1.0 and neutral media (hydrolytic precipitation occurs prior to pH 7.0.

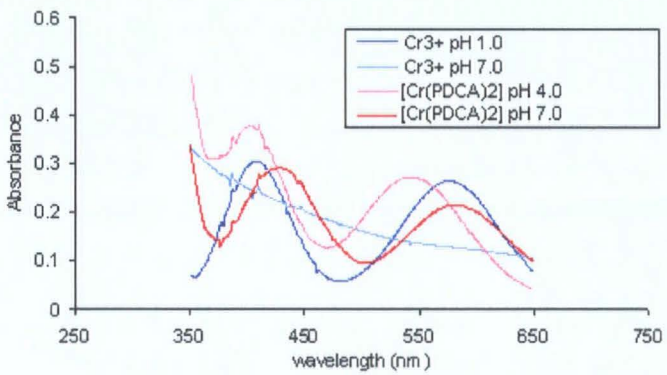

Figure 7.25 UV/Vis absorbance of free chromium(III) 5 mmol L^{-1} at pH 1 and 7, and $[Cr(PDCA)_2]^-$ complex at pH 4 and 7;

Complexation with chromium(III) was slow (Figure 7.26); equilibration with 2,6PDCA took several days. This exemplified the difficulty in speciation of chromium(III).

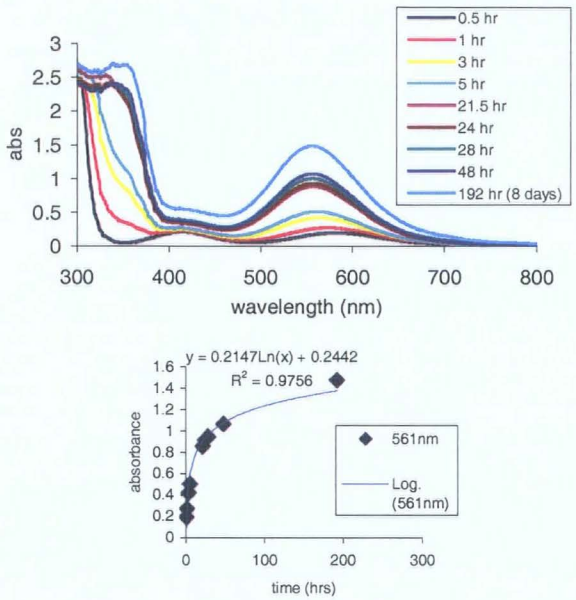

Figure 7.26 Rate of $[Cr(26PDCA)_2]^-$ complex formation UV/Vis absorbance 10 mmol L^{-1} PDCA

Voltammetry with a Cr26PDCA species gave an electroactive response at the early stages of complex formation. This was similar to the effect generated by partially formed $[CrDTPA]^{2-}$ complex described by Wang *et al.*[239]

Chapter 8

Miscellaneous Work

8 Miscellaneous Work

8.1 Diazonium Modification on Glassy Carbon; 4-Nitrobenzene Covalent Attachment on GCE

Modification of a graphite electrode (5mm diam x 50mm) involved electrolysis for 7mins at –0.6V in a 1 mmol L^{-1} solution of 4-nitrobenzenediazonium tetrafluoroborate in acetonitrile (ACN) with 0.1mol L^{-1} NEt_4ClO_4 background electrolyte. A broad irreversible cathodic peak was observed during the electrode modification, which dissipated after two cycles. This agreed well with the literature.[231] Diazonium reduction is illustrated in Figure 8.1 at a potential of 0.3V.[176]

Modification was confirmed by observation of nitrobenzene reversible redox at E^o= -1.20V after rinsing with deionised water and with ethanol in an ultra-sonic bath. (Figure 8.1).

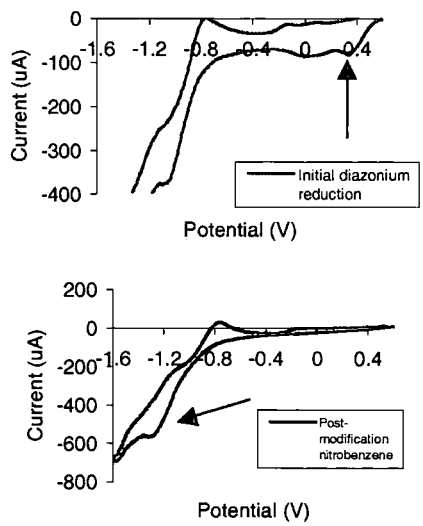

Figure 8.1 4-Nitrobenzene diazonium reduction and subsequent attachment at the graphite surface; conditions were 1mmol L^{-1} diazonium BF_4 solution in ACN with 0.1 ol L^{-1} NEt_4ClO_4, electrolysis time was 7mins at –0.6V

Initial grafting runs resulted in a reduction peak designated as the diazonium reduction that occurs during covalent attachment at the surface.[230] The two-step mechanism is described by Equation 8-1 and Equation 8-2.[231] Successful derivatisation of the carbon surface by electrochemical reduction of the diazonium group essentially depended on the aryl radicals not being oxidised at the same potential at which they are produced and thus react with the surface.[230]

Equation 8-1

$$Ar-N\equiv N^{+}+e^{-}\xrightarrow[E^{0}]{}Ar^{\bullet}+N_{2}$$

Equation 8-2

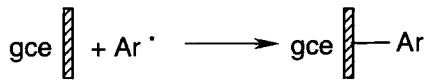

Reaction of the NO_2 group into NH_2 could be carried out in aqueous solution.[231] First, the electrode was derivatised by 4-nitrobenzene radicals in ACN. It was then transferred to a solution of 10% EtOH-water with 0.1mol L^{-1} NMe_4NO_3 background electrolyte. The cyclic voltammogram shows that the reaction became irreversible (Figure 8.2). This suggested a reduction of NO_2 to NH_2 occurred within the grafted layer of the nitrobenzene surface (Equation 8-3),[231] known to take place at a potential of –1.0V.

Equation 8-3

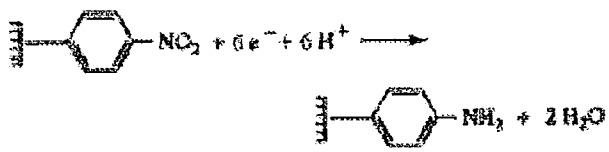

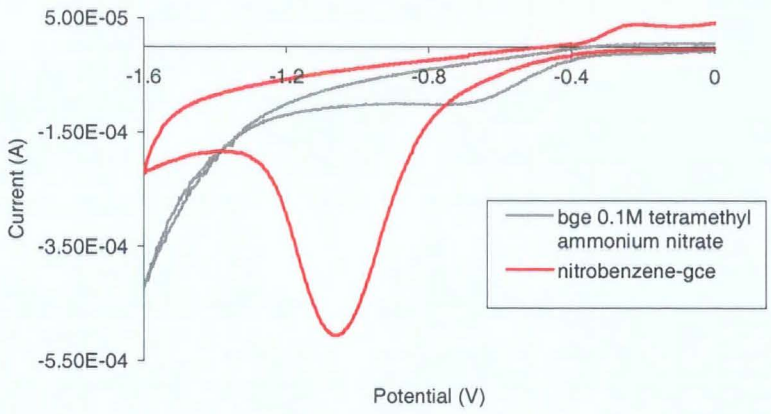

Figure 8.2 4-Nitrobenzene modified graphite in 0.1mol L^{-1} NMe_4NO_3 aqueous solution; 200mVs

The nitrobenzene compound was covalently bonded to a GCE with smaller surface area (3mm diam. carbon disc) using the method discussed earlier. The CV of the nitrobenzene-GCE did not indicate a clear reversible redox as expected at –1.2V (Figure 8.3). This could have been caused by the reversible wave in the background, indicating a small amount of water present in the sample. The presence of water is causes hydrogen evolution at –0.8V by the reaction; $H_3O^+ + e^- \rightleftharpoons ½H_2 + H_2O$.

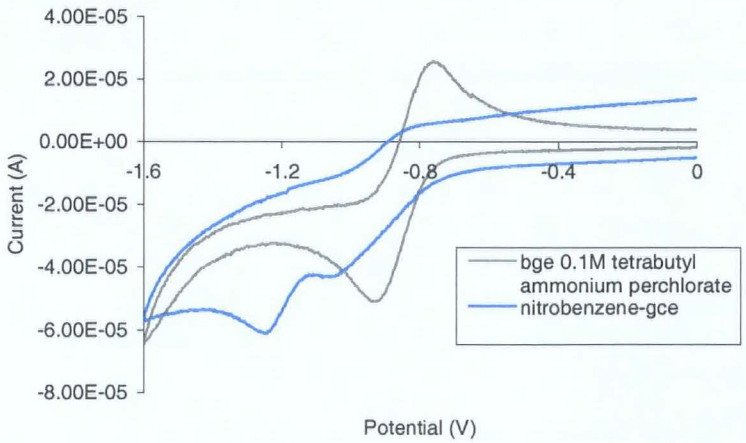

Figure 8.3 4-Nitrobenzene modification at glassy carbon in acetonitrile; 150 mV s^{-1}

However, the presence of the modified layer was again confirmed when the nitrobenzene-GCE was placed in aqueous solution containing 0.1mol L^{-1} NMe_4NO_3. This resulted in irreversible reduction, as previously described (Equation 8-3), at a potential of –0.96V.

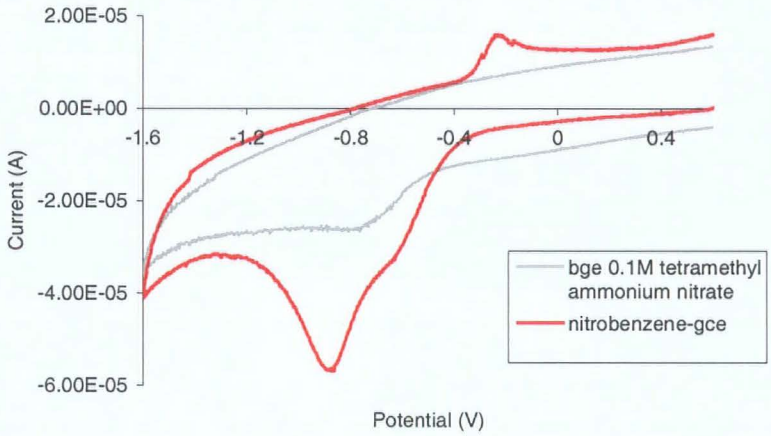

Figure 8.4 4-Nitrobenzene modified glassy carbon electrode in 0.1 mol L^{-1} NMe_4NO_3 aqueous solution; 150mV s^{-1}

The modification procedure was varied for optimization by measuring the response from nitrobenzene reduction at –1.0V. In this experiment, the concentration of diazonium solution was increased from 0.7mmol L^{-1} to 1mmol L^{-1}, and electrolysis time from 7mins to 10mins. All electrolysis was done at a potential of –0.6V.

The increase in concentration from 0.7mmol L^{-1} to 1mmol L^{-1} did not appear to have a significant effect, on nitrobenzene-GCE reduction peak (Figure 8.5a & c). The increase in electrolysis time from 7mins to 10mins did, however, appear to increase the surface coverage of nitrobenzene, based on the increase of the nitrobenzene reduction current in Figure 8.5a & b.

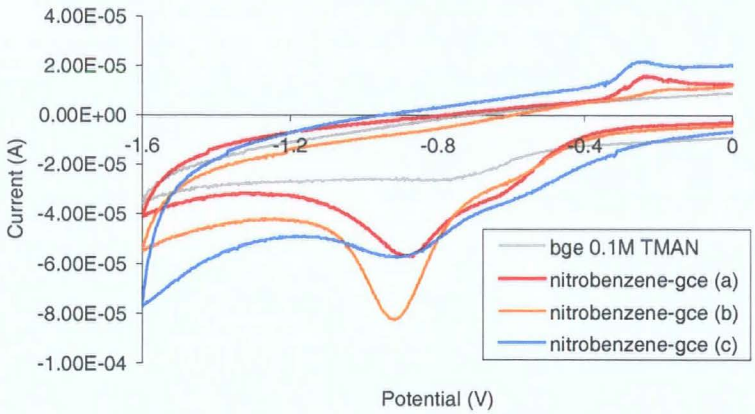

Figure 8.5 Evaluation of three GCEs' CVs at 150mV s^{-1} in 0.1 mol L^{-1} NMe_4NO_3 aqueous solution, modified with the following conditions; (a) 0.7mmol L^{-1} diazonium solution, 7min electrolysis at –0.6V (b) 1mmol L^{-1} diazonium solution, 10min electrolysis at –0.6V and (c) 1mmol L^{-1} diazonium solution, 7 mins electrolysis at –0.6V. Electrodes were modified in ACN with 0.1mol L^{-1} NBu_4ClO_4

Covalent attachment via the diazonium linkage is a readily accessible route for electrode modification. As described above, glassy carbon electrodes are easily modified and the surface monolayer can be regulated through selection of an appropriate concentration of diazonium salt, and electrolysis time and potential. The electrode is very stable; physical abrasion is necessary to restore the glassy carbon surface.[176]

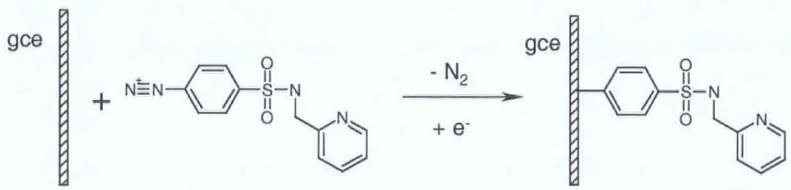

Figure 8.6 Reaction scheme for covalent attachment of ligand L^1 to gce surface via diazonium linkage

Further work could involve the derivatisation of glassy carbon surfaces with selectively binding ligands, such as the previously studied ligand, L^1. A reaction scheme is described above in Figure 8.6. It is expected that the electron donating character of the ligand would be altered when bound to a

GCE. In the case of L^1 (or L^4), a slightly greater acidity of the ligand may actually improve complex stability of copper(II) and zinc(II).

8.2 Electro-polymerisation of Pyrogallol on GCE

A glassy carbon electrode was prepared in the manner described earlier, and derivatised with pyrogallol by cyclic voltammetry between –0.1V and 1.5V for 10 cycles at a scan rate of 20mV s^{-1}. The first and last scans are illustrated below in Figure 8.7. An irreversible oxidation wave at 0.5V steadily diminished at each cycle until the electrode was passivated. This was consistent with the formation of an insoluble polymer film on the electrode surface.[232,233]

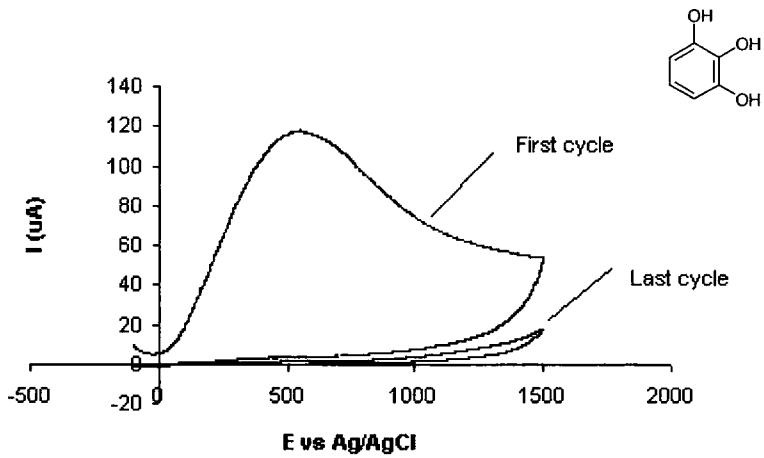

Figure 8.7 CV of first and last scan of electro-polymerisation of pyrogallol at the GCE surface

The poly(pyrogallol)-GCE was immersed in a stirred accumulation solution, buffered at pH 5.5, for 3mins at open circuit containing spiked levels of antimony(III). The electrode was then transferred to an antimony-free stripping solution of 1mol L^{-1} HCl 0.1mol L^{-1} KCl. The stripping procedure involved a 30s preconcentration step at –0.4V and a 10mV s^{-1} from –0.4V to 0.3V. The concentration range available under optimal conditions was from 10^{-5} mol L^{-1} to 10^{-8} mol L^{-1}. Spiked samples of antimony(III) with concentrations 10^{-5} to 10^{-7} mol L^{-1} are seen below in Figure 8.8.

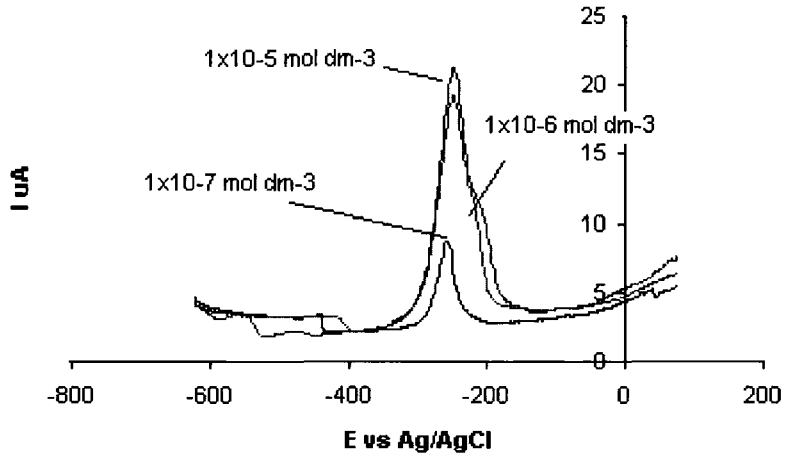

Figure 8.8 SW-ASV of poly(pyrogallol)-gce after 3min accumulation in antimony(III) solution. Stripping solution contained 1mol L^{-1} HCl

8.3 Investigation of Suitable Ligands for Chromium(III) Voltammetric Analysis

Chromium(III) is classified as a hard Lewis acid because of its +3 charge. It is expected to bind well with hard Lewis bases such as carboxylate oxygen and nitrogen donor atoms. Diethylenetriaminepentaacetic acid (DTPA) for example forms a 1:1 complex with chromium(III) with log K_1 = 22.01.[206] A weaker complexone was sought for a potential adsorptive metal ion sensor surface to impart reversibility; a stability with β of 5 - 9 may be ideal. Intermediate stability was investigated with ligands containing mixtures of oxygen and nitrogen donors, listed in Figure 8.9.

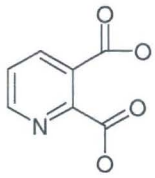

2,3-pyridinedicarboxylic acid

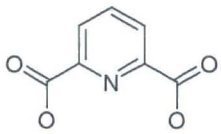

2,6-pyridinedicarboxylic acid

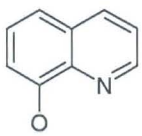

8-hydroxyquinoline

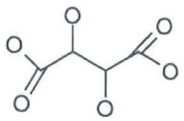

DL-tartaric acid

Figure 8.9 Prospective ligands for trivalent chromium analysis

8.3.1 Protonation Equilibrium Determinations for Chromium(III) Ligands

8.3.1.1 2,3-Pyridinedicarboxylic Acid Protonation Equilibria

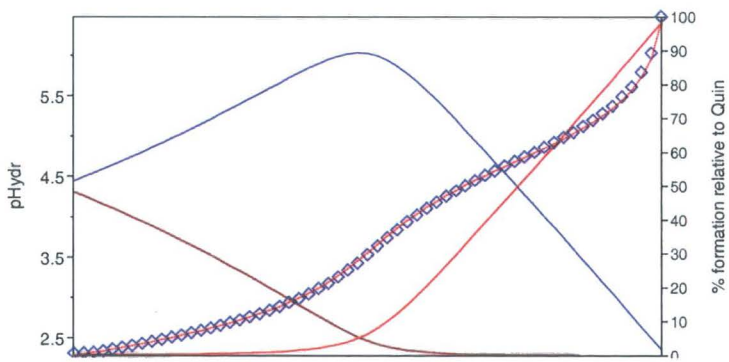

Figure 8.10 2,3-PDCA protonation equilibrium titration

Protonation constants for 2,3-pyridinedicarboxylic acid were measured in 0.1 mol L^{-1} KCl titrated against 0.1 mol L^{-1} NaOH at 25°C. Refined values (Figure 8.10) were log $K_1 = 4.69$ and $\beta_2 = 6.95$ ($Chi^2 = 21.23$ and $\sigma = 2.41$). These compared well with reported values of log $K_1 = 4.71$ and $\beta_2 = 7.08$ (0.1 mol L^{-1} KNO_3 25°C).[234]

8.3.1.2 2,6-Pyridinedicarboxylic Acid Protonation Equilibria

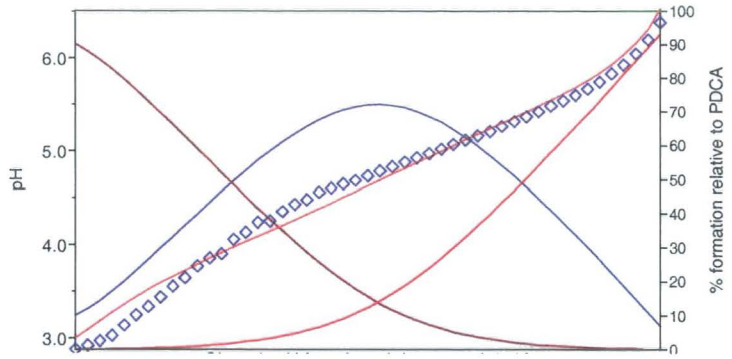

Figure 8.11 2,6-PDCA protonation equilibrium titration

Titration data for 2,6-pyridinedicarboxylic, seen in Figure 8.11, did not yield protonation constants with high confidence log $K_1 = 5.39$ and $\beta_2 = 9.35$ ($Chi^2 = 16.14$ and $\sigma = 14.68$). Reported value were log $K_1 = 4.76$ and $\beta_2 = 6.91$ (0.1 mol L^{-1} $NaNO_3$ 25°C).[235]

8.3.1.3 DL-Tartaric Acid Protonation Equilibria

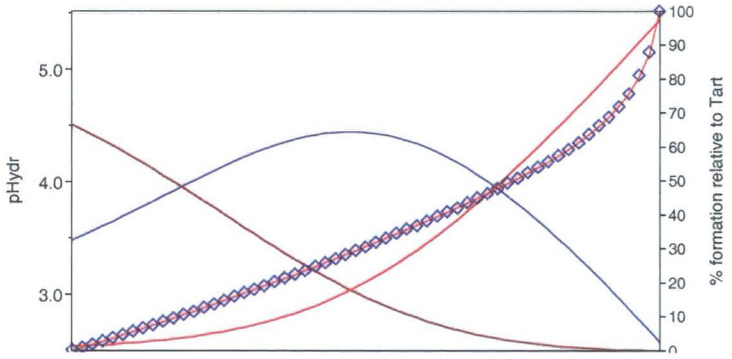

Figure 8.12 DL-Tartaric acid protonation equilibrium titration

At a concentration of 10 mmol L^{-1} tartaric acid in 0.1 mol L^{-1} KCl against 0.1 mol L^{-1} NaOH (aq), protonation constants were log $K_1 = 3.93$ and $\beta_2 = 6.7$ ($Chi^2 = 8.93$ and $\sigma = 1.82$) (Figure 8.12). These compared well with reported values log $K_1 = 3.97$ and $\beta_2 = 6.84$ (glass electrode 25°C 0.1 mol L^{-1} KNO_3).[236]

8.3.1.4 8-Hydroxyquinoline Protonation Equilibria

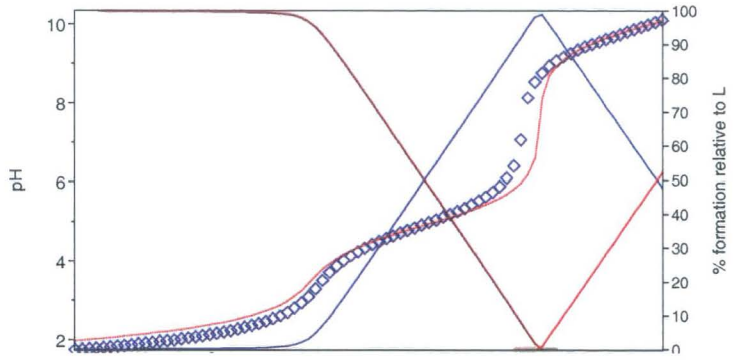

Figure 8.13 8-hydroxyquinoline protonation equilibrium titration

The protonation constants for 8-hydroxyquinoline were not refined to an actual value but the log K_1 and β_2 were found to be in the 9.5 and 14.9 range, respectively (Figure 8.13). This agreed with reported values of log K_1 = 10.00 and $\beta_2 = 15.12$.[237]

8.3.2 Chromium(III) Formation Constant Equilibria

8.3.2.1 [Cr(2,3-PDCA)$_2$]

A Cr^{3+}/ 2,3-PDCA model at 5 and 10 mmol L^{-1} gave values of log $K_{ML} \approx 2$ and $\beta_{ML_2} \approx 4.45$ but could not be refined with any precision due to unstable complex formation before hydrolysis began. The ML curve in orange (Figure 8.14) illustrates the low concentration of the species.

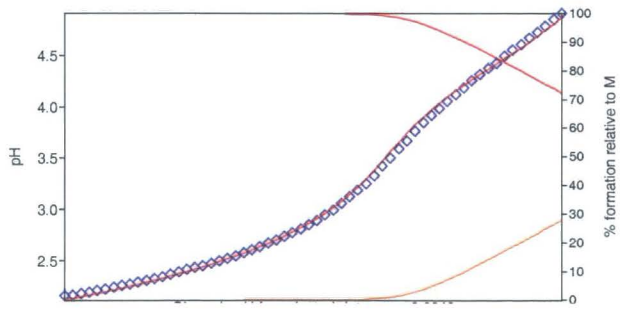

Figure 8.14 Refinement of ML species 2,3-PDCA/Cr^{3+} 5:10 mmol L^{-1} titration

8.3.2.2 [Cr(2,6-PDCA)$_2$]

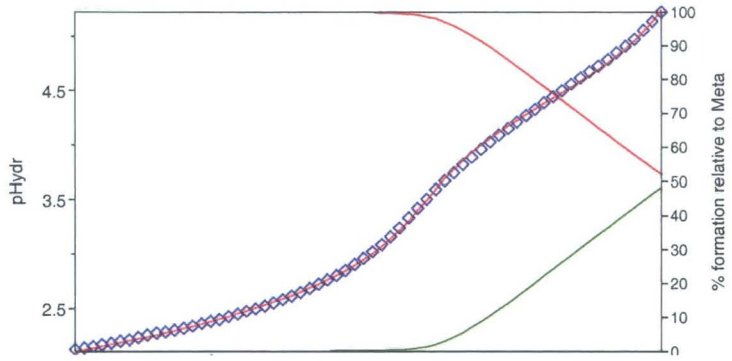

Figure 8.15 Refinement of ML species 2,6-PDCA/ Cr^{3+} 5:10 mmol L^{-1} titration

Titration data was refined in the lower portion of the pH range before any precipitation occurred (Figure 8.15). Formation constant log $K_{ML} \approx 1.5$ and was too low to be refined, $\beta_2 = 5.00$ ($Chi^2 = 5.76$ and $\sigma = 3.21$). Reported values were $\beta_2 = 5.15$ (0.5 mol L^{-1} $NaClO_4$ 25°C spec).[238]

Chapter 9

Discussion

9 Discussion

In the previous study by Aileen Congreve,[59] preferred ligands were chosen according to attributes desired for a lanthanide complex-based luminescent sensor for zinc(II). Ligands L^1 - L^4 were also evaluated for possible use as an immobilized selective surface layer for a metal ion voltammetric sensor. Predictions about metal speciation made with *HySS* software[211] were tested using voltammetric and spectrophotometric titration.

Protonation Equilibria

Basicity of the sulfonamide ligands was altered mainly by the increase in polarity from the trifluoromethyl sulfonamide group. This increase was from a log K_1 of 7.50 to a more basic tolyl sulfonamide log K_1 of 12.15. There was also a slight increase in the basicity of the pyridyl nitrogen from the α-methyl group. The L^4 log K_2 increased to 3.95 from 3.27 for L^1, and the L^3 log K_2 increased to 3.33 from 2.67 for L^2.

The trends observed between tolyl and trifluoromethyl sulfonamide ligands as well as the effect observed by the addition of the methyl group on L^3 and L^4 correlated closely with sulfonamido quinoline ligands previously reported by Nakamura *et al.*[90] Table 2.1 listed the available data on tosyl ligands TSQ, and trifluoromethyl ligands CF_3SQ and 2-Me-CF_3SQ. This showed that the pyridyl ligands were slightly more basic than the quinoline derivatives caused by the higher acidity of protonated quinoline with log K_2 of about 2 instead of 3.3. The log K_1 sulfonamide deprotonations, however, were very similar with values of 11.9, 7.6 and 8.2 for TSQ, CF_3SQ and 2-Me-CF_3SQ compared with 12.15, 7.50 and 7.58 for the respective pyridyl ligands.

Ligands L^2 and L^3 were deprotonated at lower acidities, which enabled ML_2 coordination at lower pH. However, the altered electron donating ability of the sulfonamide nitrogen made the ligand a harder Lewis base, and therefore, relatively less stable with intermediate Lewis acids, whereas ligands L^1 and L^4 were more basic. This made stability with late 3d transitions metals higher. Although LH species remain dominant throughout the mid-pH range, ML_2 formation begins at a higher pH, and therefore is in greater competition with OH, especially when $[L_T]$ is small.

Complex Equilibria

The α-methyl groups on L^3 and L^4 affected the natural order of stability of metal ions according to the Irving – Williams theory, primarily by altering the coordination geometry of copper(II) and nickel(II) complexes. Zinc(II) complexes $[ZnL^3_2]$ and $[ZnL^4_2]$ were unaffected by the steric control, which approached the stability of the copper(II) complex. Speciation models indicated, in Section 5.3.2.9 (p.95), that zinc(II) retained an ML_2 speciation at lower $[L_T^4]$ than does copper(II). It appeared that this increases the selectivity of L^4 for zinc(II) over copper(II) at ambient pH (Figure 5.36 p.97).

Trends in formation constant equilibria between transition metals cobalt(II), nickel(II), copper(II) and zinc(II) with L^1 and L^4 ligands followed the same trends as those described by Nakamura with sulfamidoquinoline ligands (Table 2.1 p.20). Ligand L^1 as well as 8-(4-toluenesulfonamide)quinoline (TSQ), follow the Irving-Williams stability trend with the highest stability at copper(II) followed by nickel(II), zinc(II) and cobalt(II). The TSQ ligand has enhanced stability relative to L^1 complexes; with β_{ML2} $[Cu(TSQ)_2]$= 25.3[90] and $[Zn(TSQ)_2]$= 19.8[90] compared to analogous L^1 complexes β_{ML2}= 20.50 and 15.03 (Table 5-11 p.96).

Zinc(II) stability in both L^3 and L^4 complexes were enhanced compared with L^2 and L^1 counterparts, with β_{ML2} of $[ZnL^3_2]$ = 11.50, which increased from 10.21, and β_{ML2} of $[ZnL^4_2]$ = 16.84, which increased from 15.03. This effect was also observed with $[Zn(CF_3SQ)_2]$ and $[Zn(2\text{-Me-}CF_3SQ)_2]$, where stability increased from β_{ML2} = 14.0 to 15.7.[90]

The opposite effect was observed with copper(II) and nickel(II) L^3 and L^4 complexes, in comparison to L^2 and L^1 complexes. In both cases stability was reduced, with β_{ML2} $[CuL^3_2]$ = 12.46 decreasing from 13.28, and β_{ML2} $[CuL^4_2]$ = 18.75 decreasing from 20.50. The β_{ML2} of $[NiL^4_2]$ also decreased from 15.28 to 13.08. Data were not available for the complex $[Cu(2\text{-Me-}CF_3SQ)_2]$, however, the effect of the methyl group on nickel(II) complex stability indicated a decrease in stability from 16.0 to 11.8 for the respective equilibrium (Table 2.1 p.20).

Speciation models described an increase in the formation of $[ZnL^4_2]$ compared with $[CuL^4_2]$ (Figure 5.35 p.97). Species distribution models were used to illustrate how, at $[L_T] \approx 2$mmol L^{-1}, there was a pronounced decline in $[ML_2]$ that occurs with L^1 and L^4 equilibria. Competitive models between copper(II) and zinc(II) with L^4 showed how $[ZnL^4_2]$ formation is favoured over copper(II) (even though β_{ML2} of $CuL^4_2 > ZnL^4_2$).

Competition models between CuL^2_2 and CuL^1_2 with $[Cu^{2+}]$ = 1μmol L^{-1} illustrated how the two ligands dominate at higher $[L_T]$ (>2 mmol L^{-1}), with L^2 coordinating more at mid-pH range, and L^1 coordinating more in the alkaline pH range (Figure 5.51 p.106). At $[L_T] < 2$ mmol L^{-1}, species distribution models indicated a large reduction in $[CuL^1_2]$, while $[CuL^2_2]$ remained high at ambient pH. This was despite the large respective difference in stability (β_{ML2}= 20.50 and 13.28).

Fluorescent Zinc(II) Probe

A central aim of the previous work by Aileen Congreve[59] to develop a selective fluorescent zinc(II) probe was to a identify a ligand that bound to zinc(II) at physiological pH, and was able to complex zinc(II) at very low concentration.[59] Analysis of pyridyl sulfonamide complex speciation indicated that, although binding strength was lower with ZnL^2_2 and ZnL^3_2, the $[ML_2]$ was high at physiological pH, and persisted when $[L_T]$ was very low (Figure 5.50 p.105).

The outcome of the study was that although trifluoromethyl L^2 and L^3 exhibited an affinity for zinc(II) binding, the pyridyl trifluoromethyl sulfonamide-appended lanthanide complexes did not show significant behaviour that was responsive to zinc(II) in the range investigated. [59] It was concluded that a zinc(II) binding group with a higher affinity at physiological pH must be sought. [59]

The trifluoromethyl sulfonamide ligands deprotonate at lower pH, and thus were available to bind with metal ions, but did not possess a high enough affinity for zinc(II). The tosyl sulfonamides had a much higher affinity for zinc(II), but were not available for binding at low enough pH.

Metal Ion Voltammetric Speciation with Acid-Base Titration

The species distribution models of metal ion equilibria facilitated the evaluation of voltammetric and spectrophotometric speciation titrations. Factors, such as $[M_T]$, $[L_T]$, $[H_T]$, scan rate, de-aeration, conditioning time, conditioning potential, and reversibility, were evaluated. Copper(II) / L^1 solution equilibria provided a convenient test case for voltammetric speciation because the reactions generated at the electrode were reversible. Other metal ion / ligand solutions investigated showed varied results, depending on their reversibility and the nature of the complex studied.

Copper(II) species Cu^{2+} and CuL^1_2 had redox reactions that occurred at separated potentials, $E_{½}$ = 0.2V and –0.34V. The increasingly negative electrode potential reflects the increased stability of CuL^1_2. The extent of E_p separation between ML_2 and free M^{2+} species reflected the thermodynamic stability of the complex. Redox potentials of copper(II) complexes increase in negativity in the order $CuL^3_2 < CuL^2_2 < CuL^4_2 < CuL^1_2$ ($E_{½}$ = 0.055V,[59] -0.14V,[59] -0.21V, and -0.34V). This coincided with the order of stability; β_{ML2} = 12.46, 13.28, 18.75, and 20.50.

In relation to the ML^+ species, models indicated that $[ML^+]$ was maximised (74%) when $[L_T^1] \approx$ 2mmol L^{-1} with a pH of 5.5. Cyclic voltammetry under these conditions confirmed the predominance of the ML^+ species, with oxidation at – 0.08V, which was clearly separated from the other species (Figure 6.21 p.122). Individual detection of ML^+ species was also observed with standard addition of copper(II) at $[L_T^1]$ = 10 mmol L^{-1} at pH 4.05 (Figure 6.20 p.122). The correlation between the model and voltammetric responses could be useful for predicting metal ion behaviour at modified electrode surfaces.

Targeted sensing of copper(II) through adsorptive binding with sulfonamide ligand L^1 may be best served with ML^+ signal at pH 4 - 5. Species distribution models have indicated that ML^+ persisted, more than ML_2, when $[L_T]$ is small. The basic deprotonation of pK_{a2} for L^1 leads to early formation of ML^+.

Simultaneous Potentiometric, Voltammetric and Spectrophotometric Acid-Base Titrations

A voltammetric and spectrophotometric pH titration method was developed to allow formation constant determination with either current response or U.V. / visible absorbance data. Differential pulse, cyclic voltammetry and absorbance measurements were taken simultaneously in a 10 ml flow-cell,

while the pH was adjusted incrementally by computer at a fixed [M]:[L] ratio.

The voltammetric pH titration for $[CuL^1_2]$ and $[CuL^4_2]$ allowed attempts to be made at calculating the 'virtual' potential from the $[M]_{free}$ labile current peaks. Although the [L]:[M] ratio needed to be higher with labile systems to obtain a well-defined free metal current, it is believed that the apparatus would certainly be capable of producing reliable formation constants with voltammetry at a GCE, by refinement by potentiometric dedicated software.

Most importantly, however, is the contribution that a reliable voltammetric formation constant evaluation method, as defined by Cukrowski, would bring to ongoing efforts for establishing accurate parameters of the labile part of metal systems involved in the metal ion bio-uptake of organisms.

Chromium Speciation

The leather tanning industry uses characteristics, such as hydrolytic polymerization and slow kinetics of chromium(III), in order to toughen and preserve leather hide. Reliable in-situ chromium(III) monitoring was sought to improve process efficiency of the tanning process and reduce environmental output of chromium.

Voltammetric sensing of chromium(III) is challenging, since it is often electro-inactive due to slow homogeneous kinetics. Use of a gold working electrode for the analysis of chromium in tanning waste was complicated by oxidative processes involving the production of $[AuCl_4]^{2-}$ at the gold surface at high potential. At a glassy carbon electrode, however, an oxidation signal was obtained for a Cr^{3+} / 2,6-PDCA solution, at E_p = 0.28V. The $[Cr(2,6\text{-}PDCA)_2]^-$ complex equilibrates over many days, therefore the electroactive response observed was likely related to a partially formed complex species.

Examination of chromium speciation in leather tanning waste solution by capillary electrophoresis with U.V. detection was very compatible with the sampling conditions. High concentration of chromium in tannery waste was suitable for U.V. detection, and the derivatisation procedure presented in Section 7.2.1 effectively converted chromium(III) to a stable anionic complex with a separated elution time from interferences of CrO_4^{2-} and $[FeDTPA]^{2-}$. Speciation capability enabled simultaneous determination of anionic CrO_4^{2-} and cationic Cr^{3+} species. The CE-UV procedure detected 0.18 mmol L^{-1} CrO_4^-. This is at a level that could impact the local environment.

A drawback of the CE-UV method was the time-consuming derivatisation step for $[CrDTPA]^{2-}$ formation. By coupling the electrophoretic method, outlined here, with a flow injection procedure, described by Wang[239] (which quickly formed a partial chromium(III)-DTPA complex) could be a fast and cheap means of chromium speciation for the leather tanning industry.

The importance of metal speciation is clear in environmental terms, and there has been an increased need for reliable methods of quantifying different metal species. Speciation of trace metals was investigated voltammetrically in the aim of establishing a methodology for combining chemical modification of electrodes as a means for analyte preconcentration, and the measurement of an electrochemical signal related to the labile fraction of a trace metal present in solution. The use of 'virtual' potentiometry, described by Cukrowski, provides a methodology for both modeling of species equilibria of the metal – immobilized ligand, and the determination of the lability of the metal ion. Here, a range of ligands were evaluated with species distribution models to obtain the optimum characteristics of a ligand for a chosen analyte. These models were then tested with voltammetry and were found to be in good agreement.

9.1 Future Work

Further investigation is needed for development of an automated flow injected chromium speciation analysis system with CE separation and voltammetric or U.V. detection.

A pyridyl sulfonamide ligand immobilized on a glassy carbon surface via diazonium linkage could be used to investigate possible sensor formats for copper(II) and zinc(II). A modified layer with an affinity for zinc(II) would avoid troublesome electrode surface adsorption at a bare glassy carbon surface.

Further voltammetric titrations at optimum concentrations and conditions, and subsequent formation constant analysis, would allow further insight into the development of in situ electrochemical sensors for metal ions in the environment. This study has shown that there is an important role in the use of voltammetric acid-base titrations for investigations of metal speciation in solution.

Appendix

Appendix I Electropherograms

Scale = 1square = 1cm = 30 secs

#1 chromate 254nm

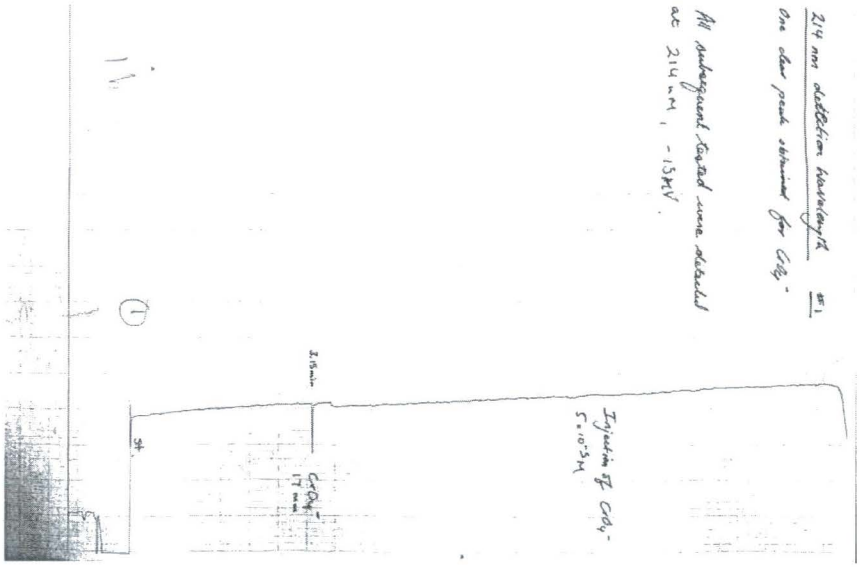

#9 sulphate background

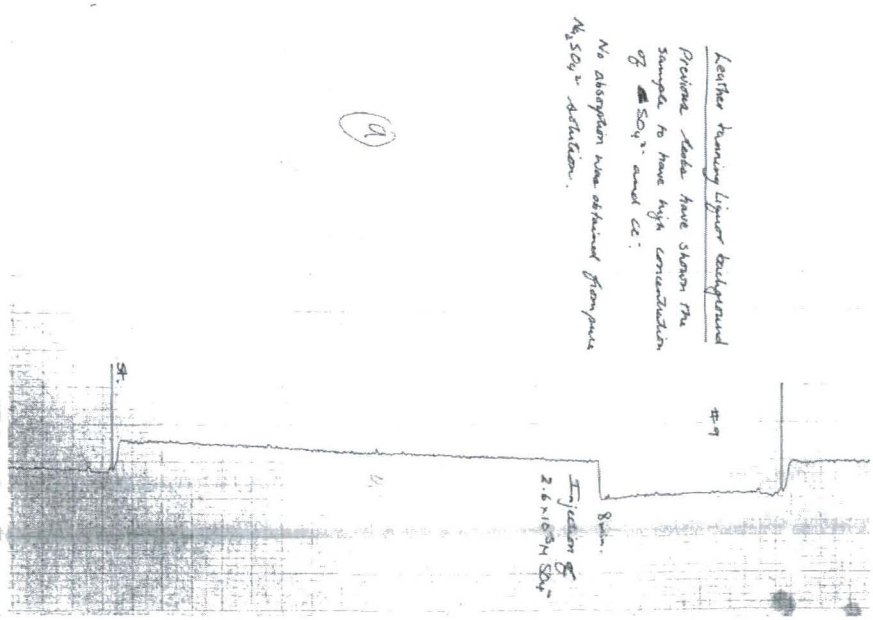

#12 chloride background

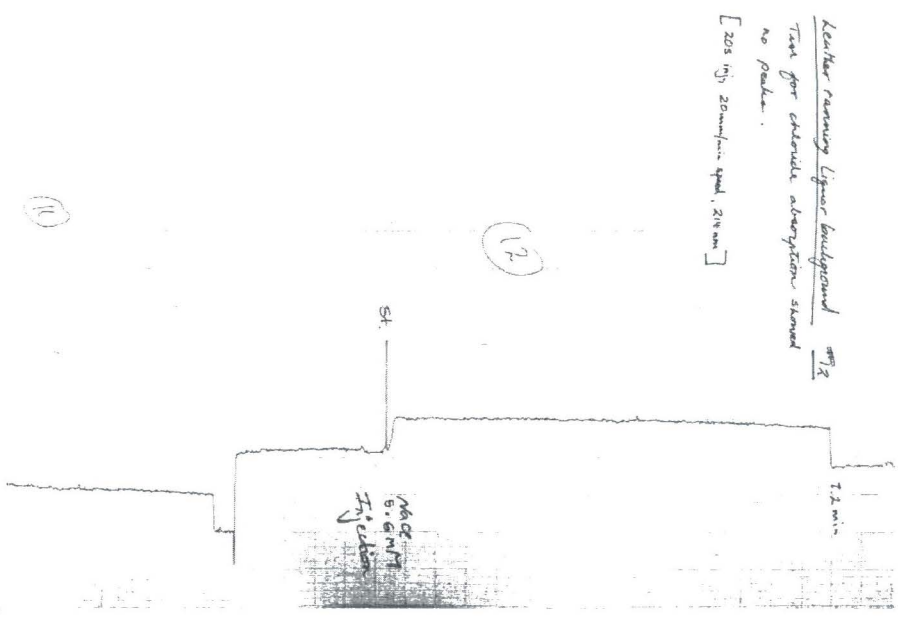

#111 chromate spike in uncomplexed undiluted sample no SPE

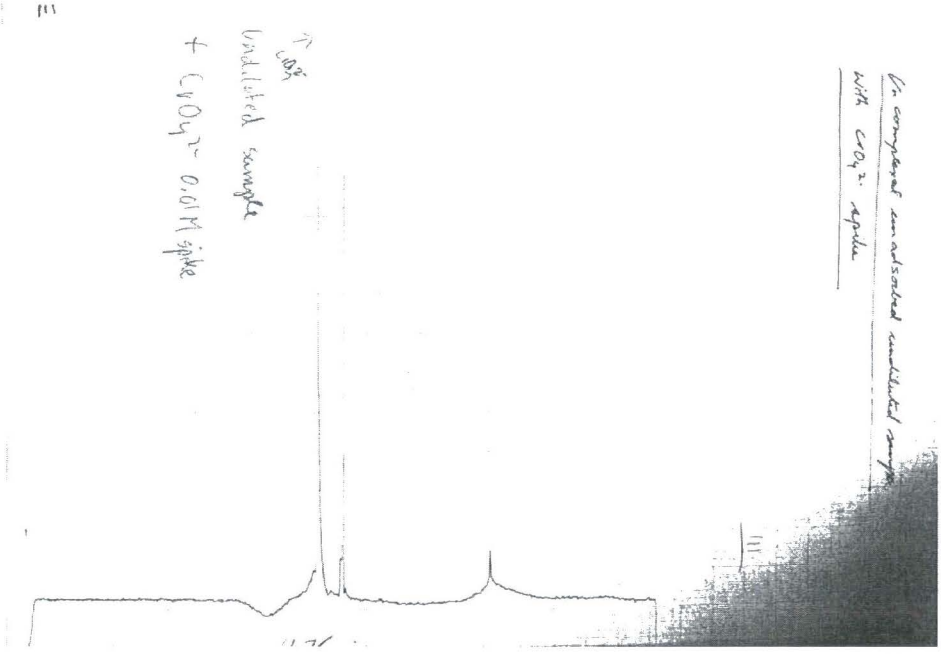

References

[1] R.A. Anderson, *Sci. Tot. Environ.,* 86 (1989) 75.

[2] W. Mertz, E.E. Roginski, F.J. Feldman, D.E. Thurman, *J. Nutr.,* 99 (1969) 363.

[3] C.S. Gad, *Sci. Tot. Environ.,* 86 (1989) 149.

[4] A.G. Levis, V. Bianchi, *Biological and Environmental Aspects of Chromium,* Elsevier, Amsterdam (1982).

[5] S. Vernitt, S.S. Levy, *Nature (London),* 250 (1974) 493.

[6] B. Gylseth, N. Gundersen, S. Langard, *Scan. J. Work Environ. Health,* 3 (1977) 28.

[7] R. Stern, *Biological and Environmental Aspects of Chromium,* Elsevier, Amsterdam, (1982).

[8] J.S. McHargue, *Amer. J. Physiol.*, 72 (1925) 583.

[9] J.S. McHargue, *Amer. J. Physiol.*, 77 (1926) 245.

[10] A.B. Beck, *Austral. J. Agr. Res.*, 12 (1961) 743.

[11] G.E. Cartwright, in *Symposium in Copper Metabolism*, (eds W.D. McElroy and B. Glass) John Hopkins Press, Baltimore (1950).

[12] E. Berman, *Toxic Metals and their Analysis*, Heydon & Son, Philadelphia (1980).

[13] E.L. Rickes, N.G. Brink, F.R. Koniusky, T.R. Wood and K. Folkers, *Science*, 108 (1948) 134.

[14] E.L. Smith, *Nature*, London, 162 (1948) 144.

[15] M. Barborik, J. Dusik, *Brit. Heart J.*, 34 (1972) 113.

[16] H.J.M. Bowen, *Trace Elements in Biochemistry*, Academic Press, NY (1966).

[17] E.J. Underwood, *Trace Elements in Human and Animal Nutrition*, Academic Press, NY (1977).

[18] F.W. Sunderman, Jr., M.J. Decsy, M.D. McNeeley, *Ann. N.Y. Acad. Sci.,* 199 (1972) 300.

[19] W. Kaim, B. Schwederski, *Bioinorganic Chemistry: Inorganic Elements in the Chemistry of Life. An Introduction and Guide,* John Wiley and Sons, Chichester, (1994).

[20] R.W. Hay, *Bioinorganic Chemistry*, Ellis Horwood, Chichester, (1984).

[21] M.C. Kimber, I.B. Mahadevan, S.F. Lincoln, A.D. Ward, E.R.T. Tiekink, *J. Org. Chem.,* 65 (2000) 8204.

[22] C.J. Fahrni, K.D. Simon, D.A. Suhy, M.S. Nasir, R.Dwivedi, T.V. O'Halloran, *J. Inorg. Biochem.,* 74 (1999) 125.

[23] G.K. Walkup, S. C. Burdette, S. J. Lippard, R. Y. Tsien, *J. Am. Chem. Soc.,* 122 (2000) 5644.

[24] E. Kessler, *Handbook on the Toxicology of Metals,* 2ed., Elsevier, New York (1986).

[25] J.H. Kennedy, *Am. J. Med. Sci.*, 251 (1966) 37.

[26] G.S. Nixon, H.D. Livingston, H. Smith, *Caries Res.,* 1 (1967) 327.

[27] Bureau of Mines, *Mineral Commodity Summaries*, U.S. Government Printing Office, Washington D.C. (1979).

[28] G. Schmidt, *Nucl. Sci. Abstr.*, 23, No. 37914 (1969) 3867.

[29] A. Wyttenbach, S. Bajo, A. Haekkinen, *Beitr. Tabakforsch.,* 8 (1976) 247.

[30] P.J. Sullivan, F.J. Agardy, J.J.J. Clark, *The Environmental Science of Drinking Water,* Elsevier, New York (2005).

[31] K.Z. Brainina, N.A. Malakhova, N.Y. Stojko, *Fres. J. Anal. Chem.* 368 (2000) 307.

[32] U.S. Environmental Protection Agency & U.S. Geological Survey; Water Resources Division, *National Environmental Methods Index*, http://www.nemi.gov

[33] K.H. Coale, K.W. Bruland, *Limnol. Oceanogr.*, 33 (1988) 1084.

[34] J.R. Donat, C.M.G. Van den Berg, *Mar. Chem.,* 38 (1992) 69.

[35] T.F. Rozan, M.E. Lassman, D.P. Ridge, G.W. Luther, *Nature*, 406 (2000) 879.

[36] J. Nuester, C.M.G. van den Berg, *Anal. Chem.* 77 (2005) 11.

[37] M.J. Ellwood, C.M.G. van den Berg, *Mar. Chem.*, 75 (2001) 33.

[38] M. Gledhill, C.M.G. van den Berg, *Mar. Chem.*, 47 (1994) 41.

[39] W. Sunda, *J. Mar. Res.*, 34 (1976) 511.

[40] W.G. Sunda, *Limnol. Oceanogr.*, 23 (1978) 870.

[41] G.E. Bately, S.C. Apte, J.L. Stauber, *Aust. J. Chem.,* 57 (2004) 903.

[42] C.M.G. Van den Berg, *Mar. Chem.*, 15 (1984) 1.

[43] J.W. Moffett, R.G. Zika, *Environ. Sci. Technol.,*, 21 (1984b) 804.

[44] J.W. Moffett, R.G. Zika, *Mar. Chem.* 21 (1987a) 301.

[45] Y.K. Chau, R. Gachter, K.L.S. Chan, *J. Fish. Res. Board Can.,* 31 (1974) 1515.

[46] H.P. van Leeuwen, R. Town, J. Buffle, R.M.J. Cleven, W. Davison, J. Puy, W.H. van Riemsdijk, L. Sigg, *Env. Sci. Technol.*, 39 (2005) 8545.

[47] H.P. van Leeuwen, *Dynamic aspects of in situ speciation processes and techniques.* J. Buffle, G. Horvai, Eds; vol. 6, IUPAC Series on Analytical and Physical Chemistry of Environmental Systems; Buffle, J., van Leeuwen, H. P., Series Eds.; Wiley: Chichester, 2000; pp 253-277.

[48] S. Jansen, R. Blust, H.P. van Leeuwen, *Environ. Sci. Technol.*, 36 (2002) 2164.

[49] R.J.M. Hudson, F.M.M. Morel, *Limnol. Oceanogr.*, 35 (1990) 1002.

[50] W. Davison, H. Zhang, *Nature,* 367 (1994) 545.

[51] N. Parthasarathy, J. Buffle, *Anal. Chim. Acta*, 284 (1994) 649.

[52] E. Bakker, *Anal. Chem.*, 76 (2004) 3285.

[53] J. Wang, *Trends Anal. Chem.*, 21 (4) (2002) 226.

[54] J. Wang, *Acc. Chem. Res.*, 35 (2002) 811.

[55] D.P. Mellor and L.E. Maley, *Nature*, 159 (1947) 370; 161 (1948) 436

[56] M. Calvin and N.C. Melchior, *J.Am. Chem. Soc.*, 70 (1948) 3270

[57] H. Irving and R.J.P. Williams, *Nature*, 162 (1948) 746

[58] D. Shriver, P. Atkins, *Inorganic Chemistry, 2ed*, Oxford University Press, NY (2000).

[59] A. Congreve (2004) *Responsive Lanthanide Complexes for Metal Ion Sensing,* Doctoral Thesis, Department of Chemistry, University of Durham.

[60] D. Parker, J.A.G.Williams (2003) *Metal Ions in Biological Systems, Volume 40, The Lanthanides and*

their Interactions, Eds. A. Sigel, H. Sigel, Marcel Dekker Inc., New York, Basel.

[61] J.R. Lakowicz, (1999) *Principles of Fluorescence Spectroscopy*, 2nd Edition, Kluwer Academic/

Plenum Publishers, New York.

[62] T. Koike, T. Watanabe, S. Aoki, E. Kimura, M. Shiro, *J. Am. Chem. Soc., 118* (1996) 12696.

[63] T. Koike, E. Kimura, I. Nakamura, Y. Hashimoto, M. Shiro, *J. Am. Chem. Soc.*,114 (1992) 7338.

[64] T. Koike, T. Abe, M. Takahashi, K. Ohtani, E. Kimura, M. Shiro, *J. Chem. Soc., Dalton Trans.*, (2002) 1764.

[65] S. Aoki, H. Kawatani, T. Goto, E. Kimura, M. Shiro, *J. Am. Chem. Soc.,123* (2001) 1123.

[66] Akkaya, E. U., Huston, M. E. Czarnik, A. W. *J. Am. Chem. Soc.,* 112 (1990) 3590.

[67] Huston, M. E., Engleman, C. Czarnik, A. W. *J. Am. Chem. Soc.,* 112 (1990) 7054.

[68] Czarnik, A.W. *Acc. Chem. Res.,* 27 (1994) 302.

[69] S. Aoki, S. Kaido, H. Fujioka, E. Kimura, *Inorg. Chem.*, 42 (2003) 1023.

[70] Koike, T.; Watanabe, T.; Aoki, S.; Kimura, E.; Shiro, M. *J. Am. Chem. Soc.*, 118 (1996) 12696.

[71] T. Hirano, K. Kikuchi, Y. Urano, T. Higuchi, T. Nagano, *Angew. Chem. Int. Ed.,* 39 (2000) 1052.

[72] C. Sauden, V. Balzeni, M. Gorka, S. Lee, M. Maetri, V. Vicinelli, F. Vögtle, *J. Am. Chem. Soc.,125* (2003) 4414.

[73] S.C. Burdette, S.J. Lippard, *Coordination Chemistry Reviews, 216-217* (2001) 333.

[74] S.C. Burdette, S.J. Lippard, *PNAS,100, 7* (2003) 3605.

[75] S. C. Burdette, C.J. Frederickson, W. Bu, S. J. Lippard, *J. Am. Chem. Soc., 125* (2003) 1778.

[76] C.J. Chang, E.M. Nolan, J. Jaworski, K.I. Okamoto, Y. Hayashi, M. Sheng, S.J. Lippard, *Inorg. Chem.*, 43 (2004) 6774.

[77] E.M. Nolan, S.J. Lippard, *Inorg. Chem.*, 43 (2004) 8310.

[78] C. J. Fahrni, T. V. O'Halloran, *J. Am. Chem. Soc., 121 (*1999)11448.

[79] M.C. Kimber, I.B. Mahadevan, S.F. Lincoln, A.D. Ward, E.R.T. Tiekink, *J. Org. Chem., 65 (*2000) 8204.

[80] C. J. Fahrni, K. D. Simon, D. A. Suhy, M. S. Nasir, R. Dwivedi, T. V. O'Halloran, *J. Inorg.*

Biochem.,74 (1999) 125.

[81] C.J.Frederickson, E.J. Kasarkis, D. Ringo, R.E. Frederickson, *J. Neurosci. Methods,* 20 (1987) 91.

[82] D.A. Pierce, N. Jotterand, I.S. Carrico, B. Imperiali, *J. Am. Chem. Soc., 123 (*2001) 5160.

[83] M.C. Kimber, I.B. Mahadevan, S.F. Lincoln, A.D. Ward, W.H. Betts, *Aust. J. Chem.*, 54 (2001) 43.

[84] S.P. Creaser, S.M. Pyke, S.F. Lincoln, *Aus. J. Chem., 56 (*2003) 61.

[85] M. Ghedini, M. La Deda, I. Aiello, A. Grisolia, *J. Chem. Soc., Dalton Trans.,* (2002), 3406.

[86] L.S. Sapochak, F.E. Benincasa, R.S. Schofield, J.L. Baker, K.K.C. Ricco, D. Fogarty, H. Kohlmann, K.F. Ferris, P.E. Burrows, *J. Am. Chem. Soc.,124 (* 2002) 6119.

[87] H. Haase, D. Beyersmann, *Biometals, (*1999) 247 – 254.

[88] T. Budde, A. Minta, J. A. White, A. R. Kay, *Neuroscience, 79, 2 (*1997) 347

[89] M. S. Nasir, C. J. Fahrni, D. A. Suhy, K. J. Kolodsick, C. P. Singer, T. V. O'Halloran, *JBIC,* 4 (1999) 775

[90] H. Nakamura, T. Yoshida, M. Todoka, *Bull. Chem. Soc. Jpn.,* 57 (1984) 2839

[91] Pengju Jiang, Zijian Guo, *Coord. Chem. Rev.,* 248 (2004) 205.

[92] R.P. Haugland, Handbook of Fluorescent Probes and Research Products, ninth ed., Molecular Probes Inc., (2002).

[93] F. Basolo, R.G. Pearson (1967*) Mechanisms of Inorganic Reactions*, 2ed, John Wiley & Sons, London.

[94] G. Milazzo, S. Caroli and V.K. Sharma, *Tables of Standard Electrode Potentials*, Wiley, London (1978).

[95] K.Z.Brainina, N.A. Malakhova, N.Y.Stojko, *Fres. J. Anal. Chem.,* 368 (2000) 307.

[96] C. M. Brett, *Pure Appl. Chem.,* 73 (2001) 1969.

[97] E. Pobozy, M. Knell, K. Killan, R. Kataky, M. Trojanowicz, *Electrophoresis*, 24 (d2003) 2259.

[98] R.D. Johnson, K.G. Bachas, *Anal. Bioanal. Chem.*, 376 (2003) 328.

[99] G. Hanrahan, D.G. Patil, J. Wang, *J. Environ. Monit.*, 6 (2004) 657.

[100] S. Mathison, E. Bakker, *Anal. Chem.*, 70 (1998) 303.

[101] E. Bakker, E. Pretsch, *Anal. Chem.*, 74 (2002) 420A.

[102] A. Sanchez, R.H. deRossi, *J. Org. Chem.,* 58 (1993) 2094.

[103] A. Odani, H. Masuda, K. Inukai, O. Yamauchi, *J. Am. Chem. Soc.*, 114 (1992) 6294.

[104] A. Kawase, H. Freiser, *Anal. Chem.*, 38 (1966) 1577.

[105] A. Bevilacqua, R.I. Gelb, W.B. Hebard, L.J. Zompa, *Inorg. Chem.*, 26 (1987) 2699.

[106] R. Delgado, S. Quintino, M. Teixeira, A. Zhang, *J. Chem. Soc., Dalton Trans.*, (1996) 55.

[107] F. Marisicano, C. Monberg, B.S. Martincigh, K. Murray, P.M. May, D.R. Williams, *J. Coord. Chem.*, 16 (1998) 321.

[108] P.M. May, K. Murray, D.R. Williams, *Talanta,* 35 (1998) 23.

[109] J. Wang, *Analytical Electrochemistry*, 2ed., Wiley-VCH, New York (2000).

[110] J. Lingane, *Chem. Rev.*, 29 (1941) 1.

[111] G. Hanrahan, D.G. Patil, J. Wang, *J. Environ. Monit.*, 6 (2004) 657.

[112] C. Belmont-Hebert, M.-L. Tercier, J. Buffle, G.C. Fiaccabrino, N.F. de Rooij, M. Koudelka-Hep, *Anal. Chem.*, 70 (1998) 2949.

[113] K.A. Howell, E.P. Achterberg, C.B. Braungardt, A.D. Tappin, P.J. Worsfold, D.R. Turner, *Tr. A. C.*, 22, 11 (2003) 828.

[114] O.M. Lage, *Euro. J. Phycol.*, 31 (1996) 341.

[115] D.M.J. Tubbing, *Wat. Res.*, 28 (1994) 37.

[116] L. Jin, *Anal. Chim. Acta.*, 412 (2000) 77.

[117] H.B. Xue, *Limnol. Oceanogr.*, 38 (1993) 1200.

[118] F.L.L. Muller, S.B. Gulin, A. Kalvoy, *Mar. Chem.*, 76 (2001) 233.

[119] M.J. Ellwood, C.M.G. Van den Berg, *Mar. Chem.*, 68 (2000) 295.

[120] S. Meylan, N. Odzak, R. Behra, L. Sigg, *Anal. Chim. Acta,* 510 (2004) 91.

[121] E. Fischer, *Anal. Chim. Acta,* 432 (2001) 11.

[122] C.M.G. Van den Berg, Z.Q. Huang, *J. Electroanal. Chem.*, 177 (1984) 269.

[123] W.W. Bedsworth, D.L. Sedlak, *Environ. Sci. Technol.*, 33 (1999) 926.

[124] C.M.G. Van den Berg, *Anal. Chim. Acta,* 250 (1991) 265.

[125] J. Buffle, M.-L. Tercier-Waeber, *Tr. A. C.*, 24, 3 (2005) 172.

[126] Town RM, van Leeuwen HP, *J. Electroanal. Chem.*, 535 (2002) 11.

[127] Daniele S, Bragato C, Baldo MA, Wang J, *Analyst*, 125 (2000) 731.

[128] I. Palchetti, A. Cagnini, M. Mascini, A.P.F. Turner, *Mikrochim. Acta*, 131 (1999) 65.

[129] W. Martinotti, *Anal. Chim. Acta, 305 (1995) 183.*

[130] I. Pizeta, *Anal. Chim. Acta,* 351 (1997) 73.

[131] C.M.G. van den Berg, *Mar. Chem.*, 15 (1984) 1.

[132] S.C. Apte, M.J. Gardner, J.E. Ravenscroft, J.A. Turrell, *Anal. Chem. Acta*, 235 (1990) 287.

[133] S.C. Apte, M.J. Gardner, J.E. Ravenscroft, *Mar. Chem.*, 29 (1990) 63.

[134] K.H. Coale, K.W. Bruland, *Limnol. Oceanogr.*, 33 (1988) 1084.

[135] G. Schwarzenbach, R. Gut, G. Anderegg, *Helv. Chim. Acta,* 37 (1954) 937.

[136] G. Schwarzenbach, H. Ackermann, *Helv. Chem. Soc.,* 35 (1952) 486.

[137] J. Buffle, J. Electroanal. Chem., 125 (1981) 273.

[138] J. Buffle, A. M. Mota, M. L. GonÁalves, *Port. Electrochim. Acta*, 3 (1985) 293.

[139] D. S. Jain, O. Prakash, S. K. Bhasin, *J. Electrochem. Soc. India*, 25 (1976) 139.

[140] A. M. Bond, J. Electroanal. Chem., 20 (1969) 223.

[141] A. M. Bond, J. Electroanal. Chem., 23 (1969) 227.

[142] G. A. Heath, G. Hefter, J. Electroanal. Chem., 84 (1977) 295.

[143] M. Ferna¬ndez, C. Arinfo, J. M. DÌaz-Cruz, R. Tauler, M. Esteban, *J. Electroanal. Chem.*, 505 (2001) 44.

[144] M. Ferna¬ndez, C. Arinfo, J. M. DÌaz-Cruz, R. Tauler, M. Esteban, *Electroanalysis*, 13 (2001) 1405.

[145] R. M. Town, H. P. van Leeuwen, *J. Electroanal. Chem.*, 535 (2002) 11.

[146] J.J. Lingane, *Chem. Rev.*, 29 (1941) 1.

[147] D.D. DeFord, D.N. Hume, *J. Am. Chem. Soc.,* 73 (1951) 5321.

[148] D.N. Hume, D.D. DeFord, G.C.B. Cave, *J. Am. Chem. Soc.,* 73 (1951) 5323.

[149] H.G. De Jong, H.P. van Leeuwen, K. Holub, *J. Electroanal. Chem.*, 234 (1987) 1.

[150] H.G. De Jong, H.P. van Leeuwen, *J. Electroanal. Chem.*, 234 (1987) 17.

[151] H.G. De Jong, H.P. van Leeuwen, J. Electroanal. Chem., 234 (1987) 1.

[152] J.M. DÌaz-Cruz, C. Arinfo, M. Esteban, E. Casassas, *Electroanalysis*, 3 (1991) 299.

[153] A.M. Nadal, C. Arinfo, M. Esteban, E. Casassas, *Electroanalysis*, 3 (1991) 309.

[154] J.M. DÌaz-Cruz, C. Arinfo, M. Esteban, E. Casassas, *J. Electroanal. Chem.*, 333 (1992) 33.

[155] R. Guidelli, D. Cozzi, *J. Phys. Chem.*, 71 (1967) 3020.

[156] R. Guidelli, D. Cozzi, *J. Phys. Chem.* 71 (1967) 3027.

[157] I. Cukrowski, J.M. Zhang, *Electroanalysis,* 16 (2004) 612.

[158] I. Cukrowski, M. Adsetts, *J. Electroanal. Chem.*, 429 (1997) 129.

[159] I. Cukrowski, *Electroanalysis*, 9 (1997) 1167.

[160] I. Cukrowski, S. A. Loader, *Electroanalysis*, 10 (1998) 877.

[161] I. Cukrowski, R. D. Hancock, R. C. Luckay, *Anal. Chim. Acta*, 319 (1996) 39.

[162] I. Cukrowski, *Electroanalysis*, 11 (1999) 606.

[163] I. Cukrowski, *J. Electroanal. Chem.* 460 (1999) 197.

[164] I. Cukrowski, J.M. Zhang, *Chem. Anal.*, 50 (2005) 3.

[165] I. Cukrowski, D.M. Mogano, J.R. Zeevaart, *J. Inorg. Biochem.,* 99 (2005) 2308.

[166] D.R. Crow, *Polarography of Metal Complexes*, Academic Press, London, 1969

[167] I. Cukrowski, J.M. Zhang, A. van Aswegen, *Helv. Chim. Acta,* 87 (2004) 2135.

[168] K. Ashley, *J. Haz. Mat.,* 102 (2003) 1.

[169] J.M. Zen, A.S. Kumar, D.M. Tsai, *Electroanalysis,* 15 (2003) 1073.

[170] A.J. Downard, *Electroanalysis*, 12, 14 (2000) 1085.

[171] B. Barbier, J. Pinson, G. Desarmot, M. Sanchez, *J. Electrochem. Soc.*, 137 (1990) 1757.

[172] J.M. Zen, A.S. Kumar, D.M. Tsai, *Electroanalysis*, 15, 3 (2003) 1073.

[173] C.P. Andrieux, F. Gonzalez, J.M. Saveant, *J. Am. Chem. Soc.*, 119 (1997) 4292.

[174] H. Maeda, T.X. Li, M. Hosoe, M. Itami, *Anal. Sci.*, 10 (1994) 963.

[175] H. Maeda, M. Itami, Y. Yamauchi, H. Ohmori, *Chem. Pharm. Bull.*, 44 (1996) 2294.

[176] M. Delamar, R. Hitmi, J. Pinson, J.M. Saveant, *J. Am. Chem. Soc.,* 114 (1992) 5883.

[177] C. Bourdillon, M. Delamar, C. Demaille, R. Hitmi, J. Moiroux, J.J. Pinson, *J. Electroanal. Chem.*, 336 (1992) 113.

[178] K. Morita, A. Yamaguchi, N. Teramae, *J. Electroanal. Chem.* 563 (2004) 249.

[179] M. Delamar, R. Hitmi, J. Pinson, J.M. Saveant, *J. Am. Chem. Soc.,* 114 (1992) 5883.

[180] I. Kosuke, *Electrochemistry in Nonaqueous Solutions*, Wiley-VCH, Weinheim (2002).

[181] G. Fonrodona, C. Rafols, E. Bosch, M. Roses, *Anal. Chim. Acta* 335 (1996) 291.

[182] S. Rondinini, P. Longhi, P.R. Mussini and T. Mussini, Pure Appl. Chem., 59 (1987) 1693.

[183] R.W. Ramette, *Chemical Equilibrium & Analysis*, Addison-Wesley, Don Mills, Ontario (1981).

[184] R. Kataky, *Ion-Selective Sensors applied to the Analysis of Blood Electrolytes,* Doctoral Thesis, University of Newastle-upon-Tyne, 1988.

[185] P. Gans, A. Sabbatini., A. Vacca., *Talanta*, 43 (1996) 1739.

[186] L. Alderighi, P. Gans, A. Ienco, D. Peters, A. Sabbatini, A. Vacca, *Coord. Chem. Rev.*, 184 (1999) 311.

[187] P. Gans, A. Sabbatini, A. Vacca, *J. Chem. Soc., Dalton Trans.*, (1985) 1195

[188] P. Gans, *Hyperquad2003*, Protonic Software (2003).

[189] A.E. Martell, R.J. Motekaitis (1992) *Determination and Use of Stability Constants*, VCH Publishers Inc., Cambridge.

[190] J. Burgess (1988) *Ions in Solution*, John Wiley & Sons, Rexdale, Ontario.

[191] Lindsay Molyneux, Molspin Equipment, Newcastle.

[192] P. Gans, *Molspin Titrator,* Protonic Software (2004).

[193] A. Congreve, R. Kataky, M. Knell, D. Parker, H. Puschmann, K. Senanayake, *New J. Chem.*, 27 (2003) 98

[194] A. Vesala, *J. Chem. Ed.*, 69 (7) (1992), 577.

[195] R.G. Bates, *Determination of pH: Theory and Practice, 2ed*, John Wiley & Sons, Toronto (1973).

[196] G. Gran, *Acta Chem. Scan.*, 4 (1950) 559.

[197] G. Gran, *Analyst,* 77 (1952) 661.

[198] D.A. Skoog, F.J. Holler, T.A. Nieman, *Principles of Instrumental Analysis, 5th ed.*,Harcourt Brace College, London (1998).

[199] M. Delamar, , *J. Am. Chem.Soc. 114* (1992) 5883.

[200] R. Hitmi, J. Pinson, J-M. Save´ant, Fr. Pat. 91011172.

[201] C. Bourdillon, C. Demaille, R. Hitmi, J. Moiroux, J. Pinson, *J. Electroanal. Chem. 336* (1992) 113.

[202] P. Allongue, M. Delamar, B. Desbat, O. Fagebaume, R. Hitmi, J. Pinson, J.M. Saveant, *J. Am. Chem. Soc.*,119 (1997) 201.

[203] S.B. Khoo, J. Zhu, *Anal. Chim. Acta.*, 373 (1998) 15

[204] ECLab software, Version 8.05, Biologic Science Instruments, Princeton Applied Research (2004).

[205] S. Pozidiakova, A. Padarauskas, *Analyst*, 123 (1998) 1497

[206] R. Bucci, *J.Coord.Chem.*, 24(1991) 169

[207] V. Solov'ev, *Stability Constant Database,* Version 5.3, Academic Software (2001).

[208] S. Rondinini, P.R. Mussini, T. Mussini, Pure Appl. Chem., 70, 7 (1998) 1419.

[209] Y. Marcus, T. Mussini, K. Izutsu, Pure Appl. Chem. 63, 11, (1991) 1647.

[210] E. Kilic, N. Aslan, *Microchim. Acta*, 151 (2005) 89.

[211] P. Gans, *Hyperquad Simulation and Speciation*, Protonic software (2000).

[212] B. Miller, *J. Electrochem. Soc.,* 117 (1969) 1675.

[213] S. Dong, Y. Xie, G. Cheng, *Electrochim. Acta,* 37 (1992) 17.

[214] I. Cukrowski, J.M. Zhang, A. van Aswegen, *Helvetica Chimica Acta,* 87 (2004) 2135.

[215] I. Cukrowski, J.M. Zhang, *Electroanalysis*, 16 (2004) 612.

[216] P. Gans, A. Sabatini, A. Vacca, *pHab* software, Ver. 3.0.24 (2003).

[217] E. Heideman, *Fundamentals of Leather Manufacturing*, Roetherdruck, Darmstadt (1993).

[218] A.R. Timerbaev, O.P. Semenova, W. Buchberger, G.K. Bonn, *Fresenius J. Anal. Chem.,* 354 (1996) 414.

[219] Z. Chen, R. Naidu, A. Subramanian, *J. Chromatogr. A,* 927 (2001) 219

[220] A.R. Timerbaev, *Talanta,* 52 (2000) 573.

[221] E. Dabek-Zlotorzynska, E. Lai, A.R. Timerbaev, *Anal. Chim. Acta,* 359 (1998) 1.

[222] R. Delgado, M. Figueira, S. Quintino, *Talanta,* 45 (1997) 451.

[223] S. Schaffer, P. Gareil, C. Dezael, D. Richard, *J. Chromatogr. A,* 707 (1996) 151.

[224] A.R. Timerbaev, O.P. Semenova, W. Bucherber, G.K. Bonn, *Analyst*, 354 (1996) 414.

[225] J. Gaur, G. Schmid, *J. Electroanal. Chem.*, 24 (1970) 279.

[226] R. Frankenthal, D. Thompson, *J. Electroanal. Soc.*, 123 (1976) 799.

[227] A. Bard, R. Parsons, J. Jordan, *Standard Potentials in Aqueous Solution*, Marcel Dekker, NY (1985).

[228] I. Stewart, J. Olesik, *J. Chrom. A,* 872 (2000) 227.

[229] H. Stunzi, *J. Inorg. Chem.*, 28 (1989) 66.

[230] J-M. Save´ant, *Adv. Phys. Org. Chem. 26* (1990) 1.

[231] P. Allongue, M. Delamar, B. Desbat, O. Faugebaume, R. Hitmi, J. Pinson, J-M. Save´ant, *J. Am. Chem. Soc.,* 119 (1997)

[232] Y. Ohnuki, H. Matsuda, *J. Electroanal. Chem.* 158 (1983) 55.

[233] T. Ohsaka, T. Hirokawa, H. Miyamoto, M. Oyama, *Anal. Chem.*, 59 (1987) 1758.

[234] M. Sawhney, D. Joshi, *Indian J. Chem.*, 19A (1980) 85.

[235] M. Khalil, A. Attia, *J. Chem. Eng. Data*, 45 (2000) 1108.

[236] L. Petitt, J. Swash, *J. Chem. Soc., Dalton Trans.*, 286 (1978).

[237] G. Venkatnarayana, S. Swamy, *Indian J. Chem.*, 23A (1984) 501.

[238] E. Chiacchierini, G. D'Ascenzo, *Ann. Chim. (Rome)*, 67 (1977) 195.

[239] J. Wang, J. Lu, B. Tian, D. MacDonald, K. Olsen, *Analyst,* 124 (1999) 349.